NASA

DIAGNOSTIC MEASUREMENTS IN ALPHA (ALKALI PLASMA HALL ACCELERATOR)

by

P. F. Jacobs, G. L. Cann, and R. L. Harder

prepared for

NATIONAL AERONAUTICS AND SPACE ADMINISTRATION

CONTRACT NAS3-8902

ELECTRO - OPTICAL SYSTEMS, INC.

A XEROX COMPANY

300 N. Halstead St., Pasadena, California, 91107 · (213) 449-1230

Requests for copies of this report should be referred to

National Aeronautics and Space Administration
Scientific and Technical Information Facility
P. O. Box 33
College Park, Maryland   20740

NASA-CR-72233
EOS ~~~~~~~-7053-Final

FINAL REPORT

DIAGNOSTIC MEASUREMENTS IN ALPHA (ALKALI PLASMA HALL ACCELERATOR)

by

P. F. Jacobs, G. L. Cann, and R. L. Harder

prepared by

NATIONAL AERONAUTICS AND SPACE ADMINISTRATION

May 31, 1967

CONTRACT NAS3-8902

Technical Management
NASA Lewis Research Center
Cleveland, Ohio
Spacecraft Technology Division
Stanley Domitz

ELECTRO-OPTICAL SYSTEMS, INC.
A XEROX COMPANY

FOREWORD

The work described in this final report was carried out for the Lewis Research Center of the National Aeronautics and Space Administration. The program was directed by Mr. Stanley Domitz, the contract technical monitor.

The work was performed at Electro-Optical Systems, Inc., in the Plasma Physics Department under the direction of Dr. G. L. Cann. Dr. P. F. Jacobs and Dr. Cann were coprincipal investigators.

The report was prepared by Drs. Jacobs and Cann and Mr. R. L. Harder. The authors gratefully acknowledge the contributions of Messrs. L. R. Gallagher (spectroscopy), K. Edwards (experimental diagnostics), R. W. Prichard and C. H. Giltner (design), T. Jacobson (electronics), C. B. Shepard (project engineer), and C. Hains (data analysis).

The authors wish to acknowledge the participation of the U.S. Air Force Aero Propulsion Laboratory in this program through Contract AF33(615)-1579. This contract contributed to the fabrication and testing of the ALPHA thrustor.

The secondary report number assigned by Electro-Optical Systems, Inc. is 7053-Final. This report covers the period 22 February through 17 May 1967.

DIAGNOSTIC MEASUREMENTS IN ALPHA
(Alkali Plasma Hall Accelerator)
By
P. F. Jacobs, G. L. Cann and R. L. Harder

ABSTRACT

This report presents the results of a one-year study of the Alkali Plasma Hall Accelerator (ALPHA). The program may be essentially divided into three areas of effort. The first entailed the design, fabrication, checkout and parametric performance testing of the ALPHA engine. Extensive measurements of electrical power input, thrust, propellant mass flow, thermal efficiency, thrust efficiency, specific impulse, magnet power, power losses to the cathode, buffer, anode and magnet housings, overall efficiency, and the background tank pressure are presented.

The second and major area of study was a detailed series of diagnostic experiments aimed at improving the confidence of the performance results referred to above, and also at furthering knowledge of the basic physics involved in the ALPHA device. The diagnostic experiments include measurements of the plasma axial velocity using Doppler-effect spectroscopy and a phototracer technique based upon optical time-of-flight determinations. These experimental results are compared directly with the specific impulse determined from the thrust and mass-flow-rate measurements. Strong evidence is presented for the existence of significant plasma acceleration in the region downstream of the anode and magnet coil. Measurements of the total beam power and the local energy flux distributions were performed using a large segmented total beam calorimeter and a small local energy flux probe. The self-consistency of the results for the total power in the plasma exhaust were excellent. These were determined by three independent techniques:

a. Input power minus component power losses, measured by coolant water calorimetry.

b. Beam power measured _in situ_ with the segmented total beam calorimeter, and

c. Numerical integration of the local energy flux probe measurements.

These results are especially significant with respect to the validity of the thermal efficiency measurements. Other diagnostic measurements which are presented include the distribution of the axial, radial, and azimuthal components of the magnetic field both with and without the plasma present, estimates of the current distribution and diamagnetic effect within the plasma, spectroscopic evidence of the existence of plasma rotation, mass flux distributions, and the magnitude and characteristic frequencies of the emf induced by a magnetic loop probe.

The final area of study involved a modest analytical study involving the concept of an "effective mass flow rate" and arriving at a set of relations for the discharge voltage in the regimes of mass flow rate which are higher or lower than the effective mass flow rate.

CONTENTS

CONTENTS (contd)

LIST OF ILLUSTRATIONS

DIAGNOSTIC MEASUREMENTS IN ALPHA
(Alkali Plasma Hall Accelerator)
By
P. F. Jacobs, G. L. Cann and R. L. Harder

Electro-Optical Systems, Inc.

SECTION 1

SUMMARY

Analytical and experimental research aimed at detailed diagnostic measurements of an Alkali Plasma Hall Current Accelerator were performed during this program. The research was concentrated on:

a. Design and fabrication of a Lithium Hall Current Accelerator. This included the electrodes, insulators and buffer components, the lithium feed system, the thrust balance and the attendant instrumentation.

b. Determination of the azimuthal velocity by means of Doppler rotation spectroscopy of lithium, hydrogen, and impurity ion lines.

c. Determination of the axial velocity of the beam by means of Doppler shifts of the spectral lines resulting from transitions among the excited states of singly ionized lithium (Li II).

d. Determination of axial velocity and axial velocity distributions of the various components (i.e., lithium atoms and ions, hydrogen atoms and ions, and impurities) of the plasma at a number of different positions using the phototracer technique.

e. Analytic investigations of expressions for the arc potential and engine efficiency based upon the principle of effective mass flow.

f. Measurement of total beam power and energy flux distribution using the segmented, water-cooled total beam calorimeter.

g. Measurement of local energy flux distribution and calculation of integrated total beam power from the data obtained using the double-jacketed energy flux probe immersed in the plasma.

h. Measurements of the distribution of the axial, radial, and azimuthal components of the magnetic field, both with and without the plasma present, using a three-dimensional Hall-effect magnetic probe.

i. Determination of the existence of current paths significantly downstream of the anode, through calculations based on the magnetic field data.

j. Measurement of the time variation of the radial component of the magnetic field using a magnetic-loop probe. Detection of certain characteristic output frequencies and their dependence upon magnetic field strength.

k. Determination of relative mass flux rates at various positions surrounding the plasma obtained from relative rates of alkali metal deposition.

l. Development of a spectral calibration source, consisting of a water-cooled discharge tube capable of generating quiescent spectra of Li I and Li II for use in improving the accuracy of the spectroscopic Doppler velocity measurements.

During the reporting period a number of tests were conducted using the lithium thrustor developed on Air Force Contract AF33(615)-1579. This thrustor is virtually identical to the one which was fabricated for this program. The tests were conducted at pressures between 10^{-4} and 2×10^{-6} torr with lithium as the primary propellant (5 to 10 milligrams per second) and hydrogen (0.5 to 1.0 milligram per second) as a secondary propellant.

The input power was typically 10 to 20 kilowatts, the thrust level 25 to 45 grams, the specific impulse 2000 to 6000 seconds, the thermal efficiency 50 to 80 percent, the thrust efficiency 30 to 55 percent, the arc current 300 to 400 amperes, and the magnetic field at the cathode tip 1000 to 3000 gauss.

Due to the large number of experiments which were conducted, and the varying degree to which each technique reached, exceeded, or fell short of the original goals intended for that specific diagnostic measurement, it is believed to be appropriate to summarize not only the important results, but the degree of confidence or utility which was actually realized during this program. The opinions are certainly somewhat subjective. However they do reflect the essential feelings

of those who actually performed the experiments and are perhaps on the closest terms with the various pitfalls. For this reason, and also to aid those who might be interested in repeating any or all of these measurements, certain comments as to the confidence, accuracy, ease of use, and sources of error characteristic of these techniques will also be included. These comments are also contained in considerably greater detail within the main body of the report.

Probably the most repeatable, accurate and confident results were those of the total beam calorimeter and the local energy flux probes. In both cases the energy flux distributions were remarkably similar in any given run. The local energy flux probe was carefully calibrated, and gives this distribution directly. The total beam calorimeter was segmented so that separate contributions to various annular segments could be obtained. This device thereby provides not only the total beam power but its radial distribution as well. Furthermore, the agreement between the net beam power (i.e., input electrical power minus arc jet component losses) and the total beam calorimeter results, as well as the integrated value of the local energy flux probe measurements, taken across a diameter of the plasma exhaust, were always in good agreement. Finally, this agreement persisted over a range of electrical input power from 11 to 18 kilowatts. These results appear to indicate a high level of confidence in these techniques and, correspondingly, a new level of confidence in the determinations of the thermal efficiency of ALPHA.

The axial velocity measurement by Doppler spectroscopy is an excellent example of an experimental technique which, initially subject to very serious errors stemming from the requirement of measuring rather small spectral shifts (viz., of the order of 0.5 Å),with instrument errors of comparable magnitude, was refined to the point where relatively good (± 20 percent) velocity measurements were possible. This great improvement in precision was the result of _in situ_ comparison with the

unshifted spectra of Li II from a laboratory "calibration" source. Instrument errors are effectively "cancelled out" by direct comparison of the calibration source spectra and that from ALPHA. The major limitation of the spectroscopic Doppler axial velocity technique was the requirement of performing velocity measurements near the exit plane due to the very rapid decay of the Li II spectra at downstream positions of the order of 1 meter. For this reason it was not possible to detect the presence (or absence) of plasma acceleration with this technique. It is believed that this technique, when applied in conjunction with a quiescent discharge source, can yield valuable velocity data.

Perhaps the most surprising results were those obtained with the photo-tracer system. This technique[*],[**] is based upon the time-of-flight of natural light intensity fluctuations. Criticized on a number of grounds (i.e., effects of acoustic waves, uncertainties in signature identification, line-of-sight and spatial resolution problems, etc.), it is nonetheless interesting that this simple and relatively straightforward technique has been reported as accurate within about 20 percent. This is substantially in agreement with our results. Furthermore, the photo-tracer velocity results: (a) are well within 20 percent of the results of the axial velocity measurements by Doppler spectroscopy . . . at or near the exit plane; (b) indicate definite acceleration of the plasma just downstream of the exit plane; (c) give velocity results, at about 1 meter downstream which are in good agreement with thrust and mass flow measurements in lithium, sodium and hydrogen plasmas; (d) show the existence of velocity distribution functions, and, in the case of lithium the existence of what appears to be two (or more) "groups" of different velocities; (e) give evidence of radial distributions in velocity; and (f) continue to show good agreement with effective exhaust velocities when the specific impulse of ALPHA was varied from about 2000 to 7000 seconds.

---

[*] D. W. Esker, "Comparison of Exhaust Velocity with the Propagation Velocity of Random Light Fluctuations", J. Spacecraft and Rockets, Vol. 4, No. 5, May 1967

[**] W. M. Van Camp, D. W. Esker, R. J. Checkley, W. G. Duke, et al., "Study of Arc Jet Propulsion Devices", NASA Report CR-54691, March 1966

The measurements of the distributions of the axial, radial and azimuthal components of the magnetic field, as measured with the three dimensional Hall-effect magnetic probe are of reasonably good quality, but are subject to misalignment problems, hysteresis effects associated with problems in accurate positioning and the inherent problem of finding the small difference between two large numbers for the cases of magnetic field measurements with and without the plasma present. Nonetheless, this can be remedied, to some extent, if inconveniently, by turning the arc on and off rapidly with the probe at a fixed position. In all cases a small but distinct (typically 3-5 percent) diamagnetic effect was observed. After careful precautions it was also possible to make reasonably systematic measurements of B_θ. The determination of current density distributions was, of course, limited by the above problems. Nonetheless, definite evidence of significant current, as far as 0.3 meter from the exit plane, was observed. It is felt that improvements in positioning and/or sweeping the probe would enhance the accuracy of these measurements.

A loop magnetic probe was also employed to study the behavior of the time variations of the radial component of the magnetic field. This device is of simple construction and is relatively easily employed. The probe output was displayed on an oscilloscope and a number of characteristic frequencies were observed. These were 60, 120 and 360 Hz (most likely associated with power supply ripple) and a frequency in the 10^5 to 3×10^5 Hz range which was found to be directly proportional to the applied magnetic field strength. The amplitude of these signals did not vary significantly with the magnetic field strength but was found to be about 5-7 times greater when ALPHA was operated solely on hydrogen than in the usual hydrogen-lithium mode. While the phenomena is not definite, the dependencies upon magnetic field and ion mass suggest the possible effects of ion cyclotron motions.

One of the diagnostic techniques which did not produce results of great utility was the alkali metal mass deposition probe which was to be used for mass flux measurements. A major problem was the presence of strong electric fields in the plasma-produced voltage drops across the collecting elements which were often comparable to, or greater than the intended IR drop in the probe. Furthermore, the probe was overly sensitive to orientation (presumably with respect to the local electric field vector) and actually behaved more like an E field probe than a mass deposition probe. Another problem, which is really inherent to a deposition probe, was the fact that once the probe is coated with lithium at a given point, it must be removed from vacuum and cleaned before a new data point can be obtained. However, in spite of the problems with the actual mass flux probe itself, some relative measurements of the lithium mass flux at a number of positions around the tank wall were taken. These data were obtained by observing the rate of attenuation of light transmission, through various tank windows, as measured with photomultipliers and actual solar cell units. One result, which may be of considerable interest to a solar powered electric propulsion system, was the fact that the deposition rate **behind ALPHA was** about 4×10^{-6} of the deposition rate at the opposite (downstream) end of the tank. Since the deposition rate at the downstream end of the tank reaches a maximum value of about 10^{-6} g/cm^2-sec this implies a rate of roughly 4×10^{-12} gram/cm^2-sec behind the engine (but without a shadow shield). This corresponded to a measured solar cell degradation of 2 percent in a 110 hour ALPHA life test.

The only diagnostic technique which produced no data whatsoever was the torque target; intended to measure the angular momentum of the beam. This was not due to any failure of the device, but rather it resulted from the fact that the estimated torques were sufficiently small that the engine would have had to be remounted in a vertical mode and fired downward at the torque sensing balance. The conversion of all the

mounting brackets, electrical feedthroughs and support equipment would have entailed considerable shutdown time as well as expense. Therefore, these tests were not performed.

SECTION 2

INTRODUCTION

During the past few years a number of investigators (Refs. 1 through 13) have been concerned with improving the performance of specific versions of the general class of MPD arcs. At present most of the effort appears to be concentrated in research and development of either ammonia or alkali metal (most commonly lithium) systems. The ammonia system has the advantage of a simple, reliable feed system, and the disadvantage of inherently high frozen flow losses with correspondingly reduced overall efficiency. The lithium system (see Figs. 1 through 3) has almost inverse characteristics. That is, its primary disadvantage, at present, is the complexity of the feed system (see Figs. 4 and 5). Its major advantage lies in the relatively small frozen flow losses and the correspondingly high overall efficiency which may be achieved.

Recently there has been a trend toward cross-checking as much of the performance data as possible through independent plasma diagnostic measurements. This desire for independent verification of thrustor performance indices, such as thrust, specific impulse and thermal and overall efficiency, stems from the lack of uniform results obtained by the various investigators. Often these variances have their origins in different experimental conditions (i.e., testing chamber dimensions, chamber materials, and background pressure) while other differences involve variations in thrustor design (i.e., thrustor size, shape, and materials) or even the expedient, but inappropriate, tendency to check the performance of one propellant on a thrustor designed to operate on a different substance.
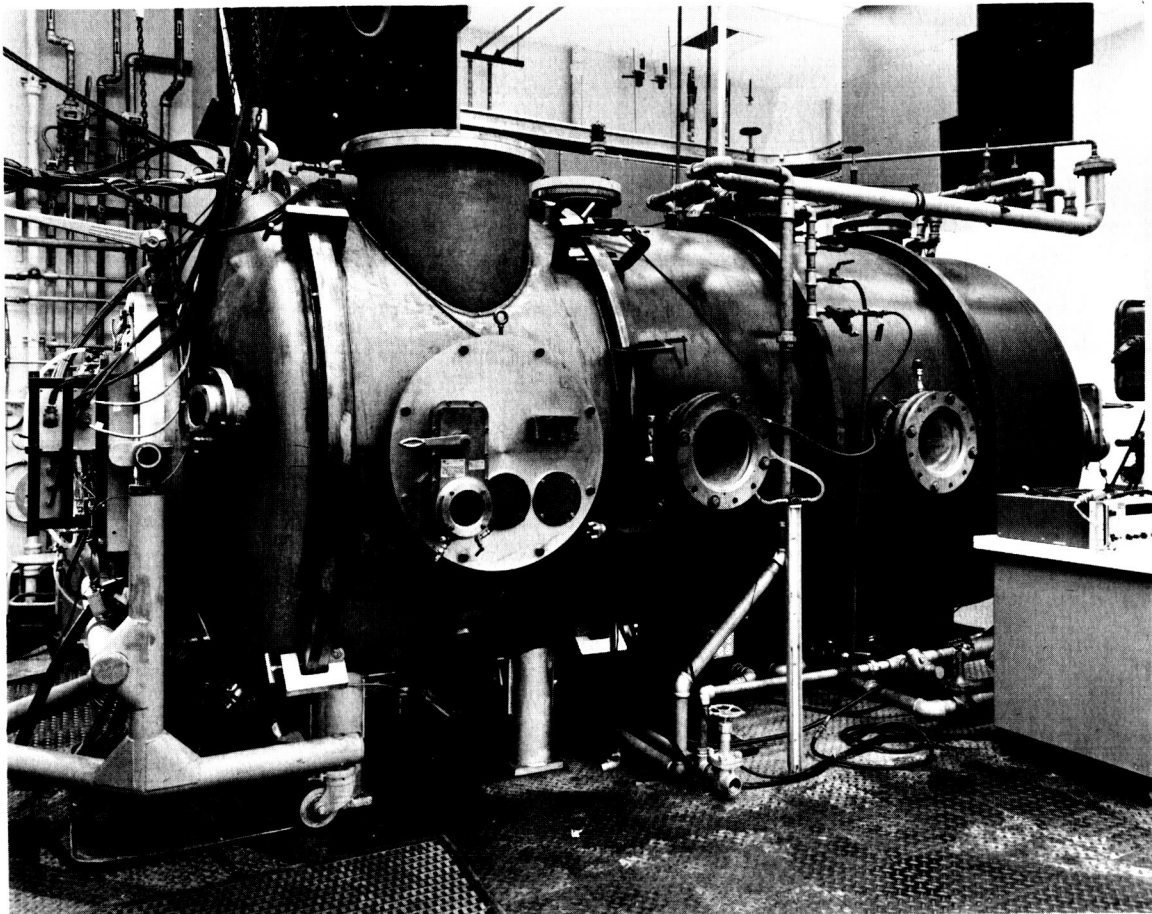
Figure 1. Photograph of 6 x 14 foot Propulsion Test Chamber

866107
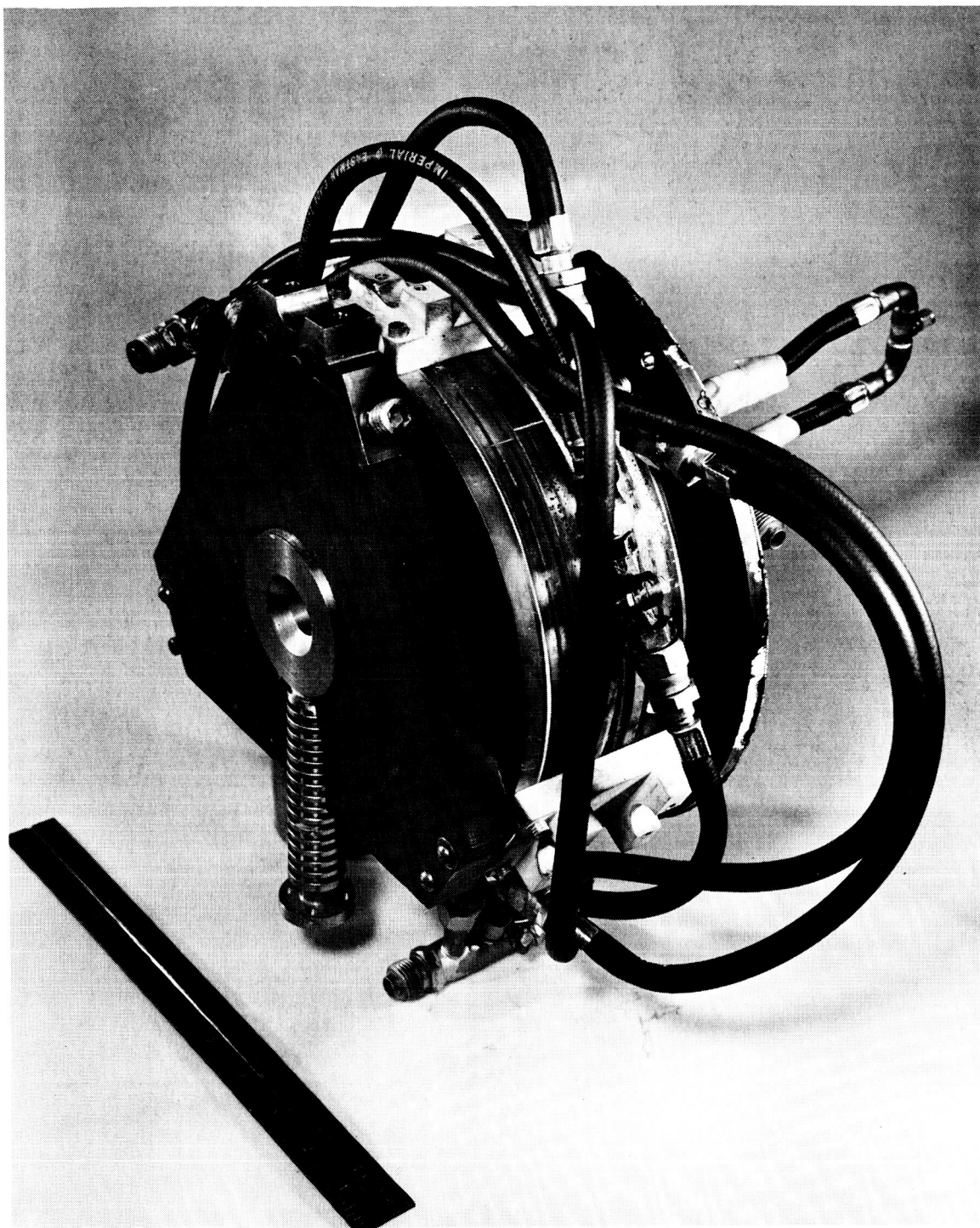
Figure 2. Photograph of ALPHA Thrustor with Front Magnet Removed

Figure 3. ALPHA Thrustor (Model LAJ-AF-CG-2B with GAF IV Feed)
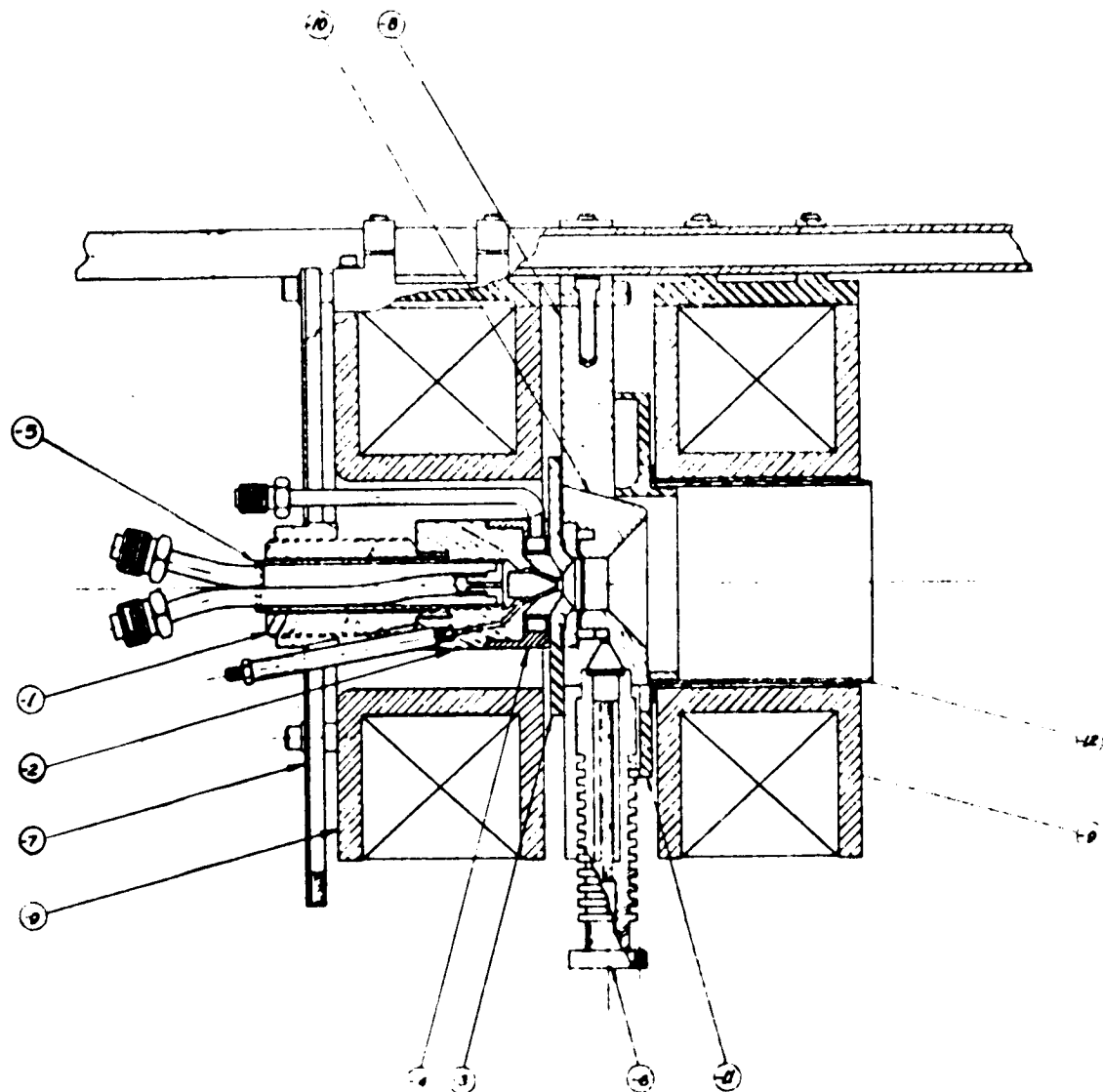
			71C 587	
1	12	-542	HOT LINER	MOLY-TUNGSTEN
1	11	-500	MAGNET INSULATOR	BORON NITRIDE
1	10	-585	ANODE	TUNGSTEN
2	9	-584	ELECTROMAGNET	COPPER-EPOXY
1	8	-580	RADIATOR	GRAPHITE
1	7	-528	SPRING PLATE	316 STAINLESS
1	6	-585	VAPORIZER	MOLYBDENUM
1	5	-520	CATHODE ASSEMBLY	TUNGSTEN-COPPER
1	4	-585	BUFFER ASSEMBLY	. . .
1	3	-584	BUFFER INSULATOR	BORON NITRIDE
1	2	-523	CATHODE . . .	. . .
1	1	87C 522	REAR .	. . .
			LIST OF MATERIALS	

Figure 4. Gas-Actuated Lithium Feed System
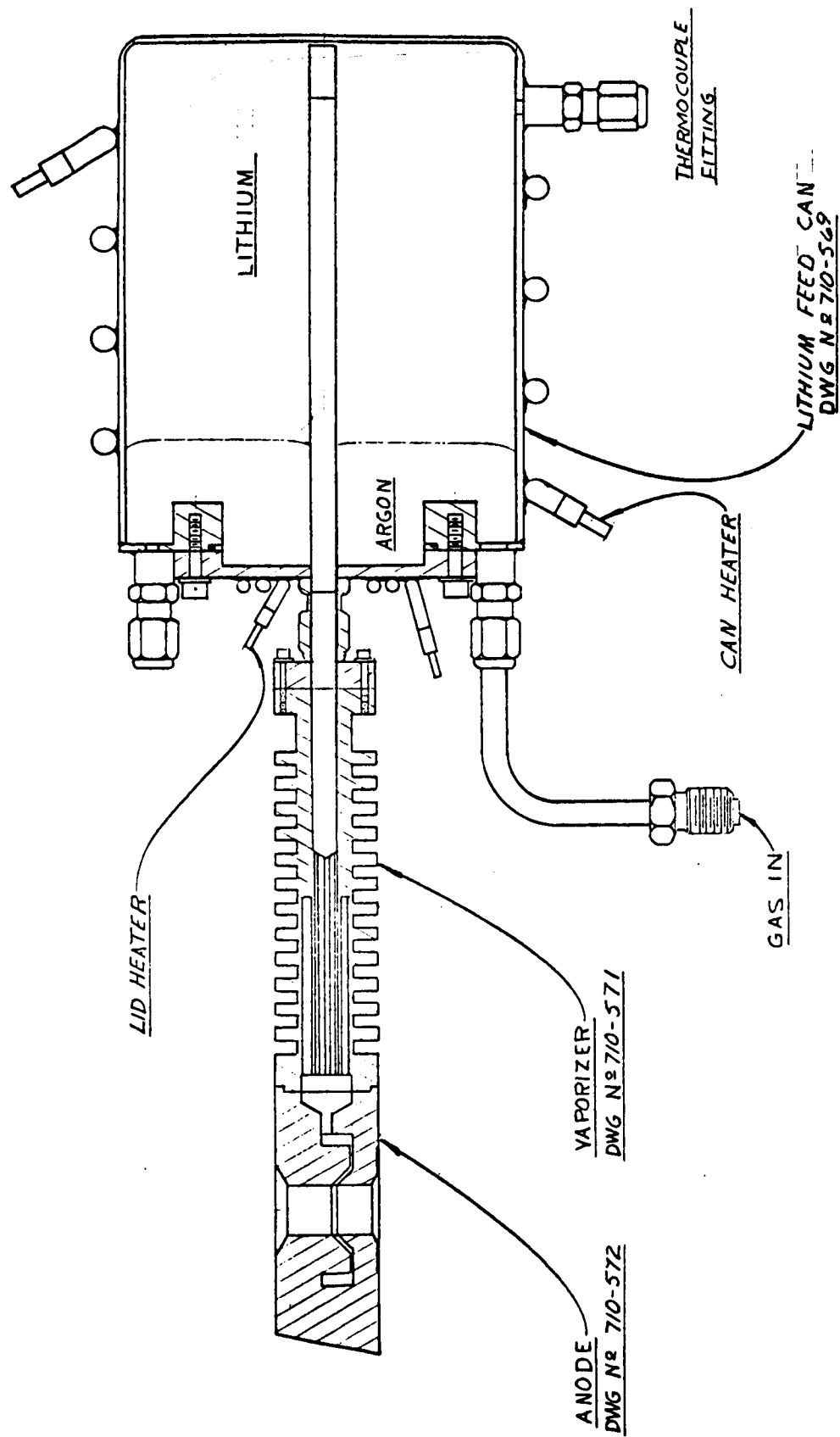
Figure 5.   Lithium Feed System for ALPHA (GAF-2-A)

Since most of the recent experimental studies at EOS have been concerned with alkali metal propellants, this program was confined to the ALPHA device. This device was operated, during this program, primarily with lithium propellant, and, to a lesser extent with sodium. As mentioned earlier, the primary purpose of this program was a series of detailed diagnostic experiments in and around the plasma exhaust of ALPHA. Wherever possible the experiments were performed with parametric variation of one or more of the main ALPHA parameters (viz., mass flow rate, arc current, and magnet current). The great advantage of parametric testing is the significant increase in the confidence with which one views experimental results when they are not only capable of generating "reasonable numbers" at a given operating condition, but also correct trends as one moves to other sets of conditions.

Finally, the research was also directed at improving the knowledge of the basic phenomena of the acceleration process. While this is certainly an ambitious goal, a number of the results appear to shed modest light on the behavior of some of the many complicated phenomena which occur with the plasma.

SECTION 3

ALPHA PERFORMANCE MEASUREMENTS

3.1 MEASUREMENT OF THRUST

3.1.1 THRUST BALANCE

The thrust balance suspension mechanism is a parallelogram formed by
a fixed upper plate, flexured support bars and a free lower plate to
which the thrustor is attached. The support bars have Bendix-type
cross-strung flexures at each end which form the pivot points. The
thrust is sensed by an unbonded strain gage force transducer mounted
on the lower plate and connected by a pneumatically operated latch to
a vertical tube which is mounted to the upper plate. The entire mech-
anism is designed so that the principal stiffness (force resisting the
applied thrust) is that of the transducer, i.e., $F_{s\,Transducer} \gg$
$F_{s\,Pendulum} + F_{s\,Flexure}$.

Electrical power for the arc and magnet coils is brought across the
balance through coaxial, mercury-filled pots which offer no mechanical
resistance to balance translation. The coaxial design eliminates tare
forces due to magnetic field interactions. Cooling water is transported
to and from the thrustor in long stainless steel U-tubes which minimize
the tare forces and vibrations to the balance. Similar techniques are
used for gas and signal leads. A photograph of the thrust balance and
ALPHA thrustor is shown in Fig. 6. Figure 7 is a detailed drawing of
the thrust balance assembly.

The range of thrust measurements using this balance is limited primarily
by the range of the force transducer. Presently, a 100-gram full-scale
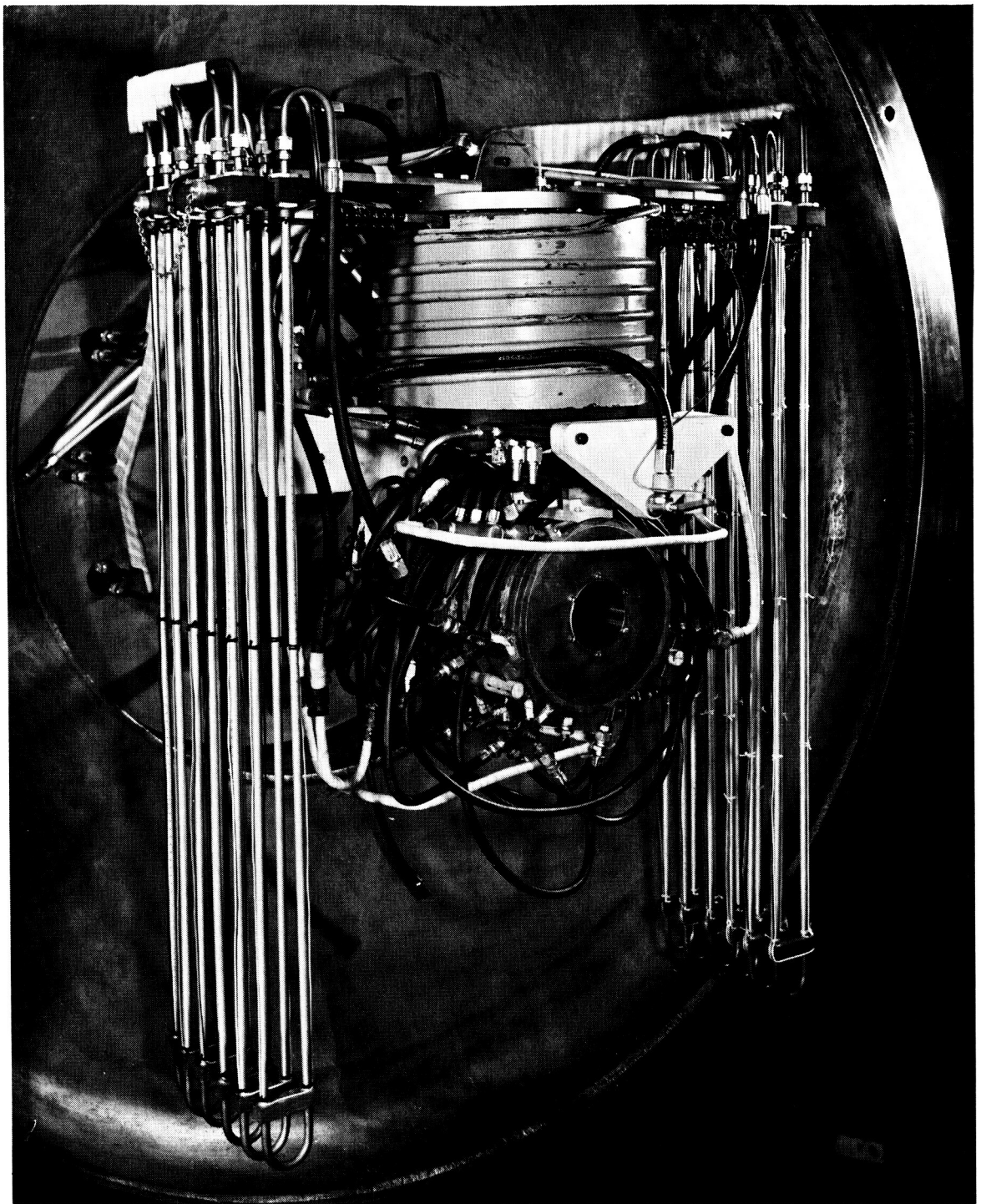
Figure 6. Photograph of Thrust Balance and ALPHA Thrustor

SP-126620
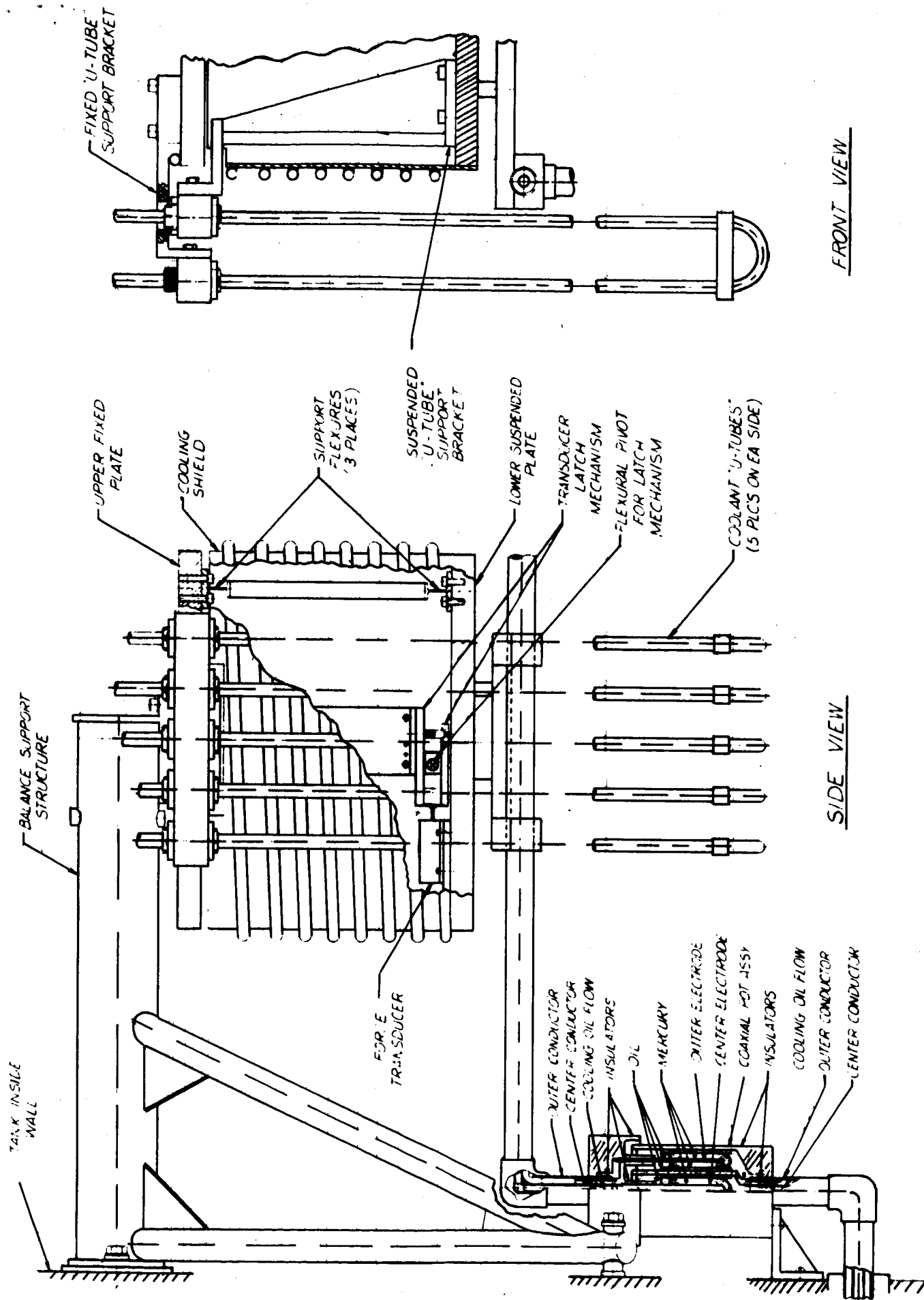
Figure 7. Thrust Balance with Coolant U-Tubes

FRONT VIEW

FIXED U-TUBE SUPPORT BRACKET

SIDE VIEW

UPPER FIXED PLATE

COOLING SHIELD

SUPPORT FLEXURES (3 PLACES)

SUSPENDED U-TUBE SUPPORT BRACKET

LOWER SUSPENDED PLATE

TRANSDUCER LATCH MECHANISM

FLEXURAL PIVOT FOR LATCH MECHANISM

COOLANT U-TUBES (5 PLCS ON EA SIDE)

BALANCE SUPPORT STRUCTURE

FORCE TRANSDUCER

TANK INSIDE WALL

OUTER CONDUCTOR
CENTER CONDUCTOR
COOLING OIL FLOW
INSULATORS
OIL
MERCURY
OUTER ELECTRODE
CENTER ELECTRODE
COAXIAL POT ASSY
INSULATORS
COOLING OIL FLOW
OUTER CONDUCTOR
CENTER CONDUCTOR

transducer is used. The estimated probability error in measurements taken within this range is ±1/2-1 gram. The principal source of error is zero drift of the transducer, due chiefly to distortion and shifting of the tank, support frame and balance mechanism when exposed to nonuniform heating during testing. Other minor error sources are transducer temperature effects, mechanical hysteresis, Lorentz forces between power leads, and center-of-gravity shifting. Considerable effort has been devoted toward minimizing these errors. These include providing a constant temperature oil bath for the transducer and flexures, careful positioning of the power leads, and cooling/shielding of the support and suspension components.

3.1.2 CALIBRATION

Five types of calibrations are performed before each thrustor test. The balance sensitivity and hysteresis is determined by dead weight calibration, using gram weights applied to the balance over a precision pulley. Hysteresis values are typically less than 1/4 gram, as determined by the difference in recorder deflection when ascending and when descending at any weight level.

The effects of the magnetic coil on thrust output are noted over the range of coil currents to be tested. Then a cathode-to-anode shorting fixture is installed and the interaction effects of arc and coil current are determined. Lastly, measured flow rates of cold gas, usually argon, are injected into the cathode gas feed annulus and a determination of thrust produced.

These calibrations are applied as corrections to the data produced during thrustor tests. Zero-drift effects, which occur primarily in the first few minutes of any test, are brought into account by shutting the thrustor off momentarily and noting the new zero position of the thrust recording pen.

3.2 MEASUREMENT OF MASS FLOW

3.2.1 GAS-DRIVEN FEED SYSTEM

The lithium feed system employed in the accelerator tests is an inert gas-actuated scheme developed recently on Contract AF 33(615)-1579. The design approach is based on equilibrating the vapor pressure of lithium upstream of a metering orifice to the argon driver pressure in the lithium reservoir. The sonic vapor flow rate through the orifice can then be calculated from measurements of the applied argon pressure. This eliminated the necessity for measuring actual lithium vapor pressure at high temperatures, or deriving vapor pressure from measured temperatures. The latter procedure would be of questionable accuracy since it involves temperature extrapolations and a very sensitive pressure-temperature relationship.

The actual feed system, shown in Figs. 4 and 5, consists of a molybdenum vaporizer, stainless steel reservoir and external pressurization controls. Lithium is maintained in its liquid state in the reservoir by electric heaters. A carefully measured pressure of argon gas is maintained over this liquid by the external circuit which has provisions for rapidly changing the pressure as well as fine bleed controls. This gas pressure forces liquid lithium through the porous filter and up into the vaporizer. The vaporizer is heated by conduction from the tungsten anode and is furnished with a narrow cross section midway from the top which contains several small diameter holes. The temperature gradient established down the length of the vaporizer consists of a relatively uniform high temperature just below the anode, a very sharp gradient across the narrow midpoint, and a slight gradient below, which is aided by peripheral radiation fins and conduction to the reservoir.

Lithium vaporization is to occur only in the small diameter holes by virtue of the high temperature gradient in this region, the high lithium surface area-to-volume ratio and the large heat storage capacity of the region just above. Localization of the lithium state-change region contributes to the dynamic stability of the system, as does the restriction to large liquid excursions presented by the porous filter.

Vapor produced in the high gradient region is superheated slightly before passing through the metering orifice, then into the anode feed annulus where it is distributed around the circumference of the anode bore, and finally injected into the arc.

3.2.2 CALIBRATION

Initial calibration of feed mass flow rate was based on perfect gas calculations of lithium vapor through the sonic orifice, supplemented by a discharge coefficient obtained by flowing known rates of argon through the orifice. Early thrustor tests showed a considerable discrepancy between these predicted flow rates and those obtained by measurement of propellant weight loss over a given interval of time.

Numerous corrections have now been made to the original theory, resulting in much closer agreement with experimentally obtained flow rates. These include taking into account friction effects, vapor heat addition and variation of γ with temperature and pressure, as well as providing a closer Reynolds number match between calibration gas and actual lithium flow rates in order to improve the discharge coefficient determinations. (Refs. 4 and 14) The theoretical-experimental correlation is not yet perfect, so the lithium and sodium mass flow rates reported for this program are based entirely upon weight change measurements made before and after each test. Long duration runs, such as Nos. 727 and 732, with nearly constant feeder driver pressures, yield probable average errors in flow rates of less than 1 percent. Short

duration runs and/or those which were performed over a wide range of driver pressures may have individual flow-rate errors as great as 15-20 percent. Three major factors contribute to this larger possible error. The lower net-to-gross weight ratio of the feeder decreases the accuracy of weight loss measurements for any given scale resolution. Secondly, there are inherent uncertainties in individual flow rate values obtained by differentiation over the duration of the test, using only end point weights and intermediate driver pressure settings. Also, small quantities of liquid propellant which may be ejected during a flooding condition can usually not be accounted for in the weight loss determination and hence provide higher error sources on short duration tests.

3.3 MEASUREMENT OF EFFICIENCIES

3.3.1 MEASUREMENT OF ARC AND MAGNET POWER

Electrical power inputs to the thrustor arc and magnet coils were determined from measurements of the average applied voltage and current.

Voltage taps were placed as close as possible to the anode, cathode, and coils in order to minimize unmeasured voltage drops in the power leads. The resultant voltage was displayed on an expanded range D'Arsonval meter of 1/4 percent accuracy, and permanently recorded on a galvanometer oscillograph.

Current signals were derived from standard low resistance (25×10^{-6} ohm) shunts and from special Hall effect transducers. The latter device consists of a thin wafer of semiconductor material positioned in the plane of the axis of the power conductor so that the magnetic field lines induced by the current flow in the conductor pass perpendicularly through the wafer. A transverse, or Hall potential will then be

generated whenever a current is passed through the wafer. Since this potential is a function of certain geometric and physical properties of the wafer as well as applied field and current, individual calibrations of each transducer were made. The signal generated by these transducers are particularly adaptable to strip-chart recording since complete isolation from the common mode voltage of the power lead is achieved. Outputs of the standard shunts are read on dc meters similar to the voltage read-outs.

It should be noted here that while the power measurements so far described have considered only average dc quantities, it is recognized that time-varying voltages and currents are involved. The major factor is the applied voltage and current ripple developed in the power supplies, predominately 360 Hz. The instrumentation just described will not provide accurate indications of the instantaneous power. For instance, the rms voltage drop across the standard shunts would be approximately 35 percent higher for 360 Hz than for dc currents. The D'Arsonval meter coil assemblies have a period of oscillation greater than one second, and hence very little response to ac signals of over 10 Hz. These are not felt to be critical shortcomings, however, since the voltage ripple emanating from the power supplies (as determined by high response oscilloscope investigations) is only a few percent of the average dc voltage. Hence, the product of average voltage and average current will approximate the total power consumed within 1 percent. The effects of power supply ripple on diagnostic measurements are discussed in later sections.

3.3.2 MEASUREMENT OF COMPONENT POWER LOSSES

Component power losses of the MPD thrustor were determined by measuring the heat input to the individual cooling circuits. This is accomplished by recording the water flow rates and temperature rises through the cathode, buffer and magnet coil housings.

7053-Final   24

The volume flow rates of cooling water were measured with sharp-edged orifice type meters, using edge pressure taps. The pressure differentials produced were monitored with mercury-filled U-tube manometers. Sufficient differential head for fine resolution was insured by selecting the smallest diameter orifice plate permissible within the full scale capabilities of the manometer. The entire flow metering system was calibrated by directly weighing the water which flowed during a long, measured interval of time. The probable error in water flow rate measurement does not exceed ±2 percent.

The water temperature rises were measured with differential thermocouple circuits. Copper-constantan couples were used primarily because the copper leg is readily compatible with common connectors, terminals and cable materials and hence lends itself well to differential-type circuits without the use of special compensating components in order to avoid extraneous thermoelectric potentials. The millivolt signals generated by the differential thermocouples are displayed by integrating digital voltmeters. These instruments have a resolution of one microvolt per digit and a common mode noise reduction of at least 140 dB. The solid-state circuitry employed has proven very effective in eliminating superimposed noise and displaying true integral values.

It is estimated that the total power loss measurement is accurate to within 3 percent, with the water flow rate measurement being the major error contribution.

3.4 DEFINITION OF EFFICIENCIES

Since there is often some question as to the exact definition of "an efficiency," we shall define, as unambiguously as possible, the three efficiencies which are referred to in the data presented in Appendix A.

3.4.1 THERMAL EFFICIENCY

The thermal efficiency, designated as $\eta_{thermal}$, is defined by the expression

$$\eta_{thermal} \equiv \frac{P_{net}}{P_{arc}}$$

where

$$P_{net} \equiv P_{arc} - P_{losses}$$

and P_{arc} is the electrical power supplied to the arc (but not including the power supplied to the magnets) and P_{losses} is the sum of the cathode, buffer and anode power losses.

3.4.2 THRUST EFFICIENCY

The thrust efficiency, designated as η_{thrust}, is defined by the expression

$$\eta_{thrust} \equiv \frac{P_{beam}}{P_{arc}}$$

where $P_{beam} = T^2/2\dot{M}$ is the directed beam power associated with the product of the thrust and the effective exhaust velocity. Here T is the engine thrust and $\dot{M}$ the <u>total</u> engine propellant mass flow rate (the sum of the lithium and hydrogen, or sodium and hydrogen, flow rates for the present ALPHA bipropellant thrustor).

3.4.3 OVERALL EFFICIENCY

The overall efficiency, designated as η_o, is defined by the expression

$$\eta_o \equiv \frac{P_{beam}}{P_{total}}$$

where P_{total} is the actual <u>total</u> electrical power delivered to the
entire system (i.e., the sum of the arc power and the <u>actual</u> magnet
power — with no allowance made for future improvements in the reduction
of the magnet power). The overall efficiency is therefore an index of
the actual conversion of the total electrical energy entering the device
into directed kinetic energy of the plasma exhaust.

3.5 <u>PERFORMANCE DATA AND PARAMETRIC TESTING</u>

Extensive parametric testing of the ALPHA device on this program, and
in conjunction with Air Force contract 33(615)-1579, was performed from
March 1966 through May 1967. The body of the data is presented in
Appendix B and also Ref. 4.

The four "controllable variables" during any given test are:

      a.   The arc current
      b.   The magnet current
      c.   The alkali metal flow rate
      d.   The hydrogen flow rate

The **indirect** variables in any test are primarily

      a.   The engine configuration
      b.   The magnet configuration
      c.   The tank configuration
      d.   The background tank pressure

The measured quantities which are directly affected by variations in
the above are:

a. The arc voltage

b. The arc power

c. The component power losses

d. The magnet power

e. The applied magnetic field strength

f. The thrust

g. The specific impulse

h. The thermal efficiency

i. The thrust efficiency

j. The overall efficiency

With so many direct and indirect variables, and so many quantities to be measured, the presentation of parametric data is not a simple matter. Appendix B presents the data in tabular form. Nonetheless, it is always somewhat more convenient to display certain trends in graphic form. Here a question of selectivity becomes apparent. Exactly which quantities plotted versus which variables will best express the most important features of the data is perhaps somewhat subjective. In the interests of a compromise between extreme brevity on the one hand and a ponderous array of data cross-plots of questionable significance on the other, the following graphs of performance data are presented in Figs. 8 through 15.

3.5.1 LITHIUM PERFORMANCE RESULTS

a. Thrust versus Power (arc and magnet)   (Fig. 8)

b. Thrust versus Mass Flow Rate   (Fig. 9)

c. Efficiency versus Mass Flow Rate   (Fig. 10)

d. Efficiency versus Specific Impulse   (Fig. 11)

3.5.2 SODIUM PERFORMANCE RESULTS

a. Thrust versus Power (arc and magnet)   (Fig. 12)

b. Thrust versus Mass Flow Rate   (Fig. 13)

c. Efficiency versus Mass Flow Rate   (Fig. 14)

d. Efficiency versus Specific Impulse   (Fig. 15)
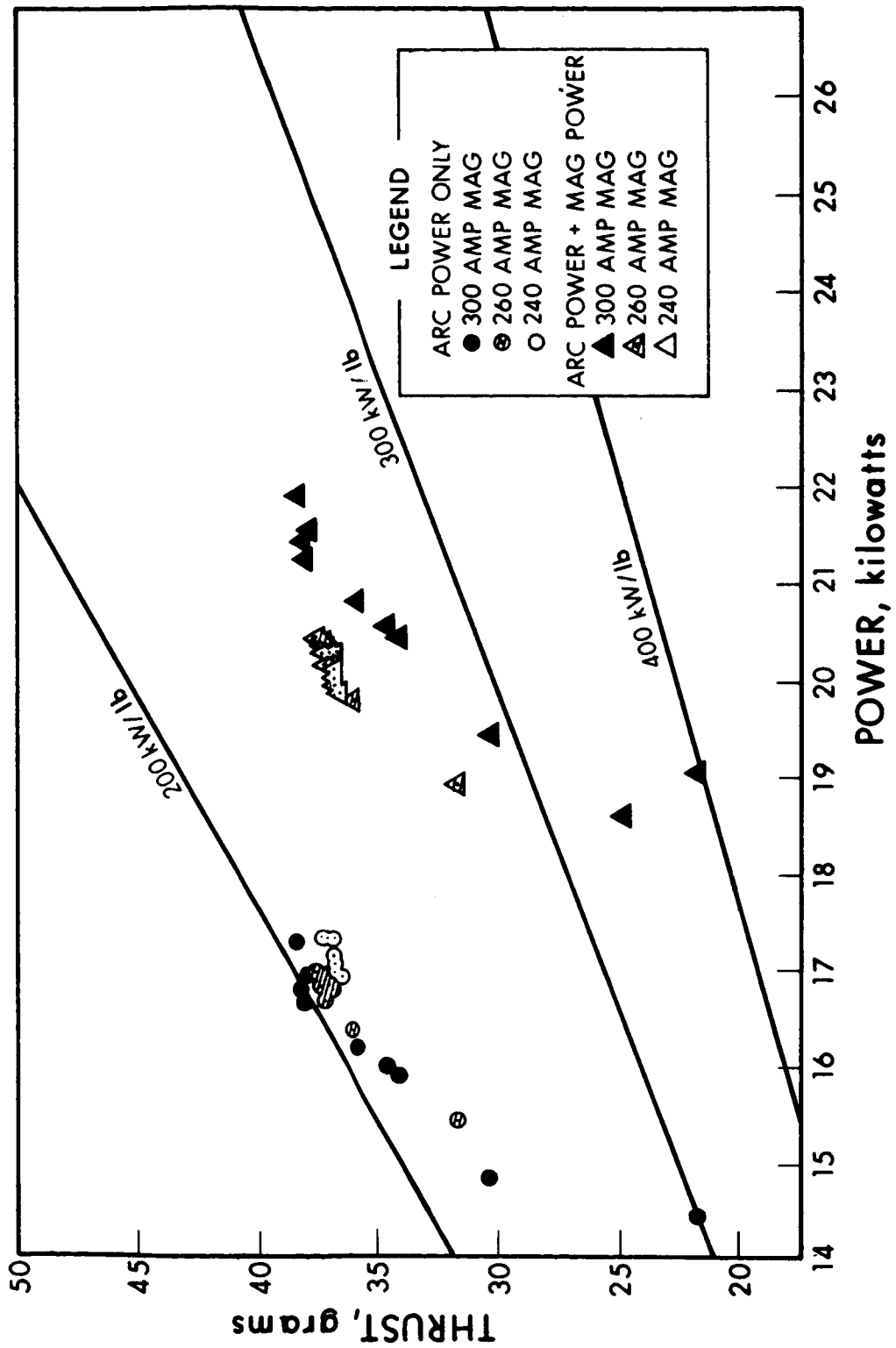
Figure 8. Thrust versus Power for Run 740

73626389
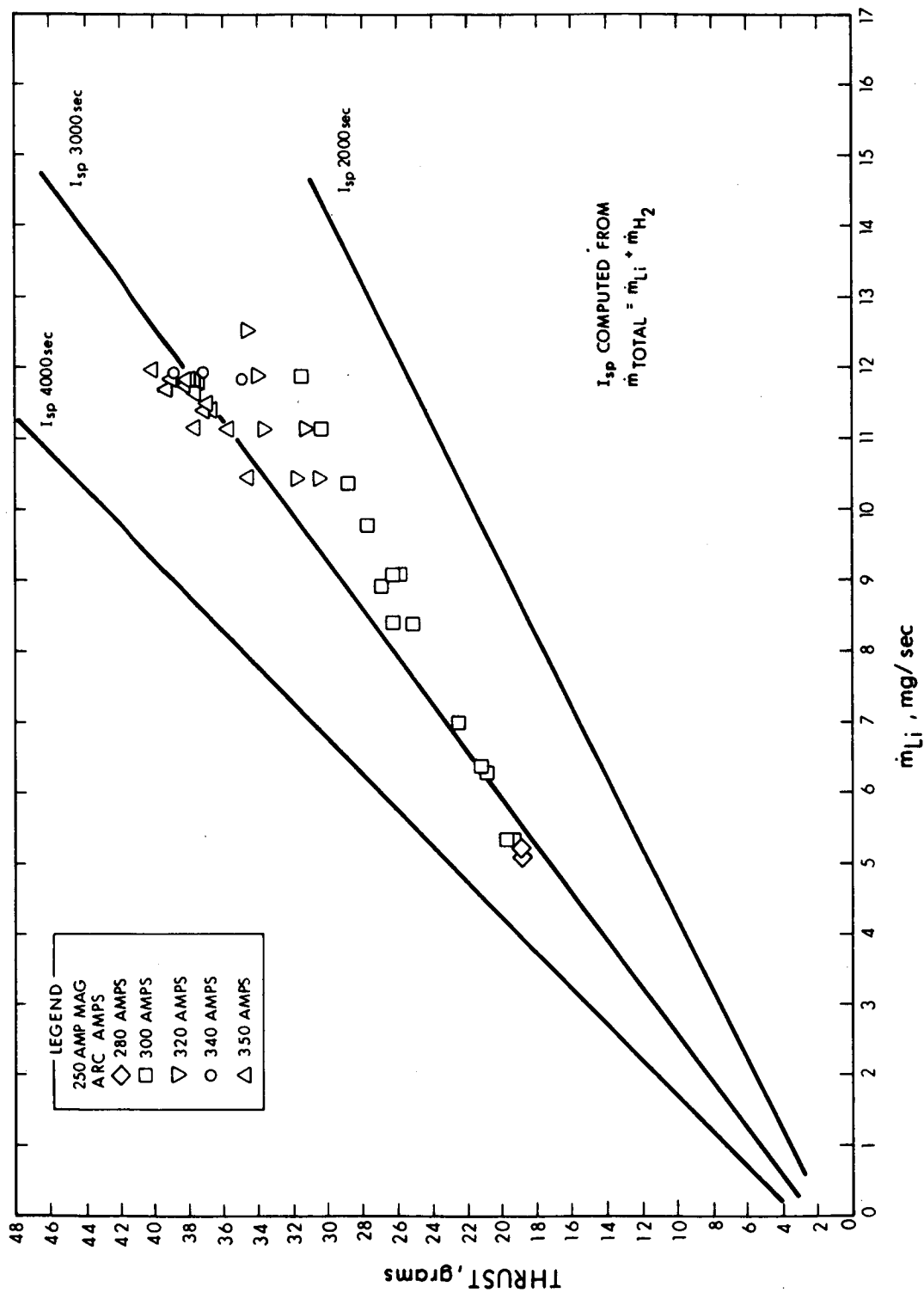
Figure 9. Thrust versus $\dot{m}_{lithium}$ for Run 736

LEGEND

η THERMAL	η THRUST	η_O
▲ 300 AMP MAG	■ 300 AMP MAG	● 300 AMP MAG
△ 250 AMP MAG	□ 250 AMP MAG	○ 250 AMP MAG
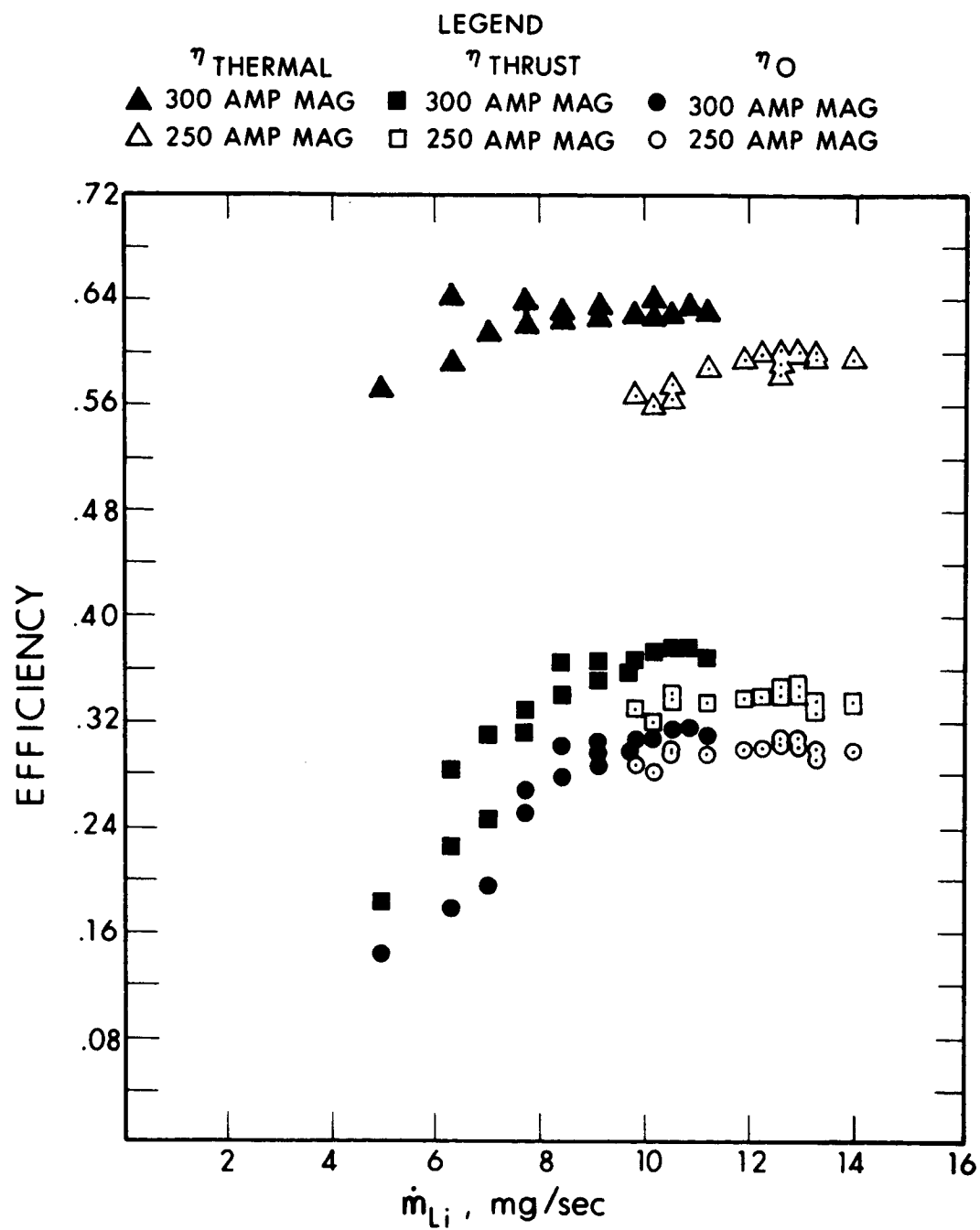
Figure 10. Efficiency versus $\dot{m}_{Li}$ for Run 738

73626391
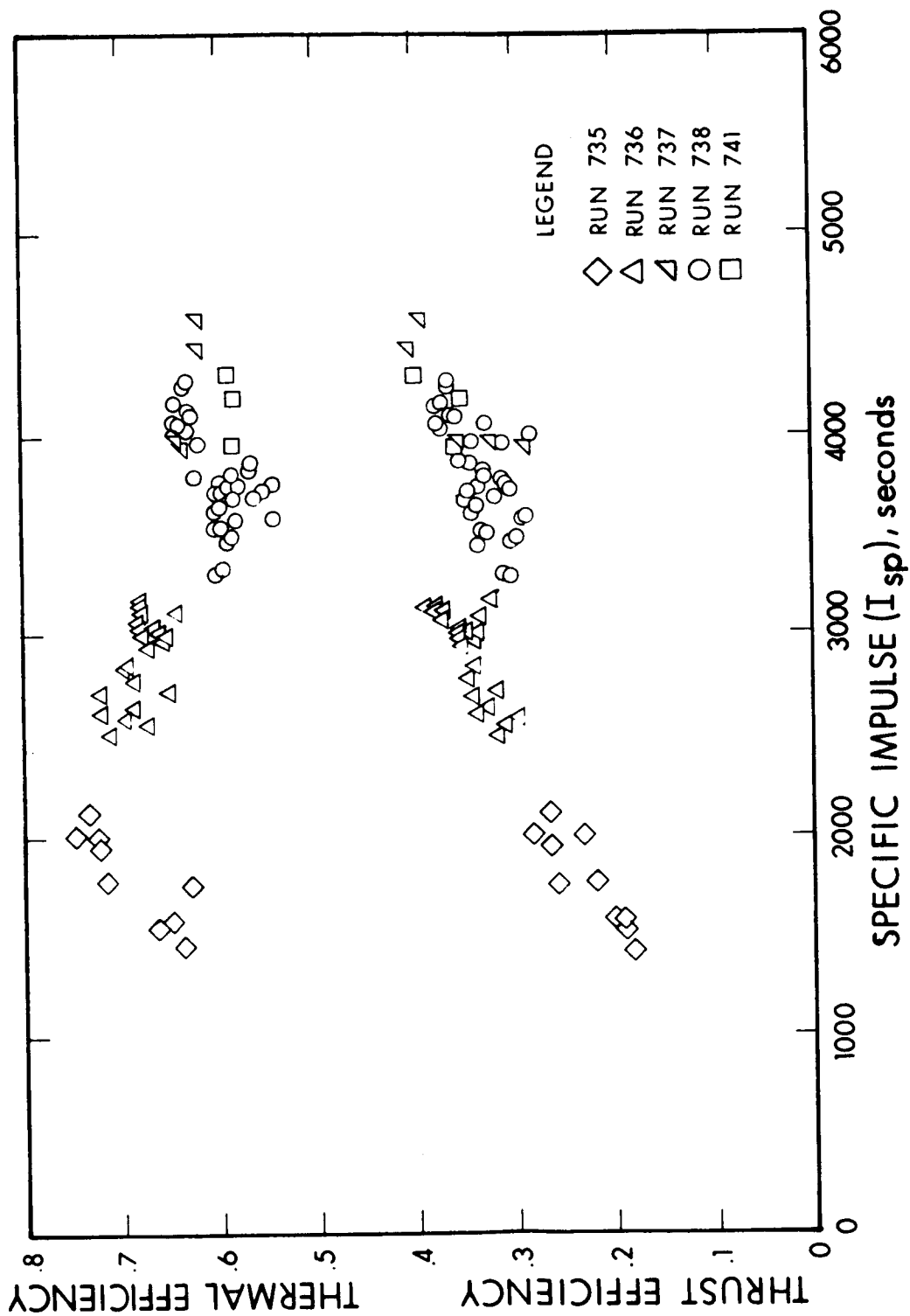
Figure 11. Efficiency versus Specific Impulse for Lithium

Figure 12. Thrust versus Power for Sodium
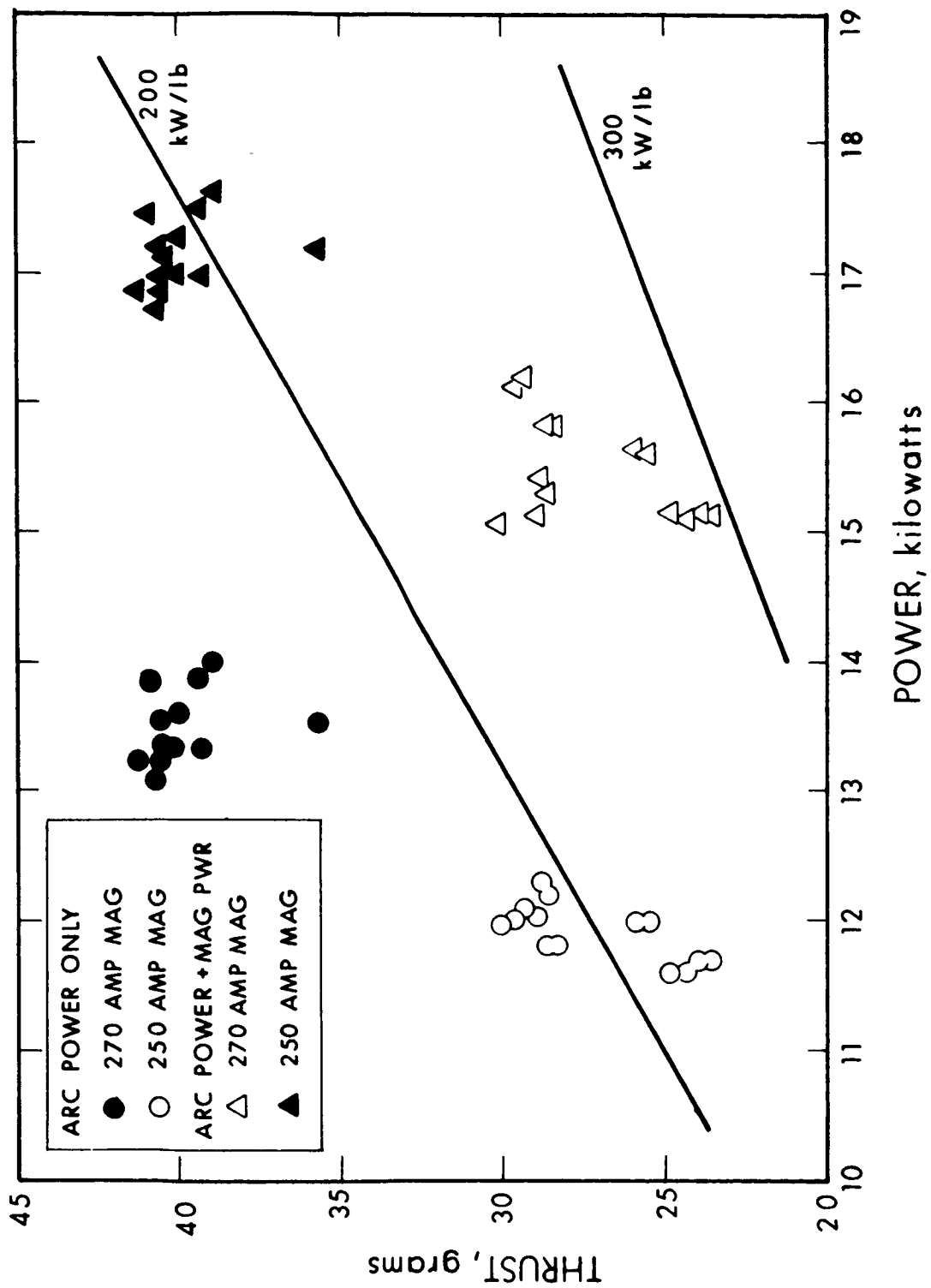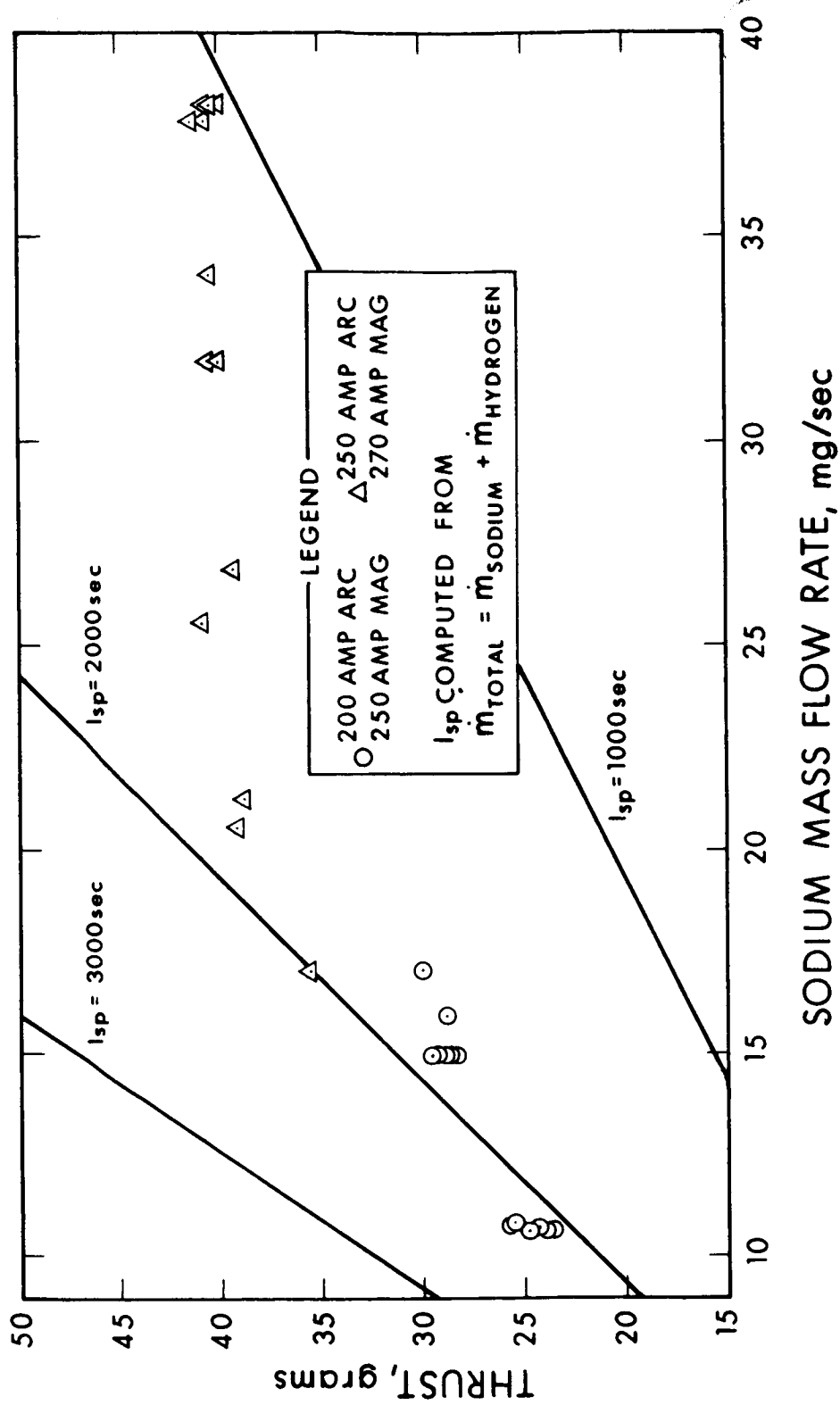
Figure 13. Thrust versus Mass Flow Rate for Sodium

3626601
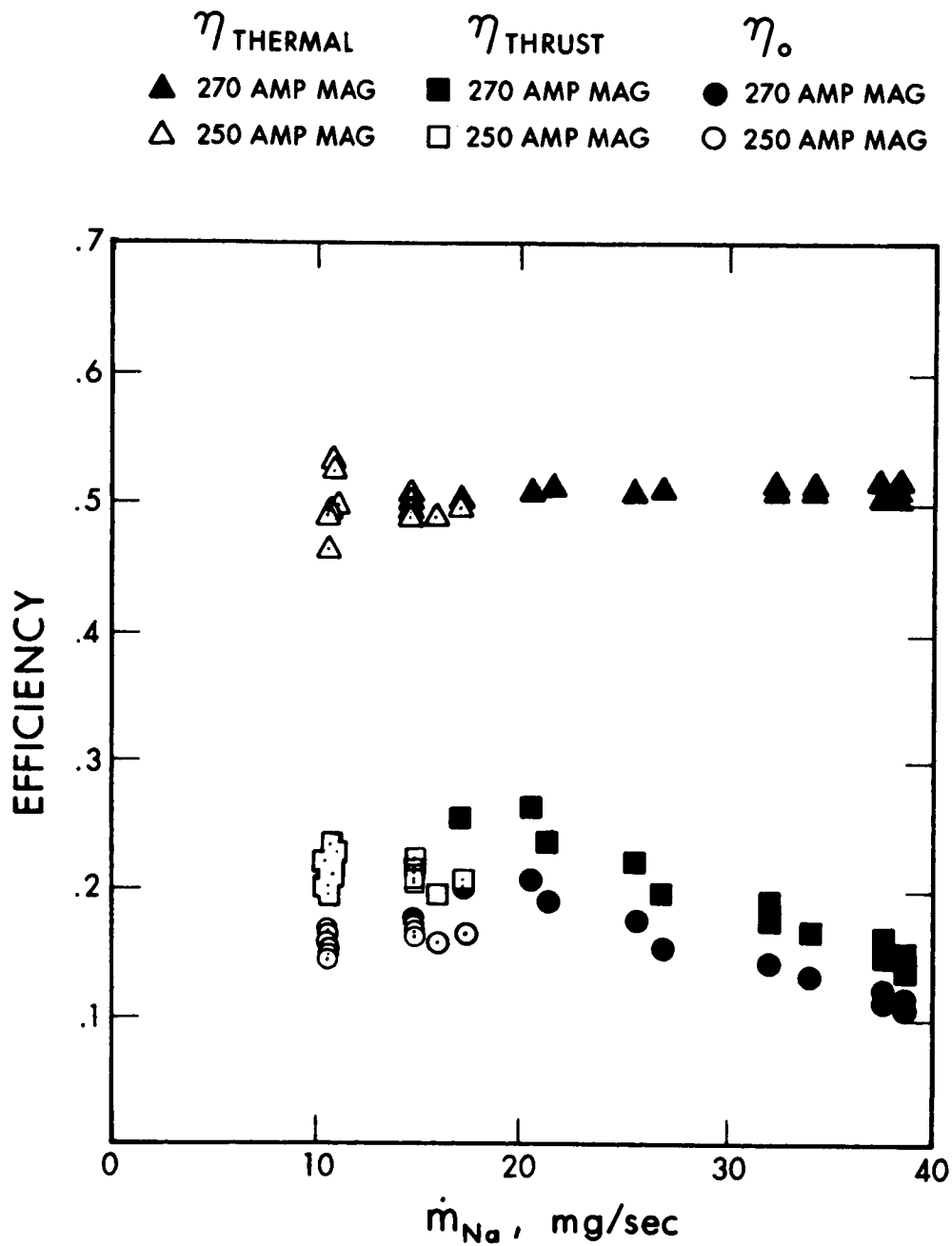
Figure 14. Efficiency versus Mass Flow Rate for Sodium

73626599
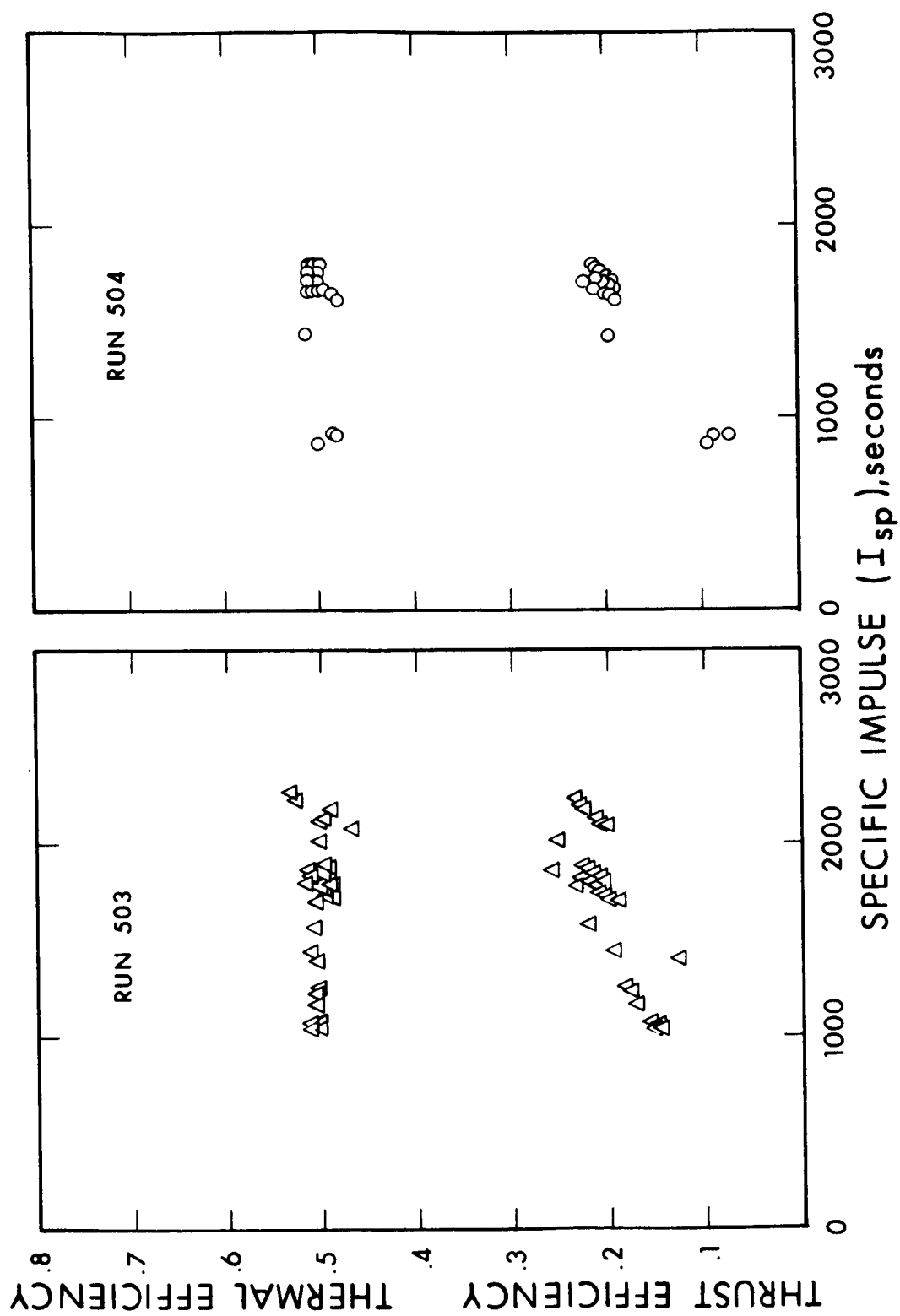
Figure 15. Efficiency versus Specific Impulse for Sodium

SECTION 4

DIAGNOSTIC MEASUREMENTS

4.1 LOCAL ENERGY FLUX

When ALPHA is operating with a condensable propellant, such as lithium
or sodium, it is not possible to use one of the conventional calori-
metric enthalpy probes (Ref. 15). This is primarily due to the fact
that the small central gas sample tube in such probes would rapidly
become clogged with condensed alkali metal, making further measure-
ments impossible.

For this reason a flow swallowing enthalpy probe (Figs. 16 and 17) has
been designed, fabricated, calibrated and operated. This probe con-
sists of two independent water circuits. The outer water circuit pro-
vides general probe cooling and insures probe integrity. The inner
water circuit, using a much smaller water flow rate, determines the
energy flux incident on the frontal opening through simple calorimetry.
The probe has been designed so that the shock wave will remain attached
to the tip. The probe is made of copper and is covered with an outer
boron nitride sleeve and Saureisen cement to provide sufficient insula-
tion to avoid shorting of potential gradients within the plasma. It
is of interest to note that there was <u>absolutely no observable effect</u>
upon the arc jet voltage when the probe was either inserted or with-
drawn from the plasma.

The probe was calibrated in a bench test. This calibration utilized a
critical orifice measurement of the inner passage probe-water flow and
a pair of copper-constantan thermocouples. Power was provided by means
of a small resistance element inserted deep inside the probe. The
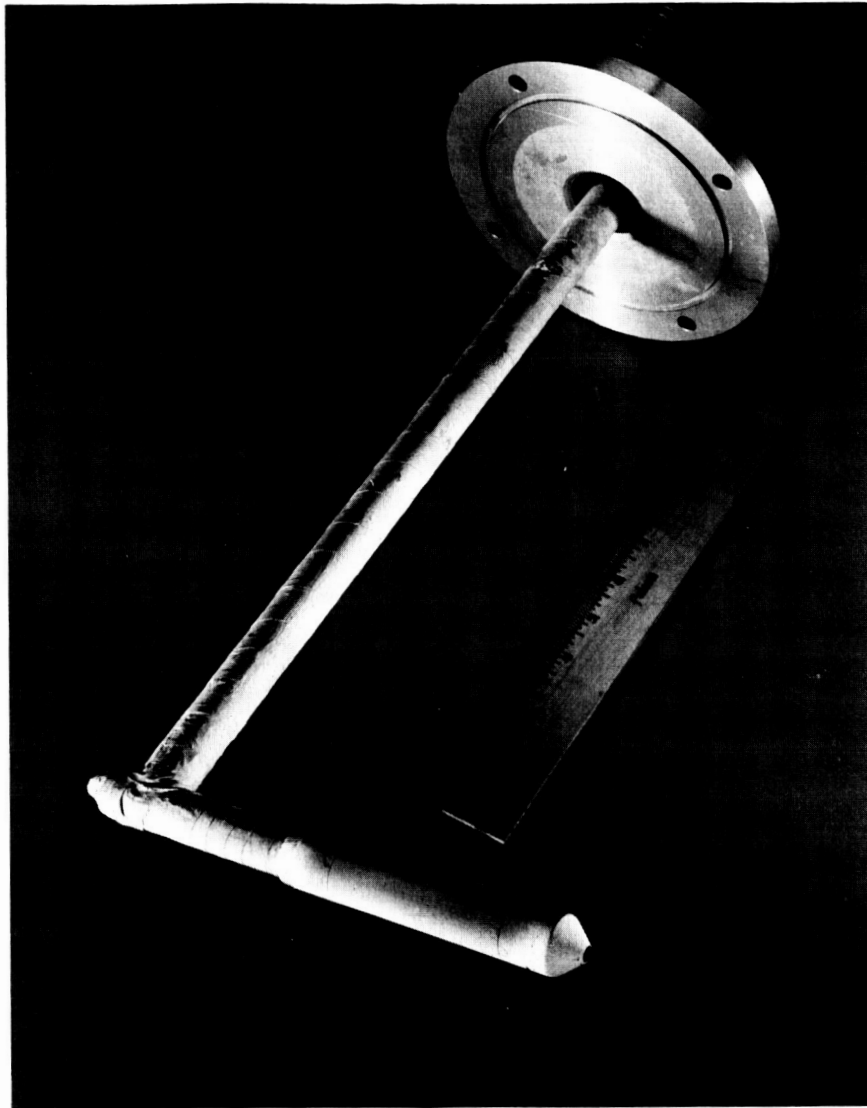
Figure 16. Photo of Energy Probe

INNER CHANNEL (I.C.)

OUTER CHANNEL (O.C.)

LITHIUM

GAS OUT

DELTA H₂O

O.C. IN

I.C. IN

I.C. OUT

O.C. OUT
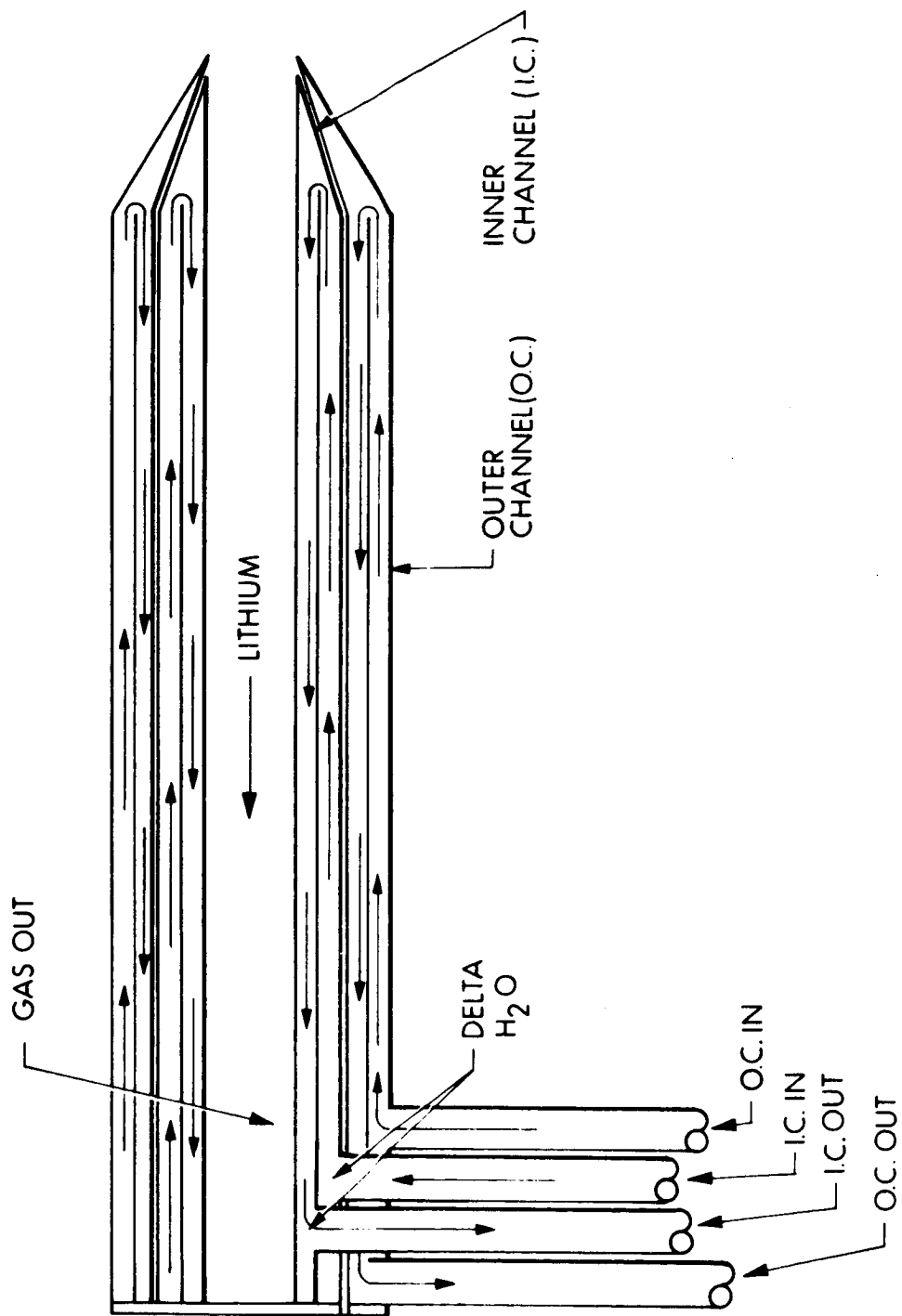
Figure 17. Schematic of Local Energy Flux Probe

73623956

electrical power input was monitored as well as the probe water temperature rise. The results are shown in Fig. 18.

Once the probe had been calibrated it was operated within the plasma exhaust of ALPHA. In the experiment to be discussed the probe was positioned at a given axial station such that the probe sampling orifice was 1.0 meter downstream from the anode face. The probe had a radial degree of freedom between positions 1 inch and 20 inches from the indicated mechanical centerline of ALPHA. The 1-inch limit was unintentional (as opposed to the r = 20-inch upper limit), and was the result of some minor modifications to the tank which forced the positioning of the probe mount 4 inches further from the centerline than had been originally accounted for. Nonetheless, this limitation was relatively minor and detailed radial distributions of the energy flux were measured (see Fig. 19). The repeatability and general steadiness of these measurements were excellent. The thermocouple outputs (both the water ΔT and the exit temperature) were measured with a recording oscillograph and the traces were very steady. About 14 measurements were made at (typically) 1-inch radial increments on each pass. A number of radial passes were made to check repeatability. The traces were so repeatable, in fact, that the major source of the tiny deviations was the gradual drift in the applied arc jet voltages (and therefore, correspondingly, in the arc power) which occurred during the 30 hour run.

Due to the conservative design of the probe, it was observed that the "exit gas" was very well cooled. The exit thermocouple never registered more than 100°C above room temperature, and usually was only about 10°C above room temperature (i.e., "room temperature" referring to the thermocouple output when the arc jet was off). This implies that the energy flux probe was cooling the entrained plasma extremely well. However, due to its large thermal inertia, the probe response was quite slow. Characteristic times of the order of 3 minutes were required at each point before the probe response had steadied to essentially the
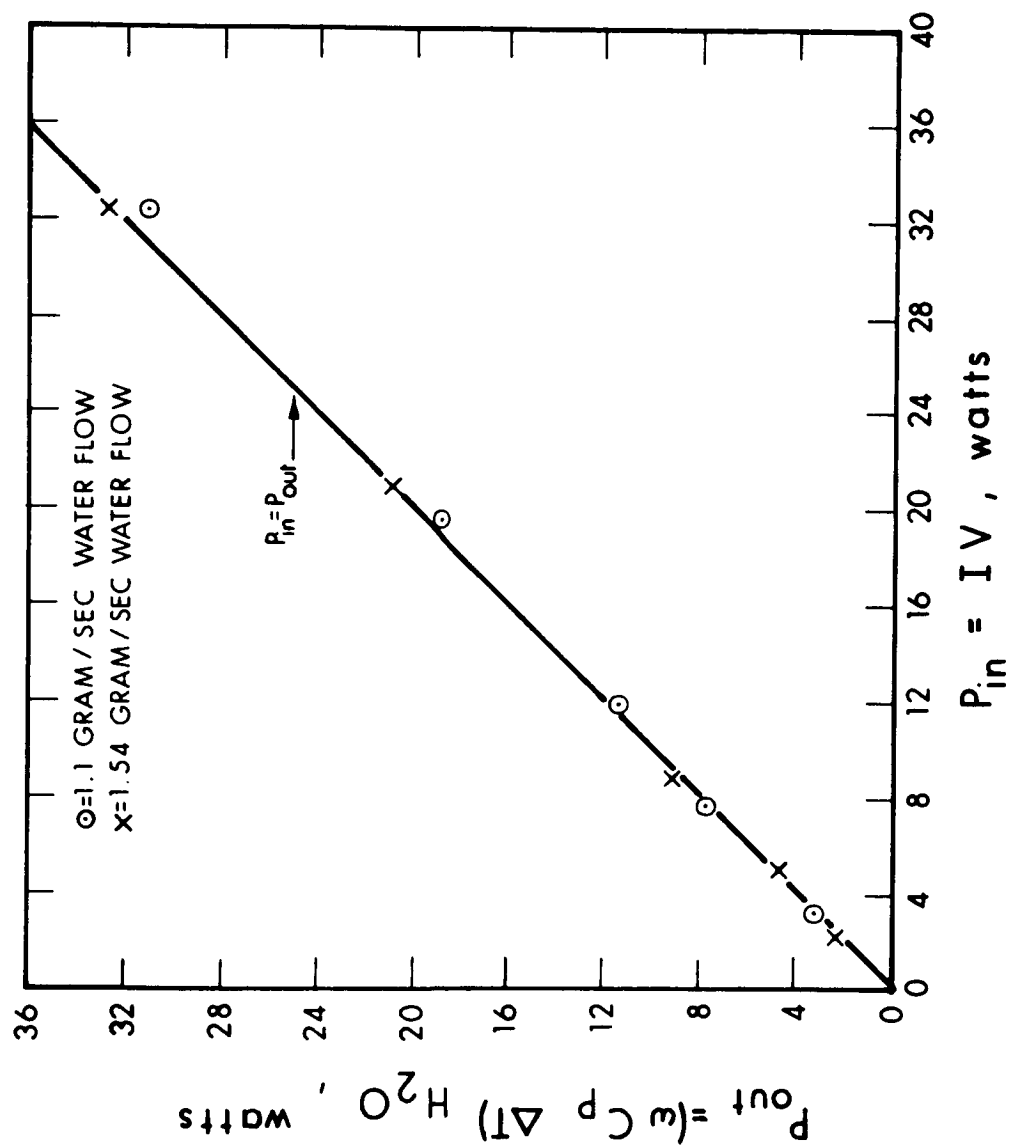
Figure 18. Energy Flux Probe Calibration
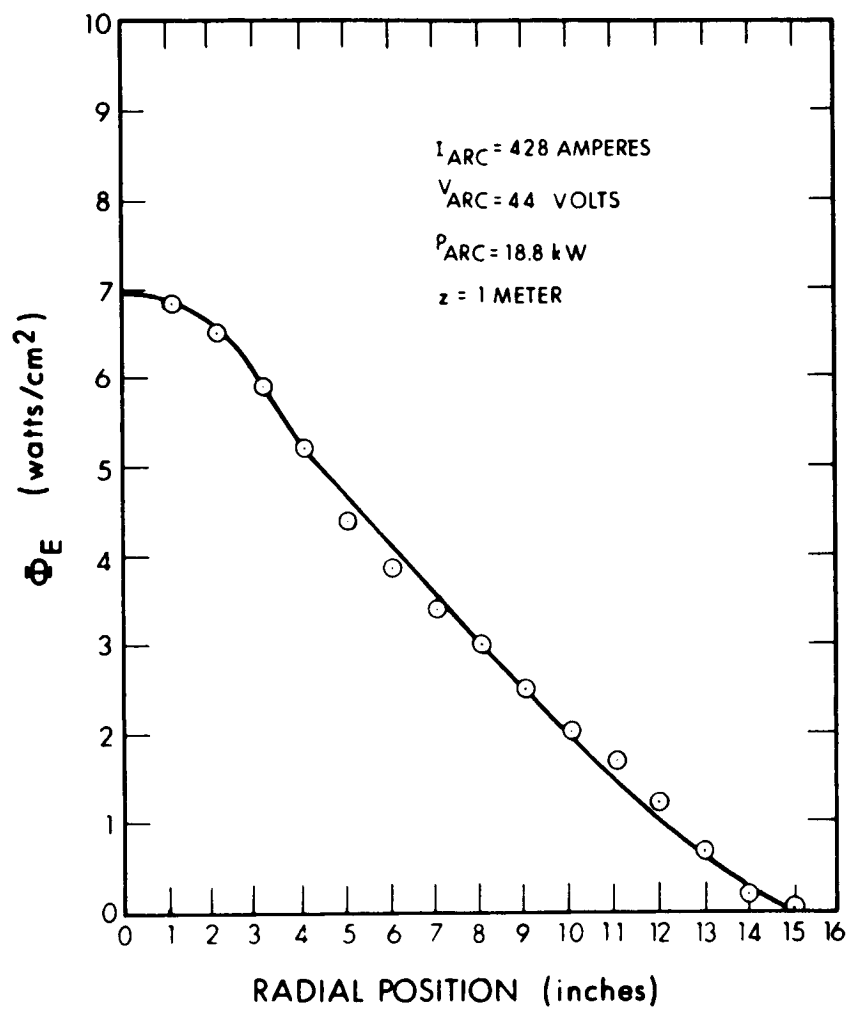
Figure 19. Energy Flux versus Radial Position

73626017

asymptotic values. The asymptotic values were determined by waiting relatively long periods (i.e., 10-15 minutes) at an occasional point. These values compared quite closely with the values obtained after 2-3 minutes, at the same location on a previous radial traverse (viz. errors in repeatability were never greater than 10 percent).

Four significant results of these measurements are:

  a. The typical value of centerline energy flux (energy per unit time per unit area) at a position 1 meter downstream of the anode is about 7 watts/cm^2 when the arc is operating at 428 amps, 44 volts, 18.8 kW, approximately 7 mg/sec of lithium, 1 mg/sec of hydrogen, and a background pressure of 10^{-4} torr.

  b. The energy flux distribution is surprisingly broad. Measurable and repeatable energy fluxes are detected as far out as r = 14 inches (from the centerline), for the conditions described above.

  c. The radial profile of the energy flux distribution shows an approximately <u>linear</u> decay of Φ_e with increasing radial position out to about r = 14 inches.

  d. A numerical integration of the energy flux distribution, over the beam cross section, was performed to obtain the total beam power.

$$P_{beam}^{*} = 2\pi \sum_{r=0}^{r=R} \Phi_e \, r\delta r$$

Also, the beam power was determined from the input power and cooling losses.

$$P_{beam} = P_{input} - P_{losses}$$

The self-consistency of the energy flux measurements is best illustrated by the comparison of the values of P_{beam}^{*} and P_{beam}. For a typical case discussed above, the numerical integration of the energy flux probe data gave

$$P^{*}_{beam} = 9.7 \text{ kW}$$

The input power was 20.6 kW. The total power losses amounted to 11.35 kW. This yields

$$P_{beam} = 9.25 \text{ kW.}$$

The relative integrated error is thus less than 5 percent.

Some characteristic values associated with the energy-flux probe are:

Sampling Diameter	=	0.25 inch
Sampling Area	=	0.32 cm^2
Maximum Diameter	=	1 inch
Inner Water Flow	=	0.6 grams/sec
Outer Water Flow	$\simeq$	20 g/sec
Thermocouple Output	=	45 μvolts
Total Power into Inner Water	$\sim$	2.3 watts
Energy Flux	$\sim$	7 watts/cm^2

An analysis of the thermal effects of lithium-hydrogen chemical reaction within an energy-flux probe is presented in Appendix A. It is clear that, for these experiments, the effects of chemical energy release are negligible relative to the flow energy (typically being of the order of 3 percent).

4.2 TOTAL BEAM CALORIMETER

The total energy of the exhaust beam from ALPHA was measured with a segmented, water-cooled, beam calorimeter developed on this program. A photograph of the device, mounted within the vacuum tank, is shown

in Fig. 20. The total beam calorimeter was operated at a number of different axial positions between 0.5 and 1.25 meters downstream from the anode face. These positioning limits arise for two entirely un-related reasons. When the total beam calorimeter was positioned closer than about 50 cm from the anode face of ALPHA a phenomena similar in appearance to a glow discharge is observed on one or more segments. The calorimeter was specifically designed with electrical insulation between the segments. In fact, the design incorporates a "shadow-shield" concept to avoid shorting of radial electric fields, which may exist within the plasma, through the somewhat subtle mechanism of lithium deposition creating a high conductivity path on the surface of what was initially an insulator. Nonetheless, anomalous behavior was observed under these conditions and it was decided not to employ the total beam calorimeter at positions closer than 50 cm from the anode. It is of interest to point out, however, that although the axial move-ment of the total beam calorimeter had negligible effects upon the thrust measurements, or the arc voltage, the magnetic loop probe output was influenced by these movements, as will be discussed in Section 4.6. The upper "limit" of 1.25 meter was not a sharply defined one. Since there is some radial spreading of the plasma exhaust beam there will, in general, exist some position beyond which a fixed diameter calori-meter will no longer intercept the entire beam. It was distinctly clear that this was occurring for positions beyond 1.25 meters from the anode and, to a lesser extent at positions even closer than this. This limita-tion is evident in the data of Table I, and in Figs. 21 and 22 which show respectively the distribution of power to the various segments, and the variation of total measured beam power with position. The vertical bands on Fig. 22 indicate the extremes of the net beam power, measured by subtracting component power losses from the input electrical arc power. The extent of the bands indicates the temporal variation of the thermal efficiency throughout a run. Neglecting the contribution of the radiation lost from the plasma, the curves of Fig. 22 should

TABLE I

TOTAL BEAM CALORIMETER

Propellant	Run No.	Δp (psi)	$\dot{m}$(gpm)	z(meters)	P_{Beam}(kW)	P_{Net}(kW)
Lithium	732	8.0	1.41	0.73	5.05	6.2
Lithium	732	10.0	1.58	0.73	4.84	6.1
Lithium	732	4.0	1.01	0.73	5.00	6.2
Lithium	732	4.0	1.01	0.73	4.94	6.1
Lithium	732	4.0	1.01	0.85	4.26	6.2
Lithium	732	8.5	1.46	0.51	5.95	6.2
Lithium	732	8.5	1.46	0.51	5.98	6.2
Lithium	732	8.5	1.46	0.51	5.93	6.2
Sodium	504	10.2	1.60	1.25	1.25	5.7
Sodium	504	10.2	1.60	0.82	2.80	5.7
Sodium	504	6.0	1.24	0.75	3.51	5.5
Sodium	504	6.0	1.24	0.51	4.75	5.5
Sodium	504	35.0*	0.75	0.82	2.78	5.7
Sodium	504	35.0*	0.75	0.51	4.97	5.7

* The orifice diameter was reduced from 0.169 inch, on all other points, to 0.086 inch on these points.
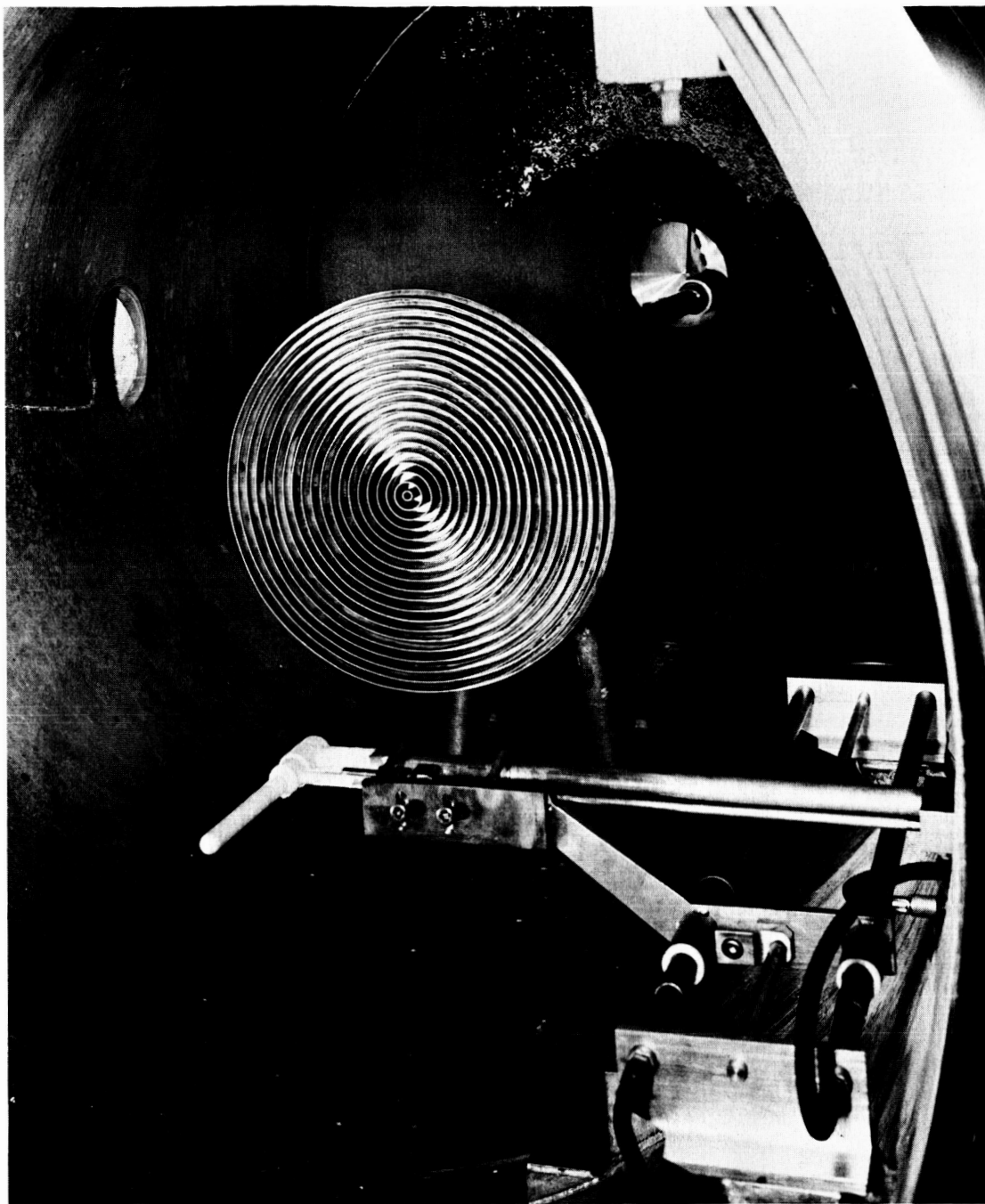
Figure 20. Photograph of Total Beam Calorimeter and Hall-Effect
Magnetic Probe
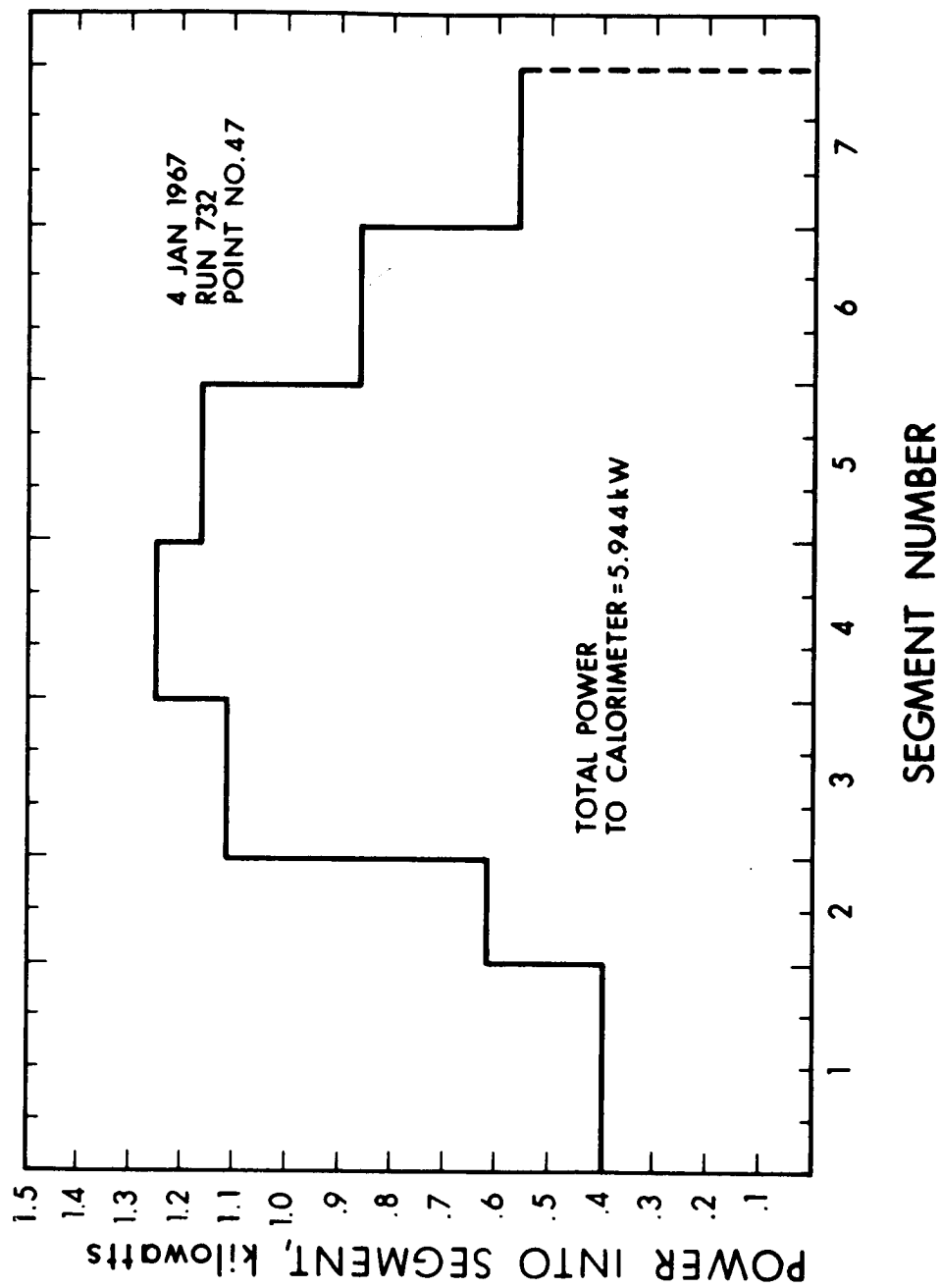
Figure 21. Power Distribution to Segments of Total Beam Calorimeter
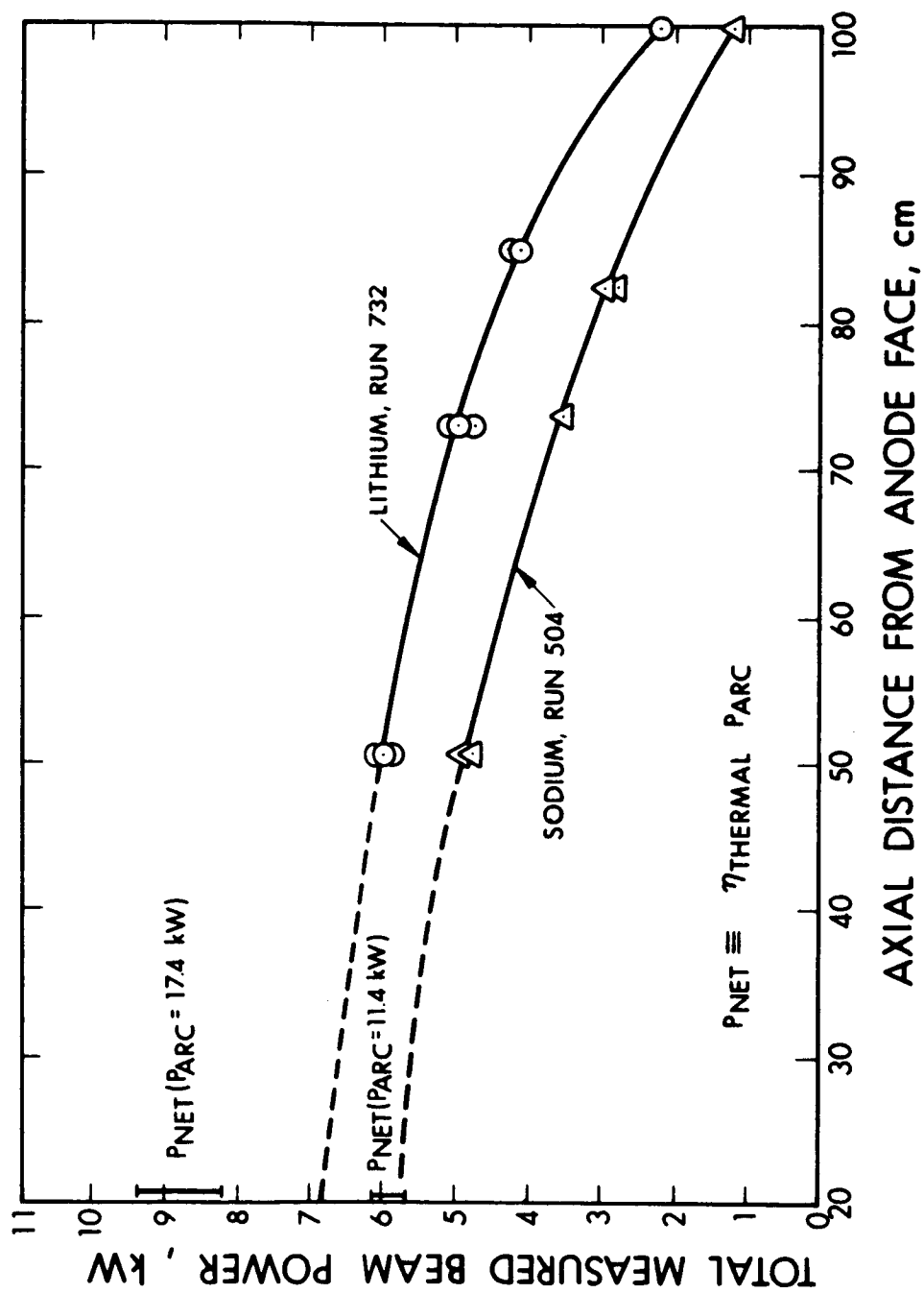
Figure 22. Total Beam Calorimeter Power versus Axial Position

73626591

extrapolate backwards to a point somewhere within this band (depending on the particular efficiency at the instant of the measurement) when z approaches zero. Unfortunately, this can be done mathematically but not physically for the reasons described earlier. Nonetheless, the extrapolation errors are reasonably small and are consistently on the low side (i.e., the calorimeter detects slightly less power in the beam than the input power minus coolant losses) as one might reasonably expect for the realistic case of finite radial radiation transport.

The water flow to the calorimeter was measured with a calibrated critical orifice, pressure drop being recorded on a standard mercury manometer. The temperature rise in each (separate) segment was measured with copper-constantan thermocouples and the outputs were monitored on an Electro-Instruments, Inc., Model 630 integrating digital voltmeter.

Since the seven separate annular segments (including, as a degenerate case, the small circular segment at the center) were connected to the water flow in a series fashion, it was important to insure that the total rise in water temperature remain sufficiently small as to avoid boiling. This places a lower limit on the water flow. On the other hand, sensitivity and accuracy in temperature measurements require reasonably large temperature differences per segment. These accuracy requirements place an upper limit on the water flow. For this reason a number of readings were obtained over a range of water flow rates, as indicated in Table I.

The power captured by the total beam calorimeter was then compared with the input electrical power minus the losses to the cathode, buffer, anode and magnet housings. The calorimeter was moved to a number of different axial positions. A distinct increase in total beam power was detected as the calorimeter was moved closer to the exit plane of the arc jet. The results of this experiment are shown in Table I and Fig. 22.

A distribution of the power to each segment is shown for point number 6 (of Table I) in Fig. 21. Since the area of each segment can easily be determined, it is possible to determine the local energy flux (watts/ cm^2) incident upon each segment. The data (as well as that from a sodium test) are presented in Fig. 23. This calculation assumes not only axial symmetry, but coaxial alignment of the arc plasma and the total beam calorimeter. While neither of these assumptions are completely true, the symmetry and alignment were, at least visually, reasonably good.

It is of interest to note two special points in conjunction with Fig. 23. The first is the relatively good agreement with the results of the local energy flux probe (see Fig. 19) for the lithium experiments. The second point concerns the rather pronounced sharpness of the peak of the radial distribution of the energy flux in the sodium experiments relative to the lithium experiments. The explanation for this effect is not apparent. The magnetic field in both tests was almost identical (in the lithium tests discussed the magnet current was 250 amps, the magnet current in the sodium tests was 240 amps) and the arc design was similar. Furthermore, the background tank pressures were also similar (i.e., in the range 5×10^{-5} to 10^{-4} torr) during these runs. Finally, the arc power was actually <u>greater</u> in the lithium test (17.5 kW as opposed to 11.4 kW for the sodium test) although the peak energy flux is smaller than that for the sodium test. It is interesting to observe however that the total integration of the energy flux distributions over the area of the calorimeter does yield a greater result (5.95 kW versus 4.97 kW, at the same position) for the lithium test than for the sodium test; a fact which is not readily apparent in Fig. 22 due to the greater relative weighting of the larger segments.

The most significant aspect of the total beam calorimeter experiments appears to be the direct, <u>in situ</u>, measurement of total beam power for two different propellants at two different sets of ALPHA operating
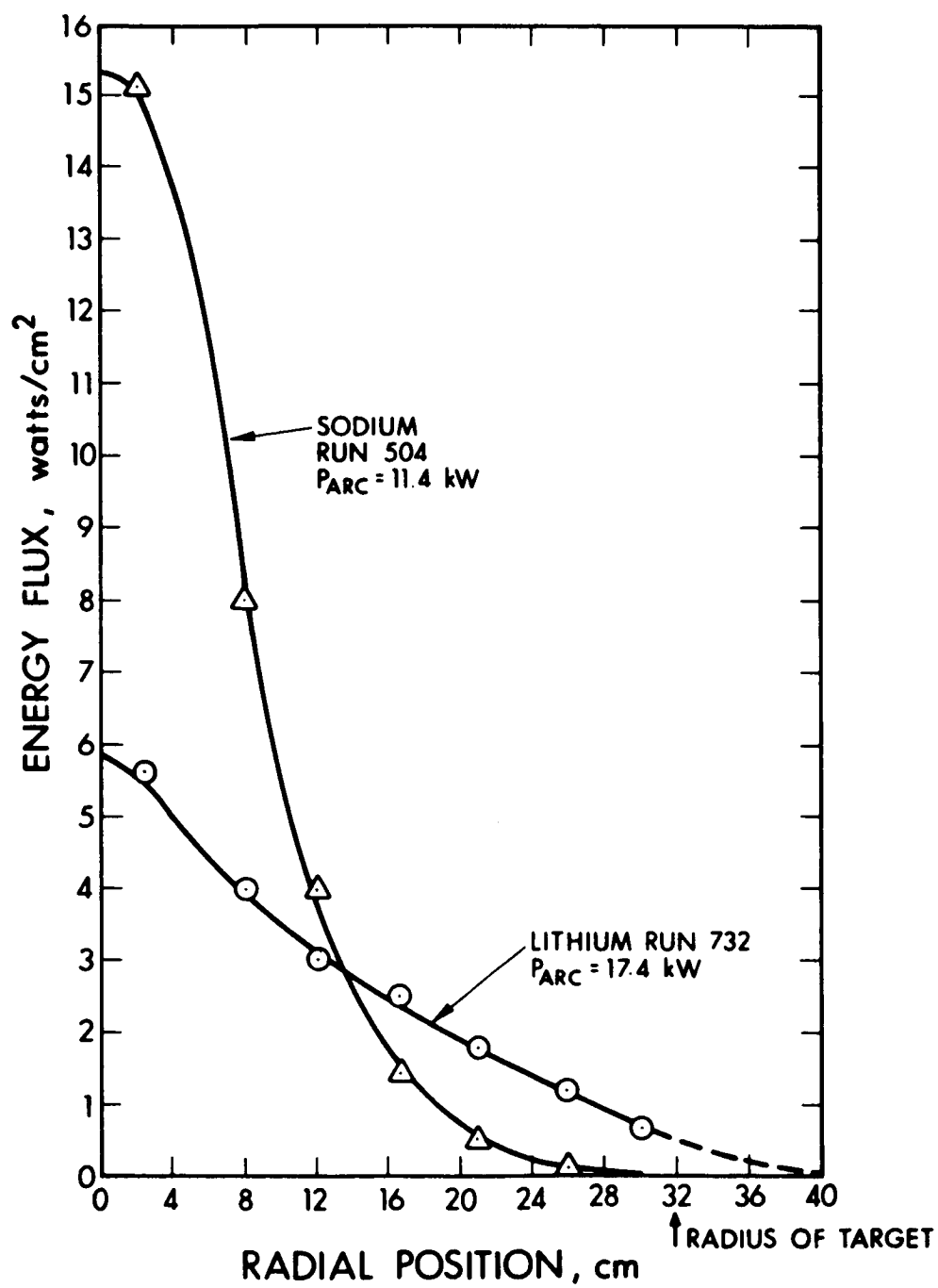
Figure 23.   Total Beam Calorimeter Energy Flux
             Distribution

73626592

conditions and the reasonably close agreement with both the radial distribution of energy flux (as measured with the local energy flux probe) and the net beam power (as determined from input arc power minus coolant losses). These results may be interpreted as an independent check upon the essential validity of the measurements of the thermal efficiency of the ALPHA thrustor.

4.3 SPECTROSCOPIC MEASUREMENTS

4.3.1 INTRODUCTION

The plasma exhaust of an alkali plasma Hall accelerator exhibits sharp radial variations in intensity, as may be seen in the spectrogram of Fig. 24, and in the photograph of the ALPHA plasma (Fig. 25). Roughly, the jet is composed of three major radial regions; a bright central "cathode jet" region surrounded by a "discharge" region (bounded on the outside by an "anode jet"), and a "plume" region. Roughly described, the central jet is almost completely ionized (appearing as the greenish-yellow region in Fig. 25), the discharge region contains atomic and molecular species, and ions in their ground state (reddish-colored region in Fig. 25). The plume is composed of atomic and molecular species (a faint pink-blue barely visible in Fig. 25).

Velocity measurements during this program have been limited primarily to the cathode jet region. The Doppler shifts of interest range from 0.5Å to 1.0Å, with a desired resolution of about 0.1Å. Measurements of the Doppler-shift of atomic spectral lines are, with only a few exceptions, obscured by the Stark-broadened lines themselves. Therefore, the Doppler-shift measurements were limited to the narrow ion spectral lines, which occur almost exclusively in the cathode jet.
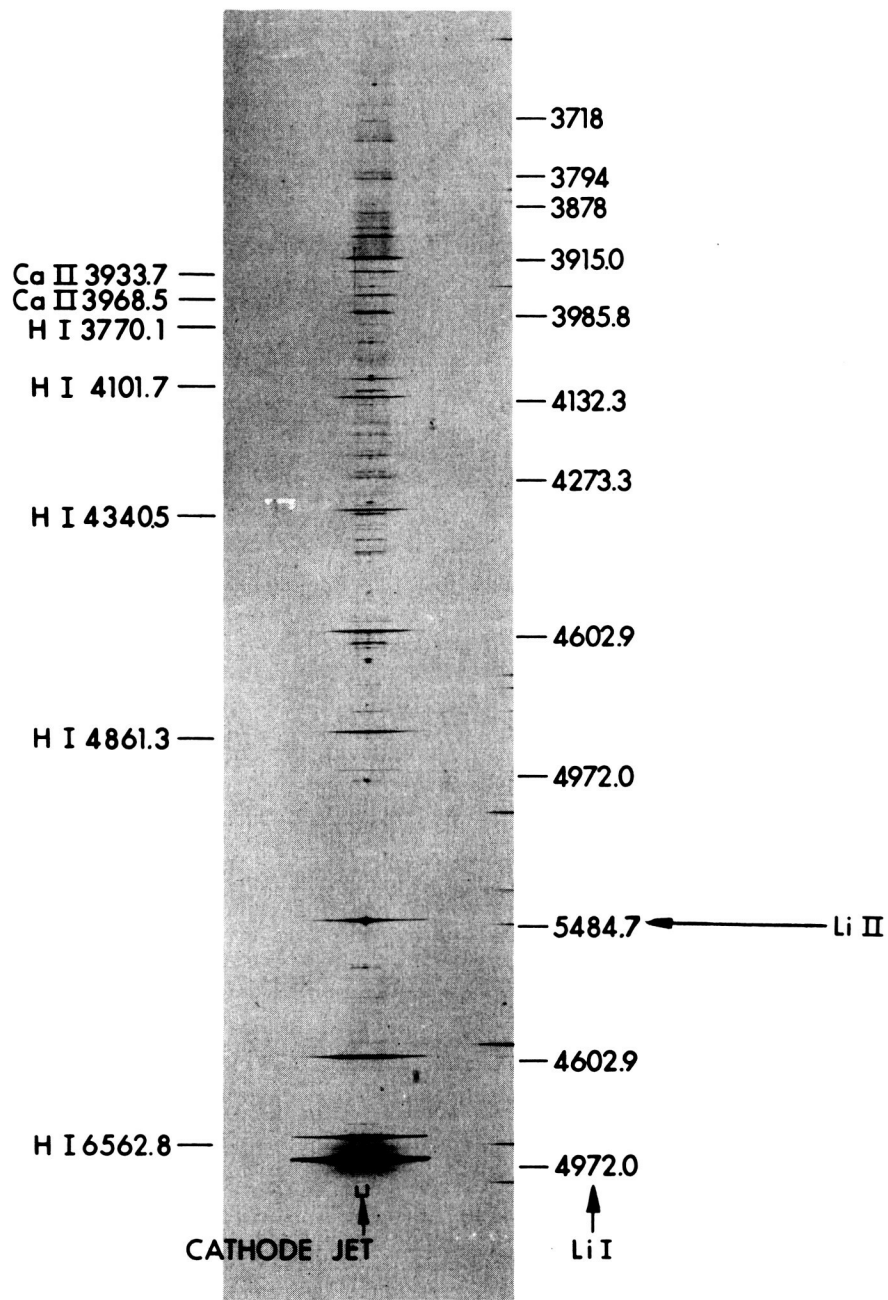
Figure 24.   Photo of Lithium Spectrum from ALPHA
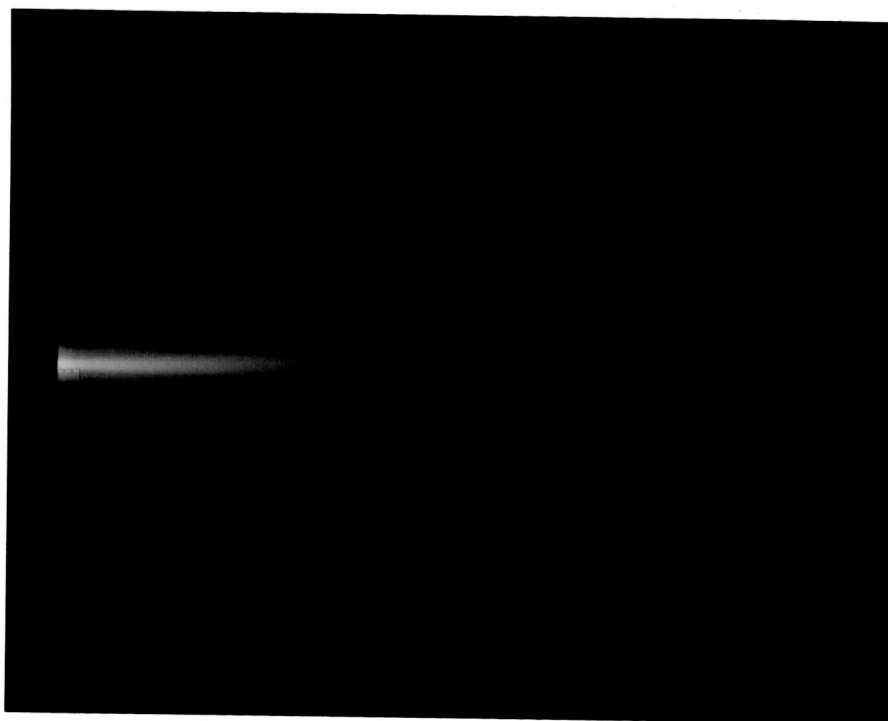
Figure 25.   Photograph of Plasma Exhaust from ALPHA

The lithium ion has a number of narrow spectral lines in the 4000-5500Å range (Ref. 16). The most intense ion line (at 5483-5485Å), however, has a complex fine structure, the components of which have been identified by Herzberg and Moore (Ref. 17) and earlier by Schuler (Refs. 18 and 19).

Spectral lines corresponding to transitions between the excited states of ionized lithium (i.e., lithium II) have definitely been observed in the central portion of the cathode jet when the ALPHA device is operating on 10 milligram/sec of lithium and about 1 milligram/sec of hydrogen. These lines are <u>not</u> observed when argon or nitrogen are used instead of hydrogen. Observation of lithium II excited-state lines indicate relatively high electron temperatures in the cathode jet since the first excited level is 61.95 electron-volts above the ground state of the lithium ion.

4.3.2 APPARATUS

Three spectroscopic instruments are used for species identification and for Doppler velocity measurement. A Gaertner L231 high dispersion spectrometer is used to identify species and visually monitor arc operation. A Bausch and Lomb 1.8 meter large quartz spectograph provides spatially-resolved spectrograms in the 2000 to 6000Å region. This instrument is extremely useful for determining the rotational velocity in the 2000-2300Å region, where it has a resolution capability of about 0.01Å. A Jarrell-Ash 1.0 meter vacuum scanning monochromator provides high spectral resolution in 4000 to 7000Å range for Doppler velocity measurements of the lithium ion spectrum.

The optical system and spectrometer for this measurement are located approximately 3 meters downstream of the accelerator, at an angle of 8 to 10° from the axis of the plasma jet. An image of the plasma jet

0.1 to 0.4 meter downstream is focused on the spectrometer entrance slit by a 36 inch focal length f/9 telephoto lens, so that the optics of the f/9 spectrometer are fully illuminated to give high spectral resolution.

Spatial resolution along the axial direction of the accelerator is limited by the 3-5 micron slit itself. Radial spatial resolution is provided by a 1/16 inch mask directly in front of the slit.

A standard 4 inch vacuum gate valve has been used to provide a "vacuum lock" spectroscopic window. The window may be mounted on any of three positions on the side of the tank. This allows spectroscopic observation over an axial range of about 30 cm. The quartz window can thus be removed and cleaned of deposited lithium without disturbing the vacuum or the continuity of a test.

The sliding valve window assembly permits one to clean the vacuum chamber window before each spectral scan. Under typical lithium feed conditions, the window transmission e-folding time constant, at the downstream end of the tank, is 8 seconds. Only small line shape corrections are necessary since the entire 5483-5485Å Li II line is scanned in about 10 seconds, and the major peaks are scanned in about one second.

Finally, of considerable importance, a lithium spectral calibration lamp was also constructed. This source was operated in a glow discharge mode, producing the 5483-5485Å lithium ion lines. The parametric (viz. pressure, discharge voltage, discharge current, and mass of lithium in the hollow cathode) control was relatively sensitive. The discharge source is best operated with the following parameters:

$$P = 0.7 - 1.0 \text{ Torr}$$
$$I = 0.3 - 0.7 \text{ Amperes}$$
$$V = 225 - 350 \text{ Volts}$$

within the stated limits, if the lithium ion lines are to be observed.

The ability to produce a spectral standard for the specific scanning monochromator (with its own inherent grating and drive characteristics) under laboratory conditions identical to those found during the axial Doppler measurements themselves was found to significantly improve the accuracy of the axial velocity measurements.

4.3.3 DOPPLER AXIAL VELOCITY

Axial velocities of excited lithium ions in a lithium-hydrogen alkali plasma Hall accelerator were recorded as 3×10^4 meters per second ($\pm 2 \times 10^4$ meters/sec) during preliminary measurements. The lithium 5483 to 5485Å was sufficiently resolved into its three main components, as seen in the reproduction of the recorded trace depicted in Fig. 26. The engine was operated at 18.6 killowatts input and an I_{sp} of about 5000 seconds (exhaust velocity of 5×10^4 meters per second).

The absolute wavelength of the observed Li II 5484Å [*] lines was determined by comparison with the Hg I 5460.742Å [**] line (both observed in the second order), and using the instrument scanning rate as determined by the relative position of the Hg I 3650.144, 3654.833, and 3663.274Å lines. Due to imperfections in the spectrometer diffraction grating, the third order spectral lines should not be used as wavelength reference lines for other spectral orders. This method of determining wavelengths has been known to cause errors up to several tenths of an angstrom (Ref. 21).

---

[*] Lithium wavelengths taken from Herzberg and Moore (Ref. 17)

[**] Mercury wavelengths taken from C. E. Moore (Ref. 20)
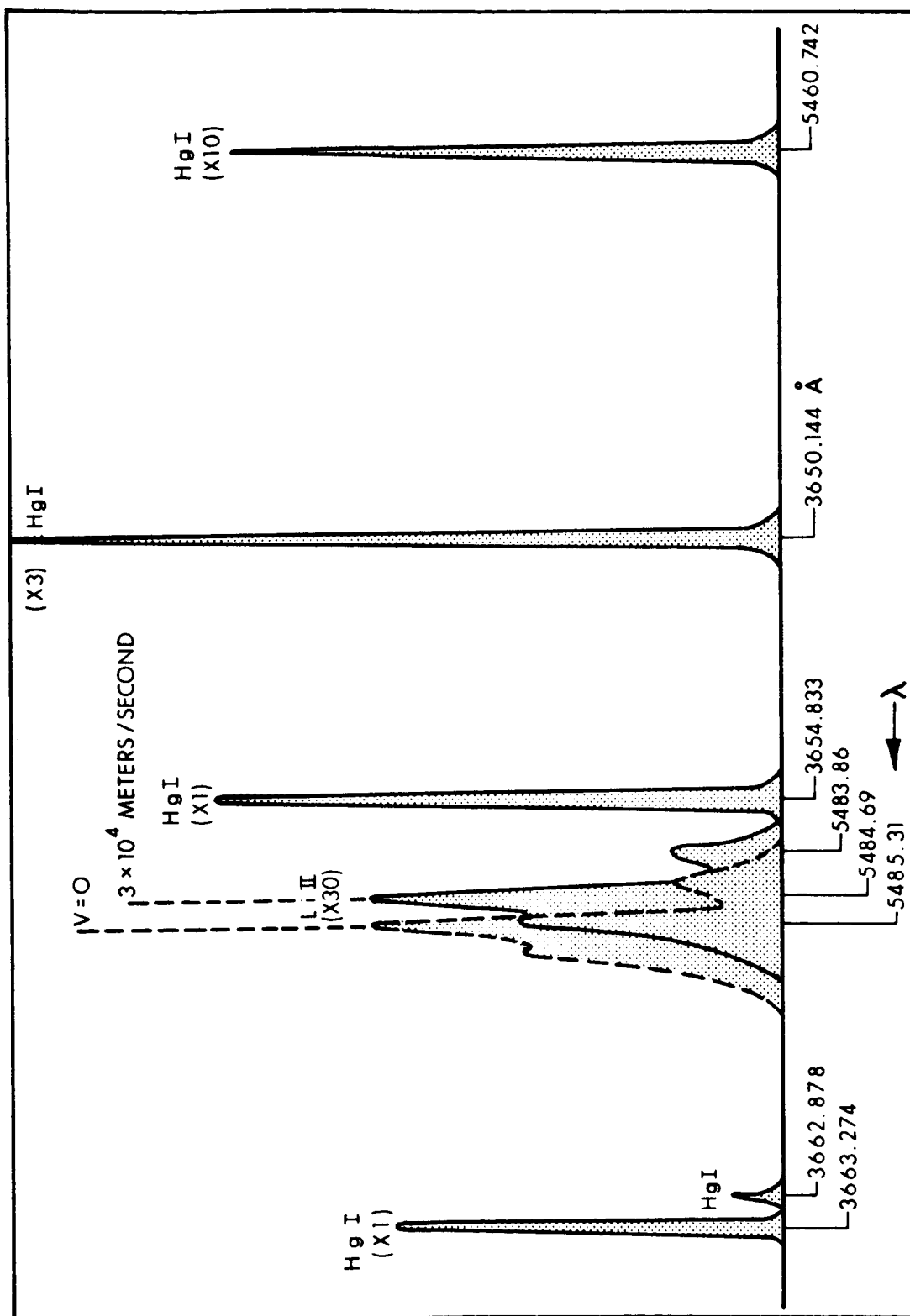
Figure 26. Reference Spectra for Doppler-Shifted Lithium Ion Lines

The major errors in the present measurement result from a variation in the scanning rate of the Jarrell-Ash monochromator. The scan rate determined from the Hg I 3650, 3654, and 3663Å lines was found to possess a repeatable 0.5 percent variation, which would produce a 50 percent variation in the value of the plasma velocity.

Most of the existing calibration errors were removed by direct comparison of the Doppler-shifted lines with unshifted reference lines from a stationary lamp. A lithium hollow-cathode discharge lamp was constructed to provide a source of Li II 5484Å radiation for this calibration.

The operation of the lithium discharge calibration source was quite successful. This source greatly increased the accuracy of the Doppler axial velocity measurements (viz., reduced the error band from 2×10^4 meters/sec to about $\pm 4 \times 10^3$ m/sec, or almost an order of magnitude increase in precision). This important increase in accuracy is the result of direct comparison, in situ, of the shifted[*] and unshifted lithium 5483 - 5485Å ion lines. In this way errors stemming from:

    a. Discrepancies in the published values of the unshifted wavelengths of the various ion lines,

    b. Diffraction grating ruling errors,

    c. Errors due to nonlinear scanning speeds on the Jarrell-Ash 1.0-meter scanning monochromator

    d. Errors stemming from a nonuniform dispersion at different wavelengths, and

    e. Readout errors

were either greatly reduced or cancelled out. The major problem before the operation of the calibration source was essentially one of determining the small difference between two large numbers. One of these

---

[*]Note that the spectrograph views the moving plasma essentially "head-on", so that observed spectra are shifted toward the blue (i.e., lower wavelengths).

numbers (i.e., the "unshifted" wavelength) is determined from standard values (see Fig. 27a) which need only be in error by 1 part in 10^4 to cause serious errors in the Doppler axial velocity measurement, and the other of these numbers (i.e., the Doppler-shifted wavelength) is determined from a scanning monochromator subject to all the errors listed above.

Figure 27b shows a trace of the 5483 - 5485Å lithium ion lines. Qualitatively, the agreement with Schulter's and Herzeberg and Moore's (Ref. 17) results is unmistakable. All of the various lines are observed with shape and relative wavelength spacing in good agreement. However, there was observed to be a definite **quantitative** <u>difference</u> in the numerical values of the wavelenghts associated with the various line peaks. This difference (i.e., 0.21Å) alone would result, cet. par., in a velocity uncertainty of about 1.2×10^4 m/sec. Figure 27c shows the Doppler-shifted spectra from ALPHA. Figure 27d shows the Doppler-shifted spectra from the ALPHA device which has been superimposed upon the unshifted reference spectra from the calibration source, taken <u>in situ</u>, on the same instruments (accomplished by scanning the signal from ALPHA and then inserting a mirror in the optical path and scanning the signal from the calibration source). This technique:

a. Automatically calibrates the "standard value" of the unshifted lithium ion lines for the particular scanning monochromator being used,

b. Cancels out any effects due to imperfections in the diffraction grating (i.e., the same diffraction grating is used for both traces),

c. Cancels out any errors due to nonuniform scanning speeds (i.e., the same portion of the drive mechanism is used for both traces — and both sets of measurements were repeated many (> 10) times,

d. Cancels out errors due to a nonuniform instrument dispersion (i.e., both measurements were made on the same instrument operating in the same wavelength region), and

Figure 27a. Spectrum of Lithium Ions (from Schuler, also Herzberg and Moore)

Figure 27b. Spectrum of Lithium Ions from Calibration Source

HgI 3654.833 Å (REFERENCE LINE)

Figure 27c. Doppler-Shifted Spectrum of Lithium Ions

Figure 27d. Superimposed Doppler-Shifted and Unshifted Lithium Ion Spectra
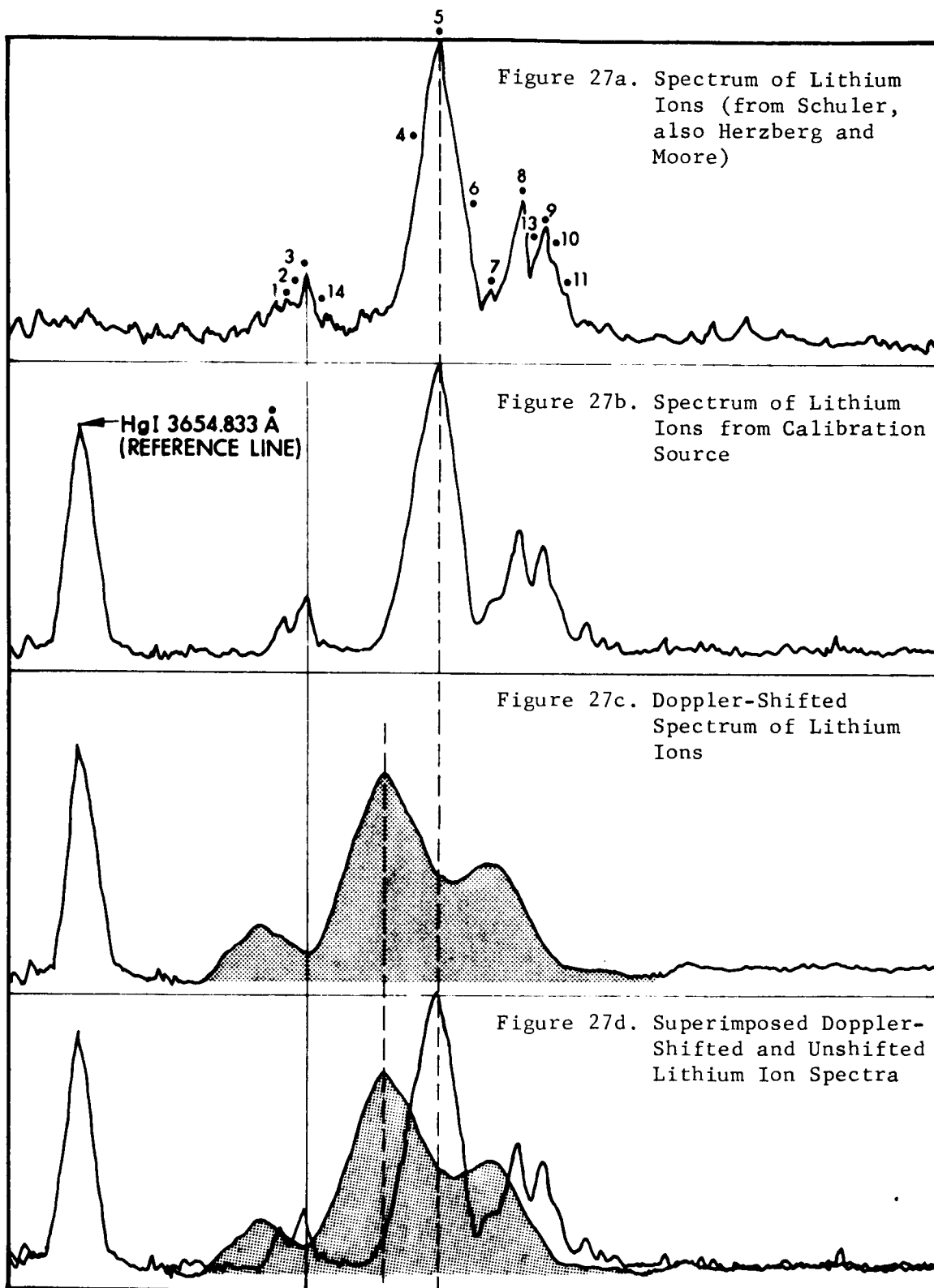
e. Of course, has no effect on readout error. This then is the
      only real source of error associated with the new technique
      involving combined use of a stationary calibrating plasma,
      and the moving plasma exhaust beam.

The Doppler velocity shift is calculated from the relation $\Delta v = (\Delta\lambda/\lambda)$ C, where $\Delta\lambda$ is the Doppler wavelength shift of the spectral line of wavelength λ, Δv is the velocity of the species relative to the observer, and C is the velocity of light.

To illustrate how this experimental technique has now moved "out of the mud", we observe that the experimentally determined value of Doppler axial velocity of 2.1×10^4 m/sec (Run No. 726), corresponds to a wavelength shift.

$$\Delta\lambda = \lambda(\frac{V}{C})$$

$$= 5484.6 \left(\frac{2.1 \times 10^4}{3 \times 10^3}\right)\text{Å}$$

$$= 0.384\text{Å}.$$

Since the dispersion of the 1.0-meter Jarrell-Ash at the most appropriate[*] drive speed corresponds to about 3.15Å/inch, the Doppler shift results in a displacement which is typically about 1/8 inch. While this is not very large, it is certainly sufficient to obtain accuracies of ±20 percent. This corresponds to about ±0.025 inch readout error, and is roughly comparable to the width of the pen trace on the recording paper.

It should also be mentioned that due to the presence of radial velocity distributions there is also an additional source of error which is not associated with the limitations of the technique. The very concept of

---

[*] Allowing for the effect of window-coating by lithium deposition.

" a Doppler shift" implies the existence of a single, unique, ion velocity. For this reason it is not surprising that the results of the Doppler axial velocity measurements are somewhat sensitive to the (unknown) radial velocity distribution as well as the position and line of sight of the region being studied.

In summary, the accuracy of the Doppler axial velocity measurements has been greatly improved through the use of the calibration source.

The velocity measurements now indicate lithium ion velocities near the exit of the ALPHA device, of about $(2.1 \pm 0.4) \times 10^4$ m/sec.[*] These measurements are in good agreement with phototracer results at the same general location (see Subsection 4.4). Unfortunately, the intensity of the ion line(s) drops off so sharply with axial position from the anode face that it has not been possible to use this technique further downstream where phototracer measurements (as well as thrust and mass flow rate measurements) indicate increased velocities.

4.3.4 DOPPLER ROTATION

Doppler rotation velocities up to 4000 meters per second were recorded early in the program at 1.9 mm radius in the cathode jet of a lithium-nitrogen bipropellant accelerator. The angular velocity appeared to be constant at smaller radii for all ionic species observed, which included Ar^+, Ca^+, Mg^+, N^+, and C^+ (see Fig. 28). No lithium ion lines were observed during these tests.

High resolution plates were used later in the program to attempt to determine the spatial variation of rotational velocity for the more recent engine configurations. Using quartz optics, (side view) image of the plasma at several axial positions were focused successively on

---

[*] For the conditions of Run 726, in which P_{arc} = 18.6 kW and I_{sp} = 5000 sec. with $p_{tank} \approx 10^{-4}$ torr.

C II – DOPPLER-SHIFTED CARBON ION LINES
B I – BORON ATOM LINES
Si II – SILICON ION LINES
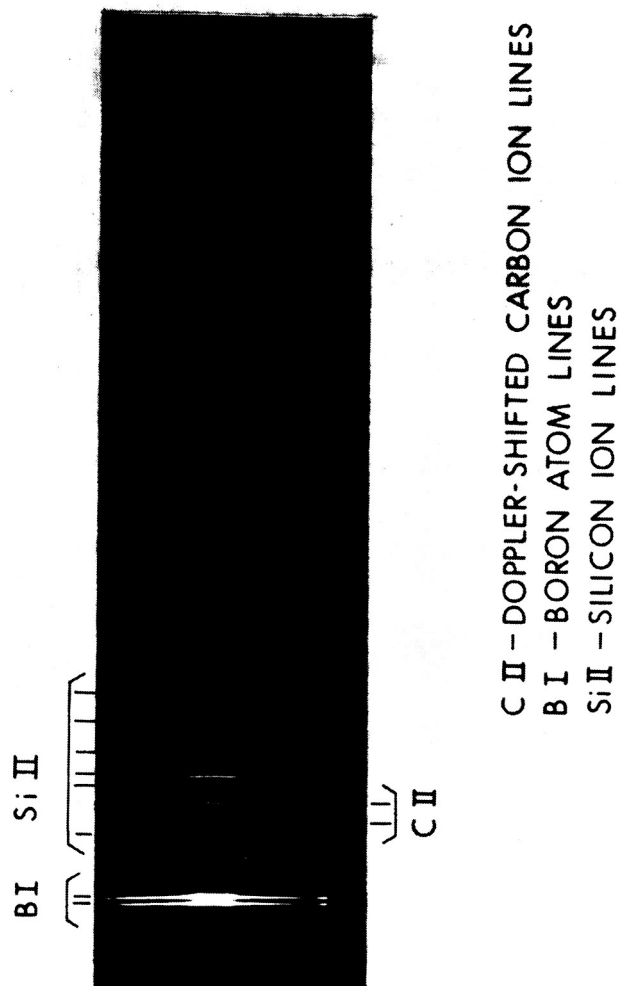
Figure 28. Near Ultraviolet Spectrum Showing Rotational
Doppler Shift of Carbon Ion Lines

TABLE II

WAVELENGTH IDENTIFICATION FOR Li II ION SPECTRUM
SHOWN IN FIGS. 27a, b, c, and d

Isotope	Component Number	Wavelength ($\overset{\circ}{A}$)
Li^7	(1)	5483.345
	(2)	5483.459
	(3)	5483.655
	(4)	5484.424
	(5)	5484.485
	(6)	5484.595
		5484.697
	(8)	5484.973
	(13)	5485.134
	(9)	5485.176
	(10)	5485.280
Li^6	(14a)	5483.879
	(14b)	5483.920
	(7)	5484.823
	(11)	5485.463

the entrance slit of the Bausch and Lomb spectrograph. Spectrograms in the 2000-2400Å range recorded the Doppler wavelength shift at high spectral resolution.

Unfortunately, the results of these experiments were not conclusive. When the ALPHA thrustor was operated in its more recent fashion (i.e., lithium as primary propellant with a small bleed of hydrogen as a secondary propellant, for buffering purposes) even the higher resolution Doppler rotation measurements were not successful at obtaining clear evidence of plasma rotation. It is probable that, in a sense, the ALPHA device was obscuring the effect itself. In the new mode of operation, cathode, buffer and insulator erosion were markedly reduced. This, of course, eliminated the source of much of the impurity spectra noted in the earlier experiments. Further, in the cathode jet region (where the intensities are highest) the hydrogen is virtually fully ionized and therefore emits only continuum radiation rather than line spectra. This is substantially different from the nitrogen of the earlier tests, which can be multiply ionized and will still exhibit bound-bound transitions resulting in spectral lines which are useful for Doppler rotational velocity measurements. Finally the lithium itself is also essentially fully ionized in this region.

While the Doppler axial velocity measurements could utilize the spectra resulting from transitions among the excited states of the lithium ion, this presents serious problems in the Doppler rotational velocity technique. As mentioned earlier, the "5485Å lithium ion line" is really a multiplier of fourteen closely spaced lines. Since the Doppler rotational velocity technique is based upon the fact that one plasma region will be proceeding toward the observer while another is receding, the spectral line will be "tilted." This follows from the fact that the portion of the plasma above the center of rotation will, for example, be receding and thereby undergo a wavelength shift toward the red while

the plasma below the centerline will be shifted in the opposite sense (i.e., toward the blue). This has the net effect of "tilting" the line, as shown in Fig. 28. Unfortunately, the lithium "line" is already sufficiently broadened as to obscure the entire effect.

A possible solution to this problem might well be _intentional_ addition of trace amounts of impurities for the express purpose of obtaining spectral lines more suitable for Doppler rotation measurements. However, due to limitations of the present program, this was not done.

4.4 PHOTOTRACER MEASUREMENTS

4.4.1 INTRODUCTION

Detailed measurements of the axial velocity in the exhaust of the Hall current accelerator have been obtained using a simple phototracer system. This device consists of two photomultiplier tubes and optical focusing lenses which can be located in various positions such that the photomultiplier tubes "see" two well defined (viz., about 1 cm radius) regions separated by a known axial distance. Typically, the axial separation ranged from 0 to 10 cm, with 8 cm apparently representing the best compromise between signature retention and accurate determination of local velocities on the one hand, and accurate determination of the relatively small time delay associated with the typical exhaust velocities on the other.

4.4.2 CALIBRATION OF OPTICAL SYSTEM

Once the phototracer system (see Fig. 29) had been fabricated, it was necessary to calibrate the field of "vision" of the system as well as its temporal response. In order to determine the field of "vision" of the photomultiplier optics a simple bench-top experiment was carried out.
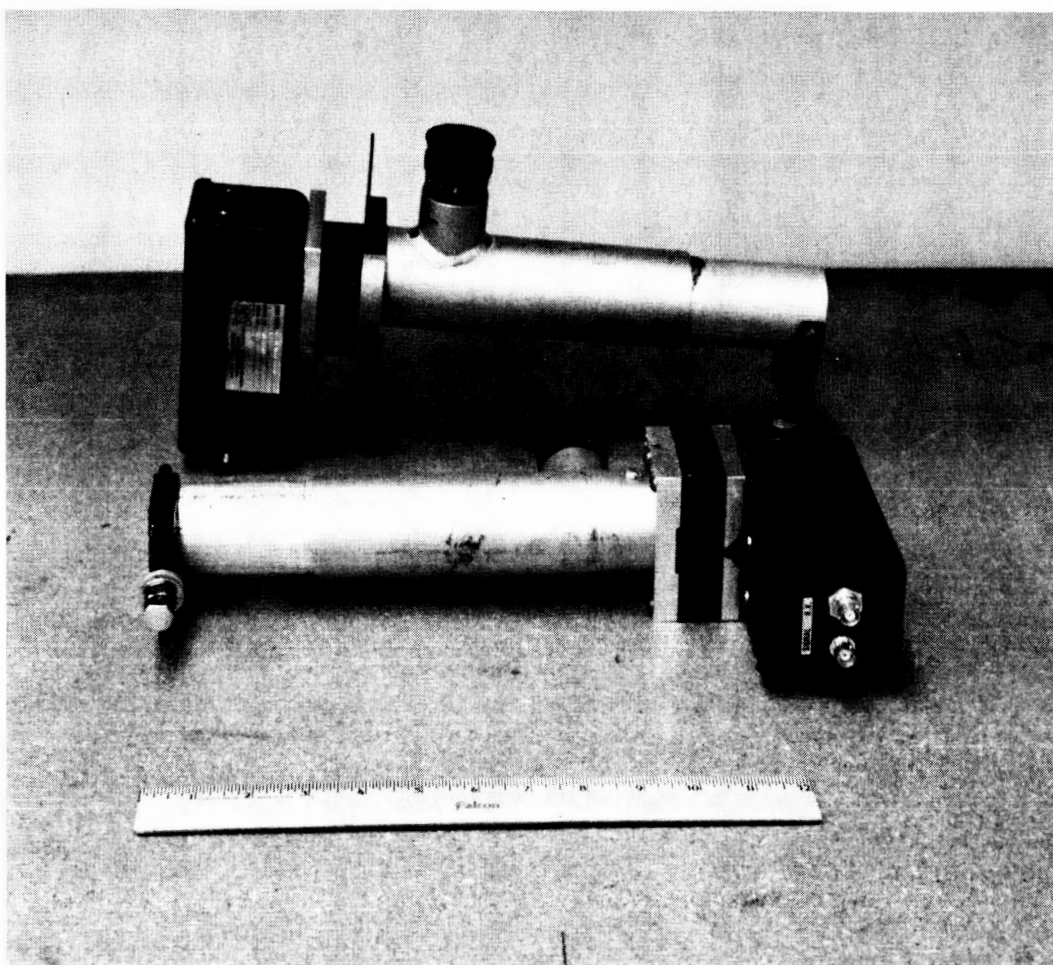
Figure 29. Photograph of Dual Phototracer System

The phototracer units were mounted such that the centers of their field of vision were 10.5 cm apart, and such that their focal plane was located 118 (±2) cm. The later quantity was determined by sighting through the optical system and observing when a printed page was in sharp focus. It was noted that the focal length was quite well defined, since print, easily read at 118 cm, was barely discernible beyond 120 cm or within 116 cm.

A meter stick was then placed in the focal plane. In a dark room a point source of light (simple flashlight covered by black tape with a tiny pinhole in the center) was moved along the meter stick. The response of the dual photomultiplier system was then determined as a function of the position of the light source along the meter stick (corresponding to axial position in the ALPHA experiments). This was done by plotting the output of each photomultiplier tube, as recorded on a Tektronix type 555A dual beam oscilloscope, versus the location of the light source.

The data resulting from this calibration definitely indicated that the phototracers would "see" only a relatively small axial sample of the plasma beam. Two distinct spikes were observed whose peaks were located 10.5 cm apart. The "half-width" of these peaks (i.e., the width, in cm, of the amplitude versus position at a point where the amplitude was half the maximum amplitude) varied between 1.0 and 1.3 cm for the two photomultipliers. Furthermore, due to the steepness of the signal attenuation as the light source moves away from the peak, there is a strong weighting of points near the peak (viz., along the optical line of sight).

However, while the transverse focusing is quite sharp, the focusing along the line of sight is not as definitive. That is, there exists a considerable response to light sources along the line of sight, but

not directly in the focal plane. In effect the "field of view" of the photomultipliers would correspond, roughly of course, to a pencil about 4 to 6 cm long, 1 cm in diameter, and having both ends sharpened.

4.4.3 BENCH-TOP CALIBRATION OF "PHOTOTRACER SYSTEM"

Step I

Using two Pacific Photometric Instruments Model 50 photomultipliers, a General Radio Corporation stroboscope, a Tektronix Type 555 dual beam oscilloscope with a Hewlett-Packard Model 196-A oscilloscope camera and a Hewlett-Packard high voltage power supply, a specific (and also variable) stroboscopic frequency was selected. At a distance of 1.18 meters both photomultipliers were placed viewing the stroboscope.

With 580 volts on each photomultiplier, the camera on "bulb" and f = 5.6, the stroboscope set at nominally 300 Hz, the oscilloscope sweep rate at 1 millisecond/cm the following trace was obtained (see Fig. 30a). The agreement between the stroboscopic period of 3.33 millisecond/ pulse, and the phototracer system response is evident.

Step II

Since the results of Step I clearly indicate the accurate definition of the photomultipliers, it was decided to check the accuracy of the triggering circuit. To do this, it is necessary to simulate the actual laboratory tracer studies with an "artificial" time delay corresponding to a typical velocity determination.

This was accomplished as follows. A light source (ordinary flashlight with a pinhole in a black cover) was directed onto a rotating hexagonal mirror system. The light reflected from the mirror was directed

OUTPUT FROM
PHOTOCELL A

OUTPUT FROM
PHOTOCELL B
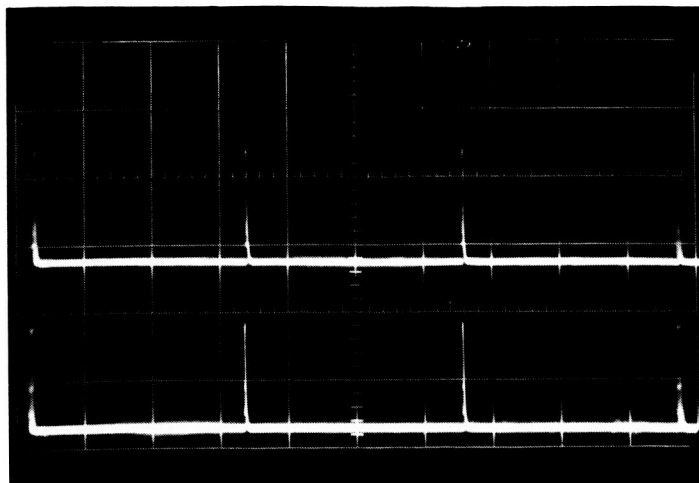
ZERO ROTATION

STROBOSCOPE
OPERATING AT
300 Hz

1 MILLISEC/cm

OUTPUT FROM
PHOTOCELL A

OUTPUT FROM
PHOTOCELL B
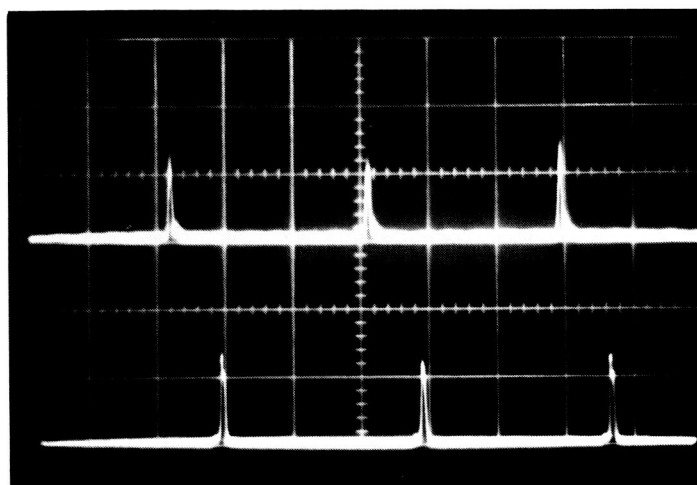
CLOCKWISE MIRROR
ROTATION

OSCILLOSCOPE
SWEEP AT
20 MILLISEC/cm

$\theta = 17.3°$
$\tau = 57$ MSEC
$\delta_t = 16$ MSEC

OUTPUT FROM
PHOTOCELL A

OUTPUT FROM
PHOTOCELL B
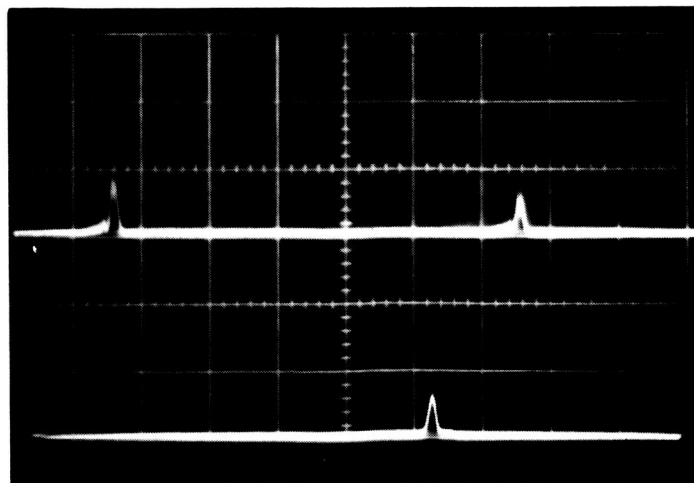
COUNTERCLOCKWISE
MIRROR ROTATION

OSCILLOSCOPE
SWEEP AT
10 MILLISEC/cm

$\theta = 17.3°$
$\tau = 57$ MSEC
$\delta_t = 16$ MSEC

Figure 30. Phototracer Calibration Photos

P0308

to the two photocells — which were displaced a known angle from one another — and the photomultiplier outputs were recorded photographi- cally on the oscilloscope.

The results, for both clockwise and counterclockwise rotation of the mirror system, are shown in Figs. 30b and 30c, respectively. The spacing between the "blips" recorded by an individual photocell is determined solely by the rotational frequency of the rotating mirror system. Taking into account the angular velocity of the drive motor, the diameter of the drive shaft, the diameter of the mirror step-down and the fact that there were 6 mirrors, leads to a theoretical separa- tion period of 57 milliseconds between "blips." This compares reason- ably well with the experimental results shown in Figs. 30b and 30c.

Finally, the phase <u>shift</u> between the consecutive outputs of both photo- tracer units depends upon: (a) the sense of rotation, (b) the rotation rate of the mirrors, and (c) the angular separation of the mirrors. Both clockwise and counterclockwise rotations were used and the sense of the phase shift (i.e., whether one of the phototracer units "led" or "lagged" the other) was always correct. The rotation rate and angular separation were also varied over about a factor of two each, and the results were always in reasonably good agreement with the predicted values. For Figs. 30b and 30c the angular separation was 17.3° and the theoretical phase shift was 16.4 milliseconds. The agreement was generally quite good (i.e., within 10%).

4.4.4 PHOTOTRACER EXPERIMENTAL PROCEDURE

Basically the two photocells are focused on the moving plasma. By determining the time of flight of inherent fluctuations past the two photocell beams it is possible to determine the velocity of these fluctuations (see Refs. 22 and 23). Since it is believed that most

of the observed fluctuations in light intensity are correlated to fluctuations in local electron particle density, this implies that one is really measuring the velocity of small pockets of either increased or reduced (relative to the long time average at a given point in the flow field) electron particle density. Provided that such a velocity may reasonably be identified with the "stream velocity," the latter quantity may be deduced.

The photomultipliers used were RCA-IP28 with an S-5 response. The voltage on each photomultiplier was between 700 and 850 volts (chosen for convenient scale amplitude). The photomultipliers were placed 8.0 ±1/2 cm apart and were optically focused with lenses. The photomultipliers were focused at a point 118 cm from the entrance lens, and were either parallel or pointed at the same spot. The outputs were calibrated with a stroboscope set at 300 Hz and were accurate to within photograph readout error (< 5 percent). The photomultipliers were used in conjunction with the following filters:

a. Band pass allowing 6707Å lithium I line

b. Band pass allowing 5384Å lithium II line

c. Band pass allowing 6562Å H line

d. No filter at all

The experimental procedure was as follows:

a. Record the point number, run conditions, date, time of day and oscilloscope settings.

b. At an arbitrary instant, open the camera shutter (with the scope camera mount closed, and the graticule and trace intensities, exposure time and F setting properly adjusted for clear photographic observation).

c. While the shutter is open, press the single sweep trigger. Provided the time delay is zero, both the upper and lower traces will fire simultaneously - thus recording, at the speed determined by the settings on the oscilloscope, events for some time increment, τ, as viewed by photocells 1 and 2.

d. <u>Trigger calibration</u> was performed by connecting the same photocell to both the upper and lower beam channels and performing the above procedure. Calibrations were performed with scale settings of 10, 5 and 2 μsec on the 10 cm oscilloscope screen. The errors (i.e., "shifts" existing in signals from the same photocell) were:

10 μsec/cm scale - 1 μsec

5 μsec/cm scale - 0.5 μsec

2 μsec/cm scale - 0.2 μsec

Corresponding to a photographic readout error of approximately 0.1 cm.

e. <u>Noise level calibration</u> - The background, photomultiplier tube, transmission line and oscilloscope noise level was calibrated, in situ, by placing a cardboard sheet in front of one photocell, but not in front of the other, while both "viewed" the plasma. Settings on both photocell circuits were identical. The amplitude and wave form of the signals were compared with, and without, the cardboard inserted to block one photocell. Without the cardboard the signals were similar in both general shape and peak and valley magnitudes. With the cardboard blocking one photocell, the magnitude dropped to about 1/5 that of the unobstructed photocell, and the signal had a random-noise pattern with no observable correlation to the signal from the unobstructed photocell.

f. Choice of settings was dictated by the somewhat conflicting limitations of:

(1) Adequate signal amplitude

(2) Keeping signal on scale

(3) Photomultiplier tube voltage limitations

(4) Sufficiently high speed for accurate time delay measurement

(5) Sufficiently slow speed to allow definition of a <u>number</u> of "signatures" on the same photograph

(6) Limitations of the photocells

(7) Limitations of the oscilloscope

(8) The range of velocities which actually exist within the plasma

(9) The range of separation possible between photocells

(10) The intensity of the beam at the position of the only truly appropriate tank window.

The "best-compromise" settings were found to be:

(1) 1 mV/cm ⎱
⎰ Type D plug-in amplifier
(2) 1 mV/cm multiplier

(3) 800 volts on photomultiplier tubes

(4) 2 μsec/cm sweep rate*

(5) Parallel beams 8 cm apart (except where noted)

(6) Zero trigger delay

(7) Single sweep traces

(8) Grid intensity relatively weak

(9) Slightly different intensities of upper and lower traces for easy identification in case signals cross one another

(10) $F = 1.4$, exposure ⁻ open (8)

(11) Photocell positions at 114 and 122 cm from anode face

g. <u>Identification of Signatures</u> - Over 60 photographs of the single-sweep output of the two photocells were taken during Runs 720, 721 and 722. Numerous complex signatures (i.e., peculiarly shaped peaks, valleys, double peaks, double valleys, inflections, flat regions with sudden rises or drops, etc.) could be identified after careful study (see Figs. 31 and 32).

Each "signature"; that is, characteristic form in the amplitude versus time display from the photomultiplier, which correlated - within reasonable limits - with a similar signature on the trace from the other photocell, was carefully recorded along with the time shift between the two. Since the phototube views a volume of plasma which has nonuniform properties as well as, most likely, a velocity profile, all the shifts (and in fact, not even all the signatures) are the same on a given photograph. Thus, the various signature identifications, and their corresponding time delays, are plotted in a distribution form. That is, the number

---

*Due to difficulties with the sweep rates of the upper and lower beams, a very small (nearly zero) delay was used to align the calibration signals more closely. For part of the tests this delay was 0.1 μsec. Later this was reduced to zero when it was observed that the waveforms on the calibration shots were virtually aligned. Also, due to nonuniform sweep rates and/or nonidentical sweep rates between the upper and lower beams, the sweep rate for the lower beam was adjusted to the "noncalibration" position, by a small "fine tuning" adjustment.

PHOTOCELL
OUTPUT
100 MV/cm
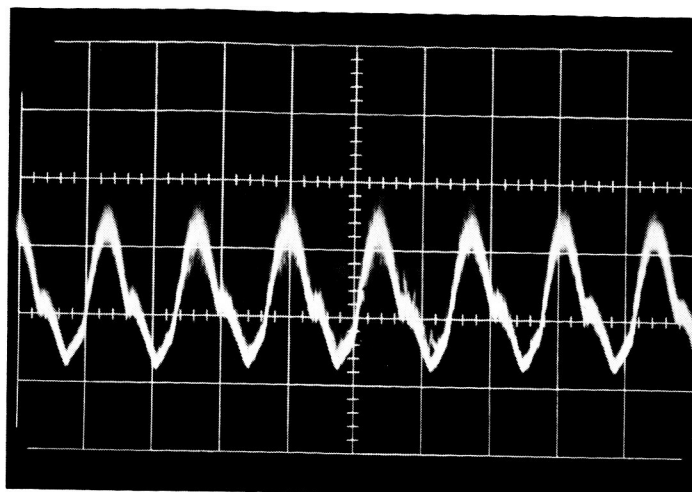
RUN 705
2 MILLISEC/cm

PREDOMINANT
FREQUENCY = 360 Hz

PHOTOCELL
OUTPUT
50 MV/cm

RUN 705
(LITHIUM)

10 μ SEC/cm
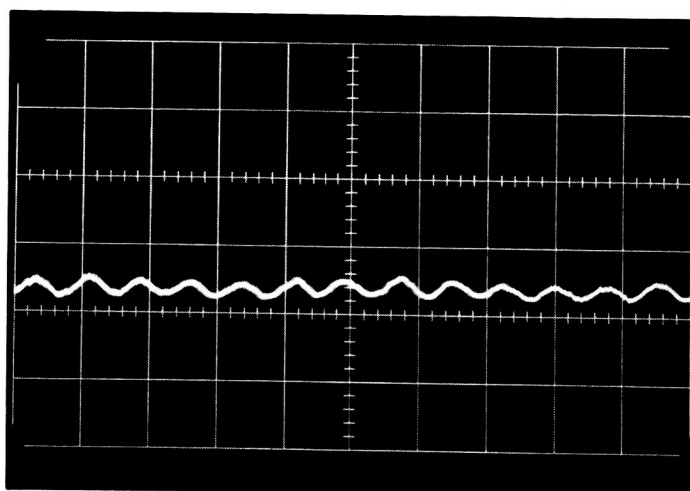
PREDOMINANT
FREQUENCY $\approx$ 132 KHz

$\mathfrak{C}_L$, Z = 14 cm

PHOTOCELL
OUTPUT
10 MV/cm

RUN 705
(LITHIUM)

5 μ SEC/cm
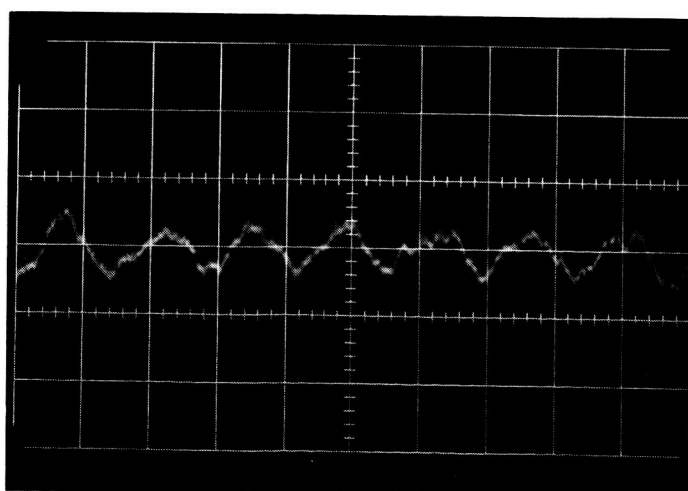
PREDOMINANT
FREQUENCY $\approx$ 140 KHz

$\mathfrak{C}_L$, Z = 114 cm

Figure 31.   Photograph Showing Characteristic Frequencies

UPSTREAM
PHOTOTRACER

(10 MV/cm)

DOWNSTREAM
PHOTOTRACER
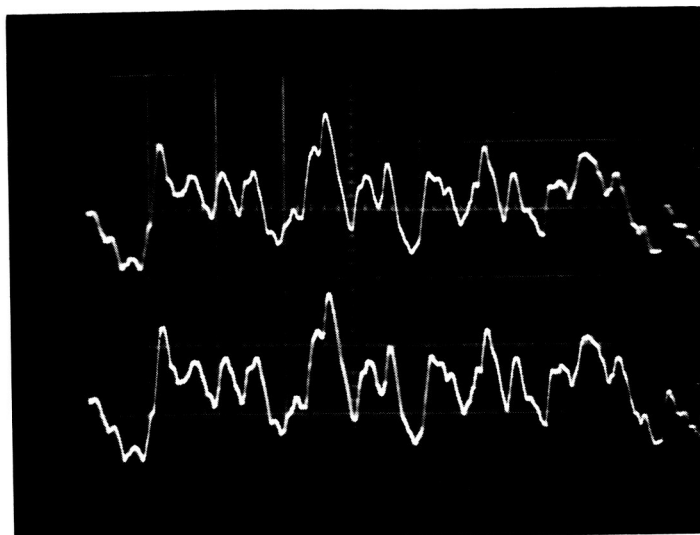
REFERENCE
CALIBRATION

$\Delta Z = 0\,cm$

5 μ sec/cm
Z = 114 cm
RUN 504 (SODIUM)

UPSTREAM
PHOTOTRACER

(10 MV/cm)

DOWNSTREAM
PHOTOTRACER
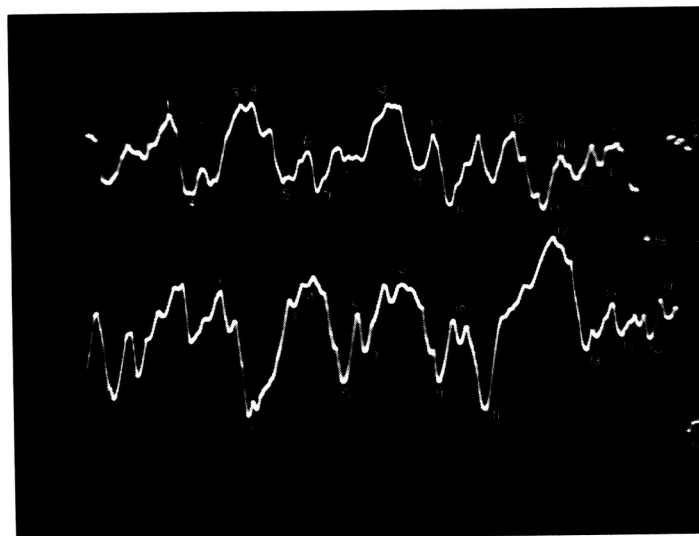
PHOTOTRACER DATA

5 μ sec/cm

$\Delta z = 8\,cm$

z = 114 cm

RUN 504 (SODIUM)

Figure 32. Photographs Showing Phototracer Reference and
Velocity Measurements

P0310

of points lying in the time delay range $\tau - \Delta\tau$ to $\tau + \Delta\tau$ are plotted as a function of τ. Here, $\Delta\tau$ = characteristic readout time error - which was ~ 0.2 μsec on the 2 μsec/cm scale.

After plotting these distributions, two characteristic time-delays result. The first is τ_{mp}. This is the "most probable" time delay, and corresponds to the peak of the distribution function.

The second characteristic time is $\bar{\tau}$, defined as that time beyond which the area under the smooth curve resulting from the data (e.g., best least-squares fit) is half the total area under the curve.

These time delays define two important characteristic velocities. These are:

$$v_{M.P.} \equiv \frac{\Delta z}{\tau_{M.P.}} \quad \text{(most probable velocity)}$$

and

$$\bar{v} \equiv \frac{\Delta z}{\bar{\tau}} \quad \text{(average velocity)}$$

where Δz = displacement between photomultipliers.

h. <u>Observations</u> - The distribution functions for plasma velocity, obtained using the phototracer method were generally of remarkably good quality. However, under certain circumstances, appropriate to various experimental runs, the plots showed one major peak and/or more (sometimes as high as five) sub-peaks. Possible explanations for these sub-peaks are:

(1) A geometric velocity profile

(2) Multiple species velocities for different atoms and/or ions

(3) Misinterpretation of regular modulated frequencies

(4) Experimental error

These explanations were studied in greater detail by the following methods:

(1) Observations at various radial positions along a chord

(2) Use of selective band-pass filters

(3) Identification of "regular" frequencies

(4) Error analysis

4.4.5 PHOTOTRACER MEASUREMENTS

Over 200 photographs of the exhaust have been taken with this system.
Recognizable signatures of light fluctuations associated with local
fluctuations in plasma electron density (see Refs. 22 and 23 and Figs.
31 and 32) have been observed on Tektronix 555A dual-beam oscilloscope
traces of the two focused photomultipliers. The sweep rates and time
delays as well as the accuracy of the focusing have been calibrated.
By focusing the two photomultiplier tubes at the same point in the
plasma, it was possible to determine the correspondence between signa-
tures. This was found to be excellent. Next, in order to check the
circuitry for time lags, a given signal from one photomultiplier tube
was passed through the circuitry of both photomultipliers and the sys-
tem balanced to give zero time delay for all scales from 1 millisec/cm
down to 0.1 μsec/cm. Most of the data were taken with oscilloscope
sweep rates of 2 and 5 μsec/cm. This resulted in observable time shifts
of from essentially zero cm to as much as 4 cm on the oscilloscope
photographs.

In the first set of experiments the jet was observed at a median posi-
tion of 118 cm (i.e. one unit focused at 114 cm and the second at 122
cm) downstream from the anode face, and "viewing" perpendicular to the
jet through its diameter. The resulting photographs were studied for
time delays.

A typical plot of the distribution of the time-delay measurements is shown
in Fig. 33.

Since a purely one dimensional, one component exhaust velocity distri-
bution would correspond to a delta function located at some specific
value of τ, it appeared that either the various species (Li atoms, Li
ions, hydrogen atoms, hydrogen ions and impurities) were traveling at
different velocities, or there exists a radial distribution of velocities.
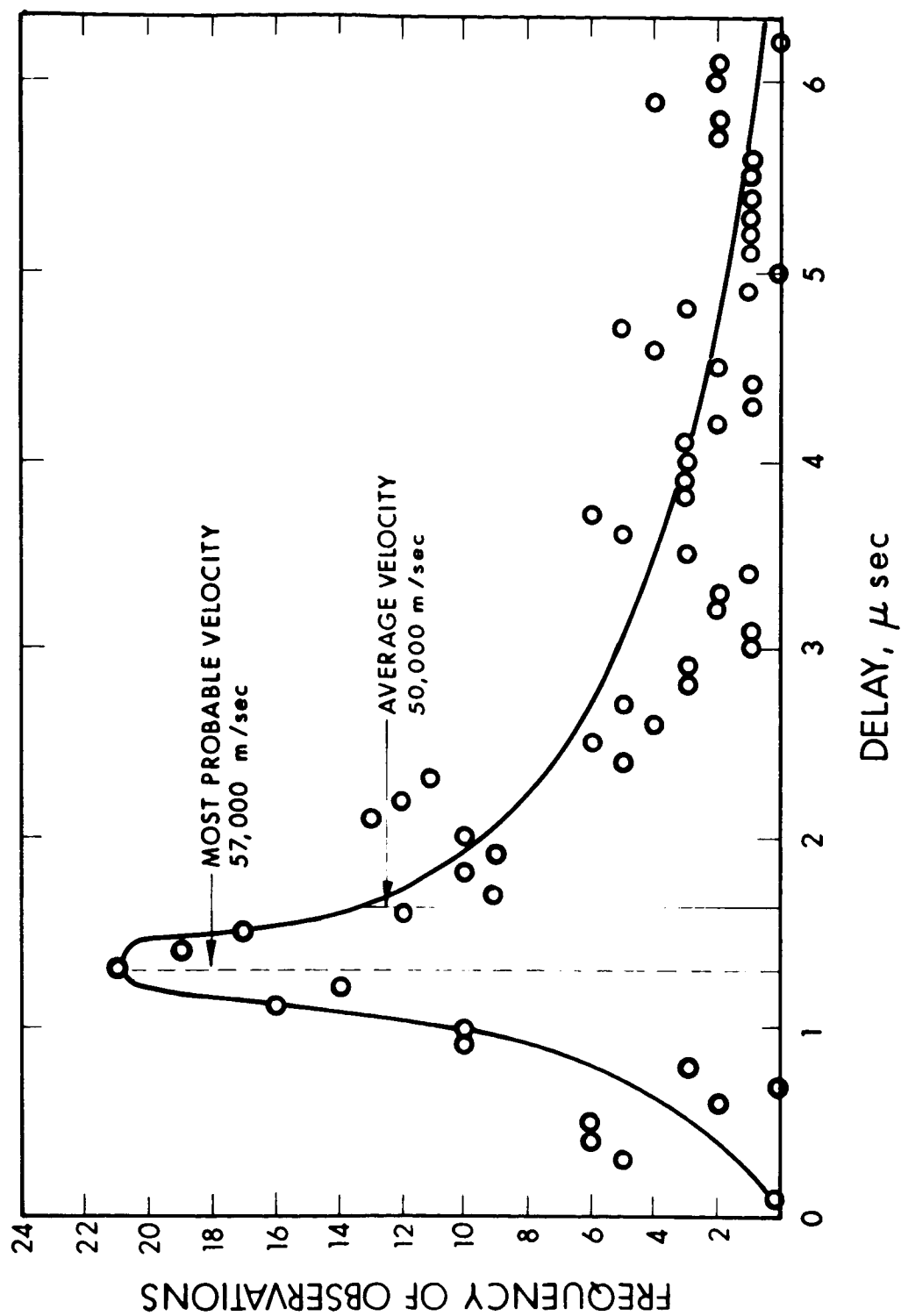
Figure 33. Experimental Phototracer Time Delay Distribution

To check the former possibility optical band pass filters were inserted in the light path and similar measurements were made. The principal conclusion of these tests was that Li I and Li II appear to have very similar velocities at any given point (peaks in their respective distribution functions occurred at essentially the same time delay) but that the Li I was primarily on the outside of the exhaust beam while Li II was primarily on or near the jet centerline.

However, a very interesting phenomena was also uncovered upon careful study of the phototracer velocity distributions resulting from Runs 720, 721 (lithium and hydrogen) and Run 722 (hydrogen only). While initially appearing to be a possible experimental error, a small but distinct "sub-peak" was found to exist on the distributions resulting from the photo-tracer data for Runs 720 and 721, while this sub-peak did not exist on Run 722. The velocity corresponding to this sub-peak ranged from 1.38 to 1.42 times the velocity of the primary peak of the distribution function and was observed only when looking at the centerline.

If one considers the possibility of multiple ionization (i.e., the existence of small amounts of Li III — that is, doubly-ionized lithium) it is distinctly possible that certain doubly ionized species, falling through a given potential drop would acquire velocities exceeding the velocity of a singly ionized atom of the same type by a factor of $\sqrt{2}$. This is remarkably close to the experimental values (viz. 1.414 compared with 1.38 to 1.42) and, interestingly enough, does not appear in the hydrogen data — which is plausible since hydrogen cannot exist in a doubly ionized state.

The next series of experiments, also performed at $Z = 118$ cm, involved viewing the jet at different positions off the centerline. In this way different chords, from the diameter to the edge of the jet, are viewed by the phototracer system. The results of this test definitely indicated the existence of a radial velocity profile. The results at $r = 5$ cm

7053-Final

were substantially identical with those at $r = 0$ (i.e. centerline) and indicated a most probable velocity of $(5 \pm 1) \times 10^4$ meters/sec. However, at $r = 10$ cm the peak of the distribution was at $(2 \pm 0.4) \times 10^4$ meters/ sec and at $r = 15$ cm the peak was at $(1.3 \pm 0.4) \times 10^4$ meters/sec.

The final experiment was a series of measurements at a position very near the exit plane (median position $Z = 14$ cm from anode face, or about 5 cm from the downstream magnet housing). The principal result of this measurement was the existence of considerably greater time delays indicating lower velocities. The peak of the distribution of these measurements corresponded to $(2.2 \pm 0.4) \times 10^4$ meters/sec. Provided these measurements are valid, the results indicate that the velocity of the beam is more than doubled in the region external to the engine components.

This behavior is not unreasonable when one invokes the concept of electromagnetic acceleration by volume body forces acting essentially as a "magnetic nozzle" throughout the plasma exhaust region, as further discussed in Subsection 4.5.

Experiments were also performed with ALPHA operating on sodium propellant. The results were similar in all respects except the measured time delays were distinctly longer (i.e., lower velocities) than with lithium. These experiments were also conducted at $z = 118$ cm. The results of the parametric phototracer experiments are summarized in Table III.

4.5 CURRENT DENSITY AND MAGNETIC FIELD PROBE MEASUREMENTS

4.5.1 INTRODUCTION AND THEORY

Measurements were made of the magnetic fields of ALPHA in order to help explain the mode of operation. Two important questions had been asked which detailed magnetic field measurements might answer:

TABLE III

PHOTOTRACER RESULTS

Species	Run	z(cm)	$\bar{v}_{phototracer}$	$\bar{U} \equiv T/\dot{m}$
			(Kilometers/sec)	
Li I	720	14	21 ±4	48 ±2
Li II	720	14	21 ±4	48 ±2
Li I	721	14	22 ±4	50 ±2
Li II	721	14	22 ±4	50 ±2
Li I	720	118	50 ±10	48 ±2
Li II	720	118	50 ±10	48 ±2
Li I	721	118	52 ±10	50 ±2
Li II	721	118	52 ±10	50 ±2
H I	723	118	70 ±12	65 ±3
NA I	503	118	18 ±4	22 ±1
NA I	504	118	20 ±4	22 ±1

a. Do the anode to cathode arc currents extend downstream into the plasma?

b. Do azimuthal "Hall" currents exist within the plasma?

The relationship between currents and magnetic fields came from Maxwell's equations. For the case of steady axisymmetric currents and fields, the equations are (Ref. 24):

$$-\partial B_\theta/\partial z = \mu_o J_r \tag{1}$$

$$\partial B_r/\partial z - \partial B_z/\partial r = \mu_o J_\theta \tag{2}$$

$$(1/r)\, \partial(r\, B_\theta)\partial r = \mu_o J_z \tag{3}$$

$$(1/r)\, \partial(rB_r)/\partial r + \partial B_z/\partial z = 0 \tag{4}$$

Notice that Eqs. (1) and (3) contain B_θ, J_r and J_z, while Eqs. (2) and (4) contain B_r, B_z and J_θ. This means that the two sets are uncoupled, which leads to a great simplification in the reduction of data. The determination of the current densities from the measured magnetic fields requires a differentiation of experimental data. In order to find the net axial current through a ring of radius R, we use the current density integral form of Eq. (3)

$$I(R, z) \equiv \int_0^R J_z (r, z)\, 2\pi\, rdr$$

$$= 2\pi R\, B_\theta(R,z)/\mu_o \tag{5}$$

In principle, Eq. (2) could be used to determine the axial and radial distribution of J_θ, and Eq. (4) is a check of compatibility of the measured B_r, B_z. These detailed calculations were not done because the accuracy of the data and the rather coarse grid of points for which data were taken do not justify differentiation. The existence of a J_θ can be

determined by simply observing if B_r and B_z change when the arc is turned on. If the azimuthal J_θ were in the same direction as the current in the magnetic coils, the B_z on axis would increase in absolute value (paramagnetic effect); while if the induced J_θ were in the opposite direction as the coil current B_z on axis would decrease (diamagnetic effect).

4.5.2 PROBE CONSTRUCTION AND CHECKOUT

Hall effect transducers were chosen to measure the magnetic fields. A probe was constructed (see Figs. 34 and 35) which contains three transducers on mutually perpendicular axes. The elements were encased in a water jacket which kept their temperature rise below $1^\circ C$. The active probe was encased in a boron nitride insulator to prevent arc attachment. The probe was mounted on a traversing mechanism which allowed axial and radial motion.

The Hall effect magnetic probe was calibrated and checked for linearity by placing the probe in a magnetic field which had been calibrated by a Bell gaussmeter. The probe was traversed through the magnetic field of the coils inside the test facility. A torch was used to determine what effect heat may have either upon probe alignment or upon transducer heating. It was determined that the indents used for probe positioning were not accurate enough to return exactly to the same location (the situation was even worse after some coating by condensing alkali during the run). The heating effect was negligible except upon the azimuthal probe. The change of B_θ due to severe heating was about 10 percent of the value recorded during the experiment.

4.5.3 EXPERIMENTAL RESULTS

Magnetic fields were measured with the arc off and on to determine the differences. While taking the data, it was noted that the axial and
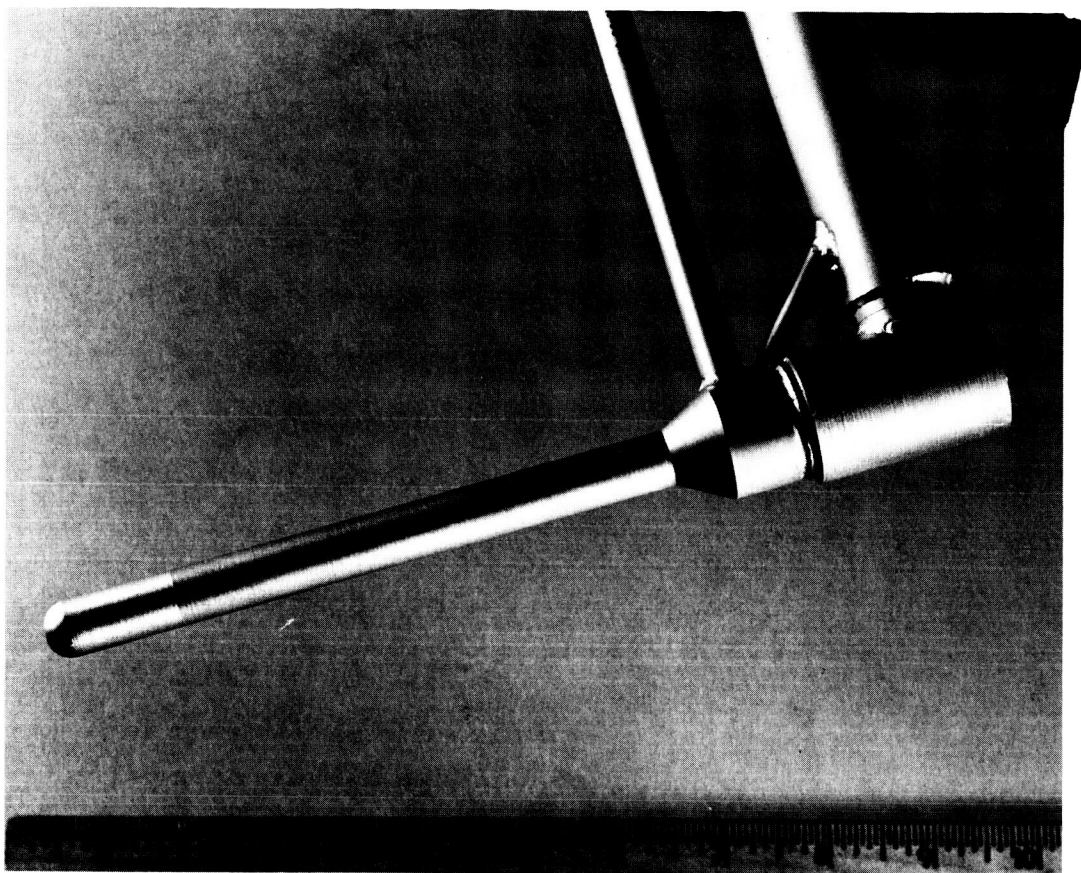
Figure 34. Photo of Hall-Effect Magnetic Probe

6690

COPPER SHEATH

STAINLESS TUBE

HALL EFFECT
TRANSDUCER

STAINLESS
TRANSDUCER
WELL
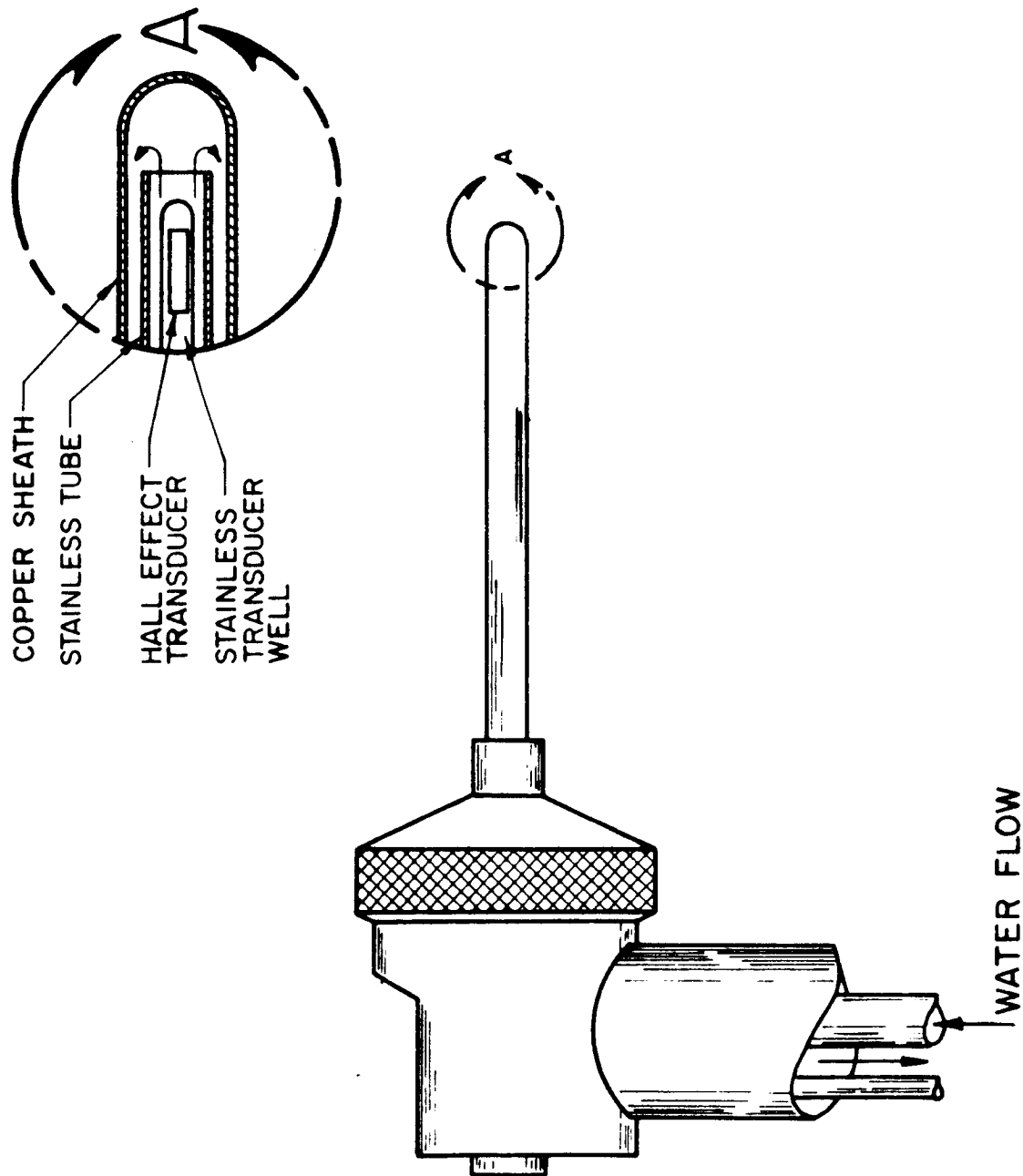
WATER FLOW

Figure 35. Axial Current Density Probe. Hall Effect Transducer Carried in Water Cooled Probe Used to Measure Tangential Field, B_θ, Induced by Axial Current, J_z. Arrows Indicate Water Flow

radial components of the magnetic field were steady and reproducible. The difficulties in measuring the azimuthal magnetic field arise largely because their value is an order of magnitude smaller, and small misalignments can cause axial or radial applied fields to intersect the azimuthal transducer.

Typical data for the axial magnetic field is shown in Fig. 36. This shows the axial magnetic field as a function of location downstream of the magnet housing during a lithium run. A small diamagnetic effect indicates the existence of some J_θ "Hall" current. Data was not taken closer to the thrustor due to interference with the arc.

Figure 37 shows the radial distribution of B_z and B_r for $z = 7.6$ cm downstream of the magnet housing. Again the B_z shows some diamagnetic effect, which decreases for large radius. B_r showed only very slight change. In order to eliminate the possibility of errors due to positioning, the arc was interrupted while the probe was sitting at $r = 2.54$ cm. The change is indicated on Fig. 37 by the on-off marks.

Data for the azimuthal magnetic field is shown in Fig. 38. There is some scatter in the data which is probably due to positioning error and thermal effects. The readings with arc off are proportional to the current in the magnet coil, and are due to probe misalignment. The intersection of the arc on and arc off curves did not occur at $r = 0$, which is due to misalignment of the thrustor or the probe traversing mechanism. For data reduction the center of the arc was assumed to be the point where B_θ did not change when the arc was turned off or on.

Using Eq. (5) and the above B_θ data, the net current inside a ring of radius R was computed for several axial locations and is shown in Fig. 39. The relative accuracy of these curves gets worse at large radius due to subtraction of nearly equal B_θ for arc on and arc off to get a
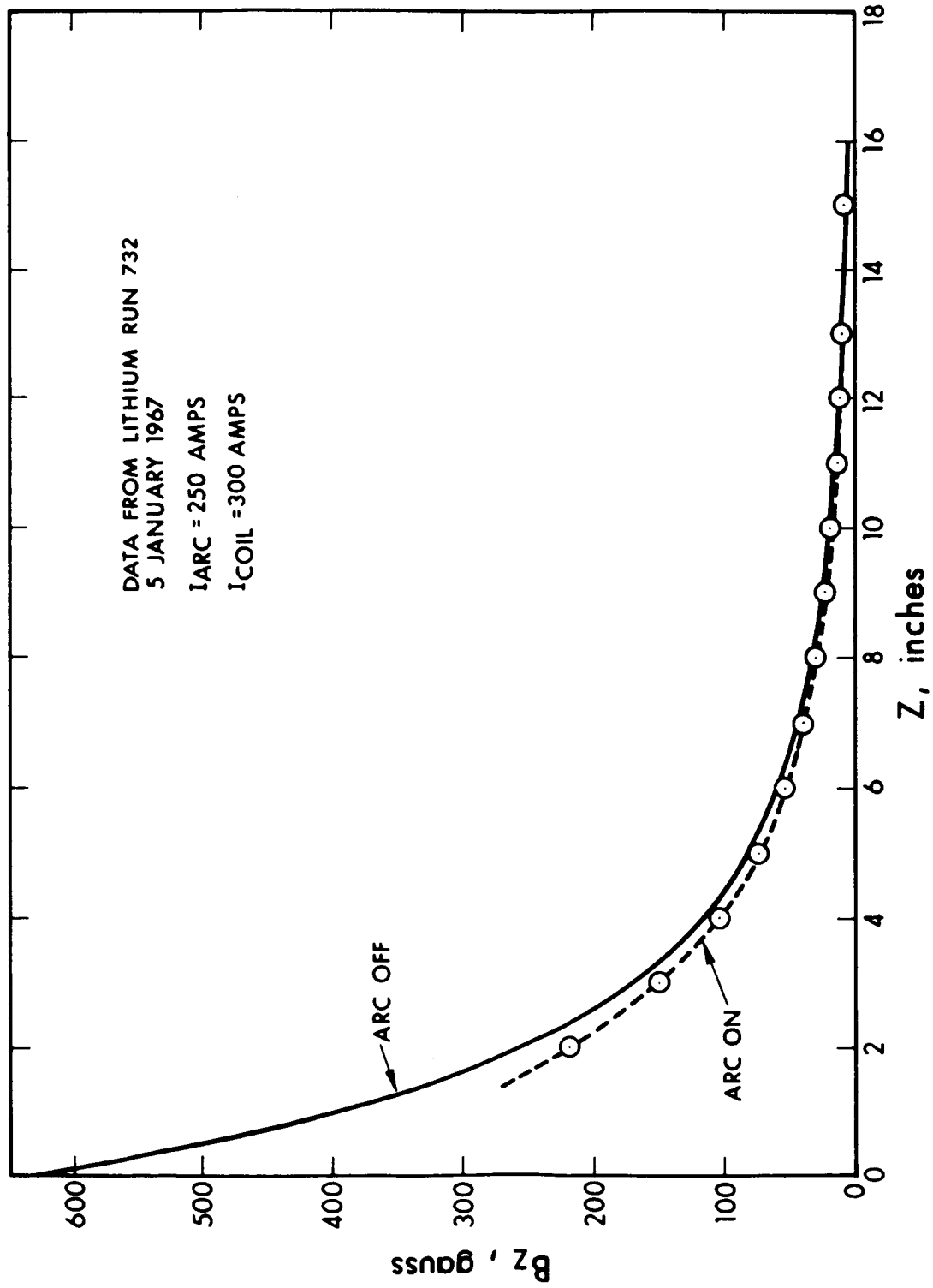
Figure 36. Axial Magnetic Field Along the Axis

73626596
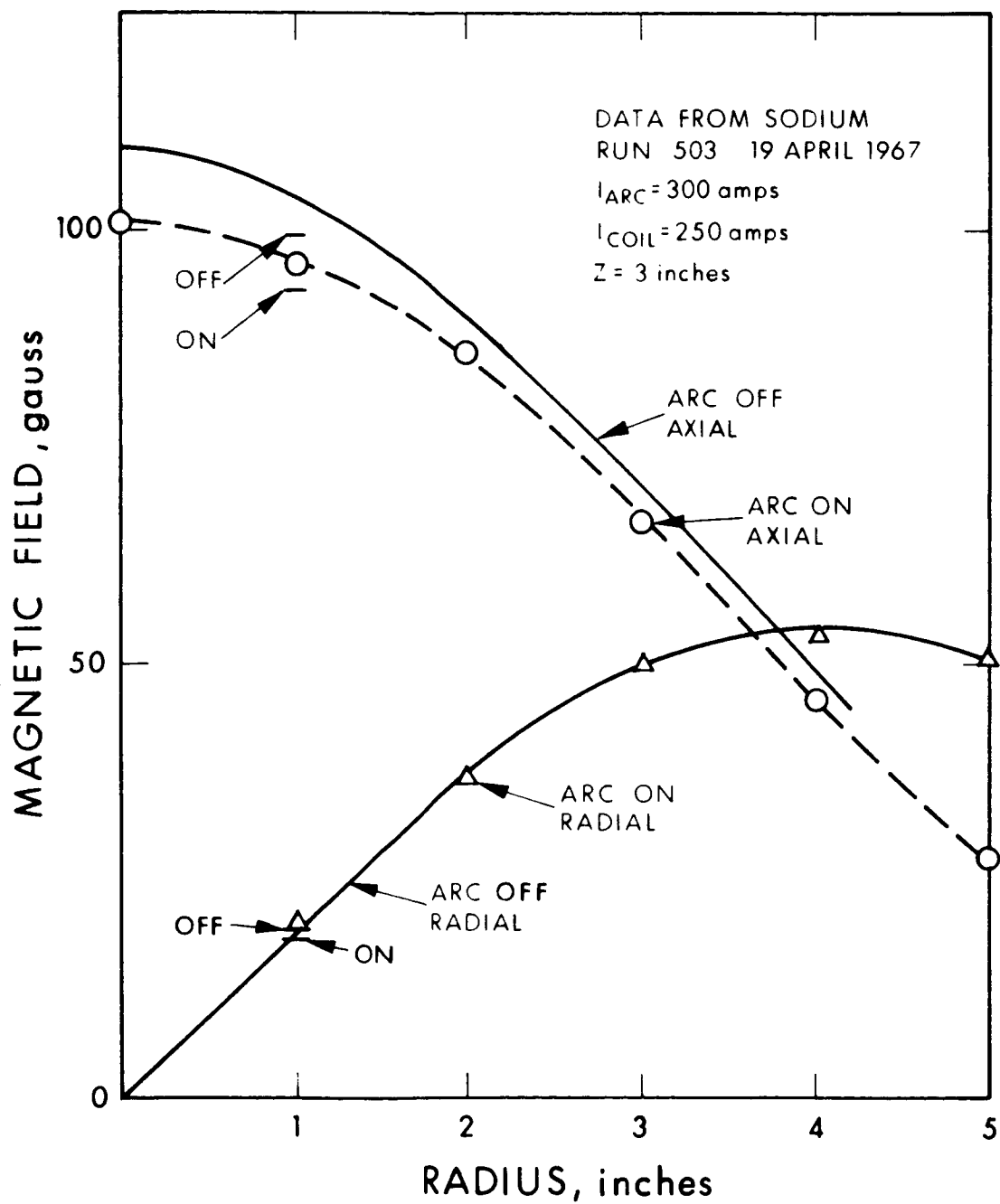
Figure 37. Axial and Radial Magnetic Field versus Radius
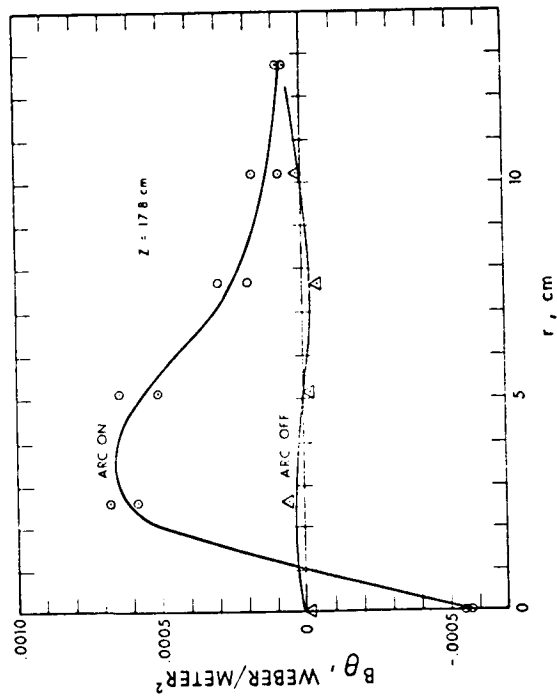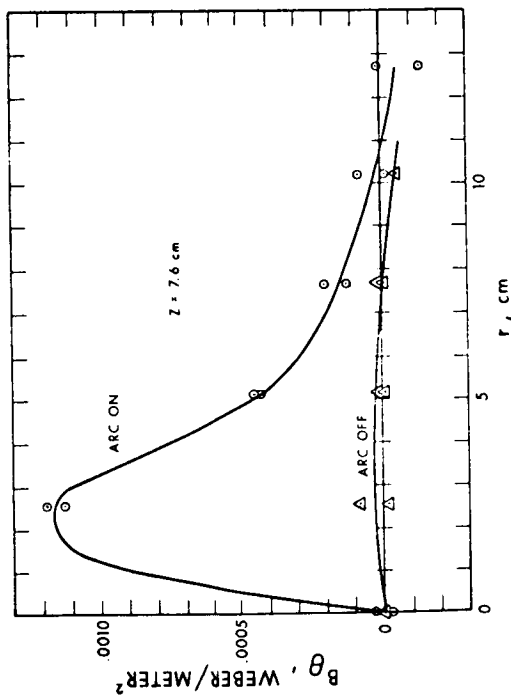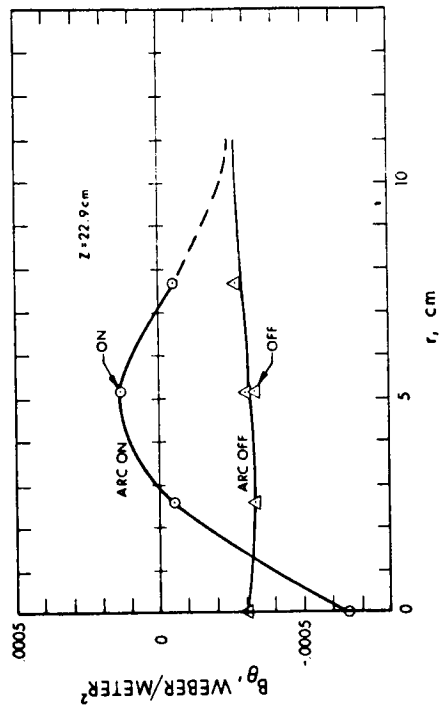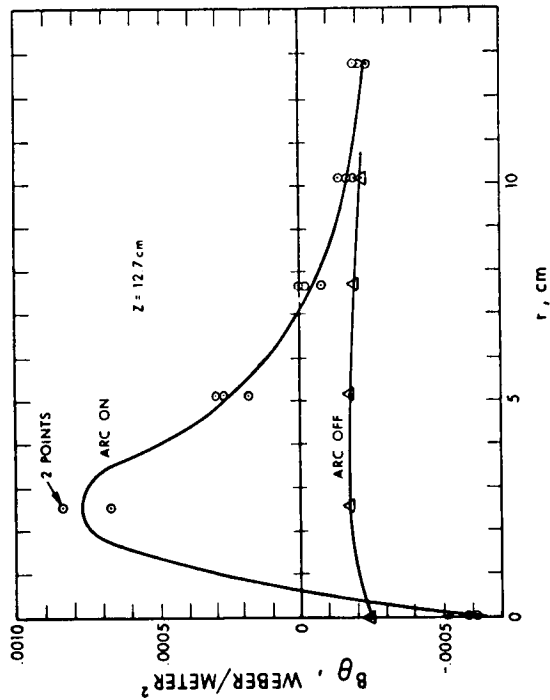
Figure 38. Azimuthal Magnetic Field versus Radial Position
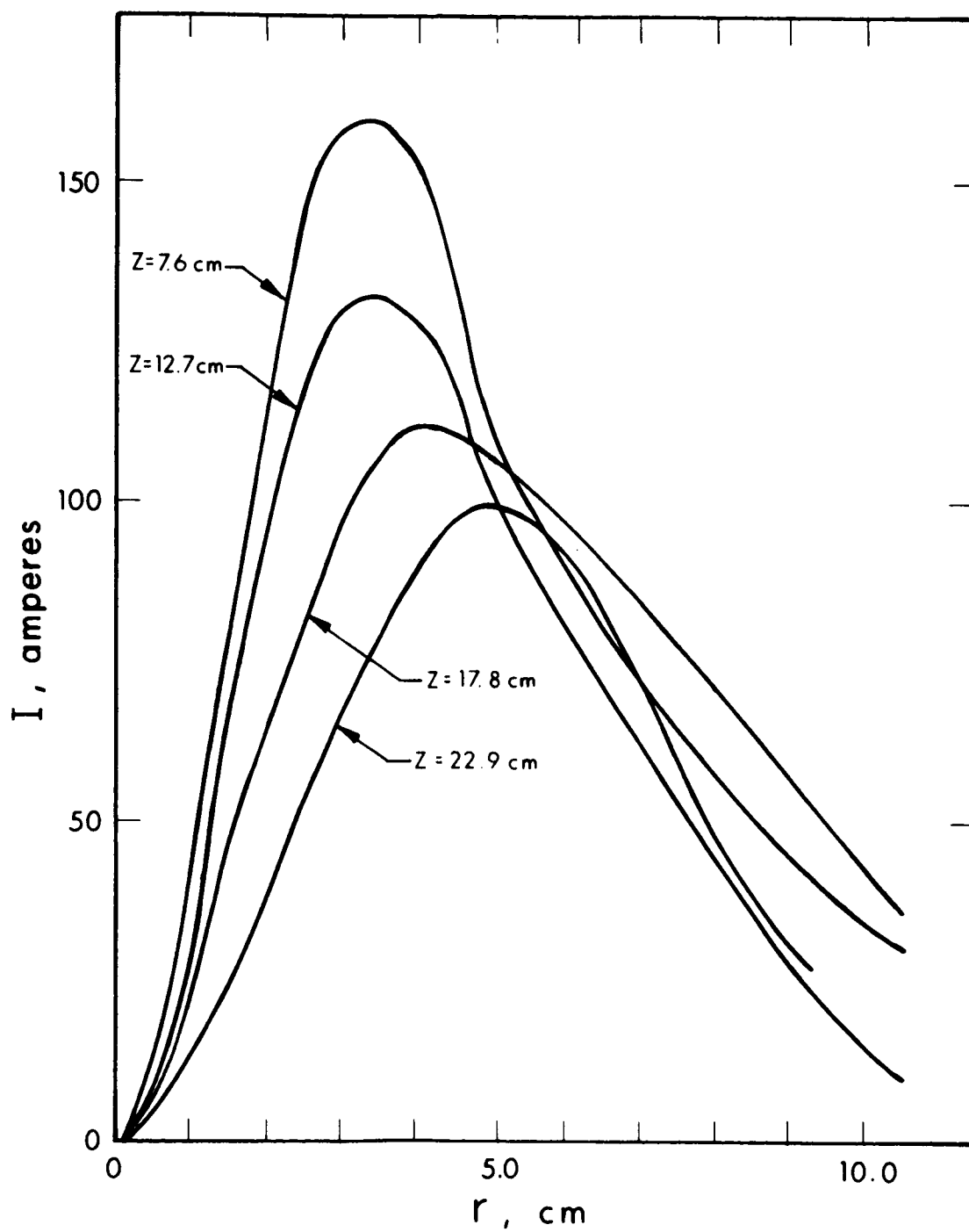
Figure 39. Current Density Integral versus Radial Position

small difference, which was then multiplied by a large radius. The curves would go to zero if there were no net current. In theory, the current density could be obtained by differentiation of the curves of Fig. 39; this was not done because the number of radial locations at which data was taken was too few. The peaks of the curves of Fig. 39 are shown on Fig. 40, which shows the amount of current which flows past each point. Data were not taken closer than $z = 7.6$ cm because of interference with the arc. It is believed that $I \to 0$ at $z \approx 50$ cm since the arc attached to the total beam calorimeter when it was placed that close. Beyond $z = 50$ cm attachment was not observed.

An interesting observation is that when the arc is restarted on hydrogen the azimuthal magnetic field (and hence arc current) did not appear. It was not until operation was returned to sodium and the tank pressure dropped below 10^{-3} Torr, that the current loops were again detected.

4.5.4 CONCLUSIONS AND RECOMMENDATIONS

a. Axial electric currents existed at least 0.33 meter downstream of the magnet housing (the greatest distance ever probed).

b. A slight diamagnetic effect indicates the presence of some azimuthal "Hall" currents.

c. Poor signal-to-noise level makes accurate determination of axial currents difficult. The big difficulty is that the azimuthal fields are an order of magnitude smaller than the axial ones. Errors may be due to thermal deflections.

d. More accurate and convenient results could be obtained by employing a probe with a smooth transverse with position readout rather than the indent system.

e. The best method found to get reliable results was to extinguish and restart the arc, using only the changes in probe response.
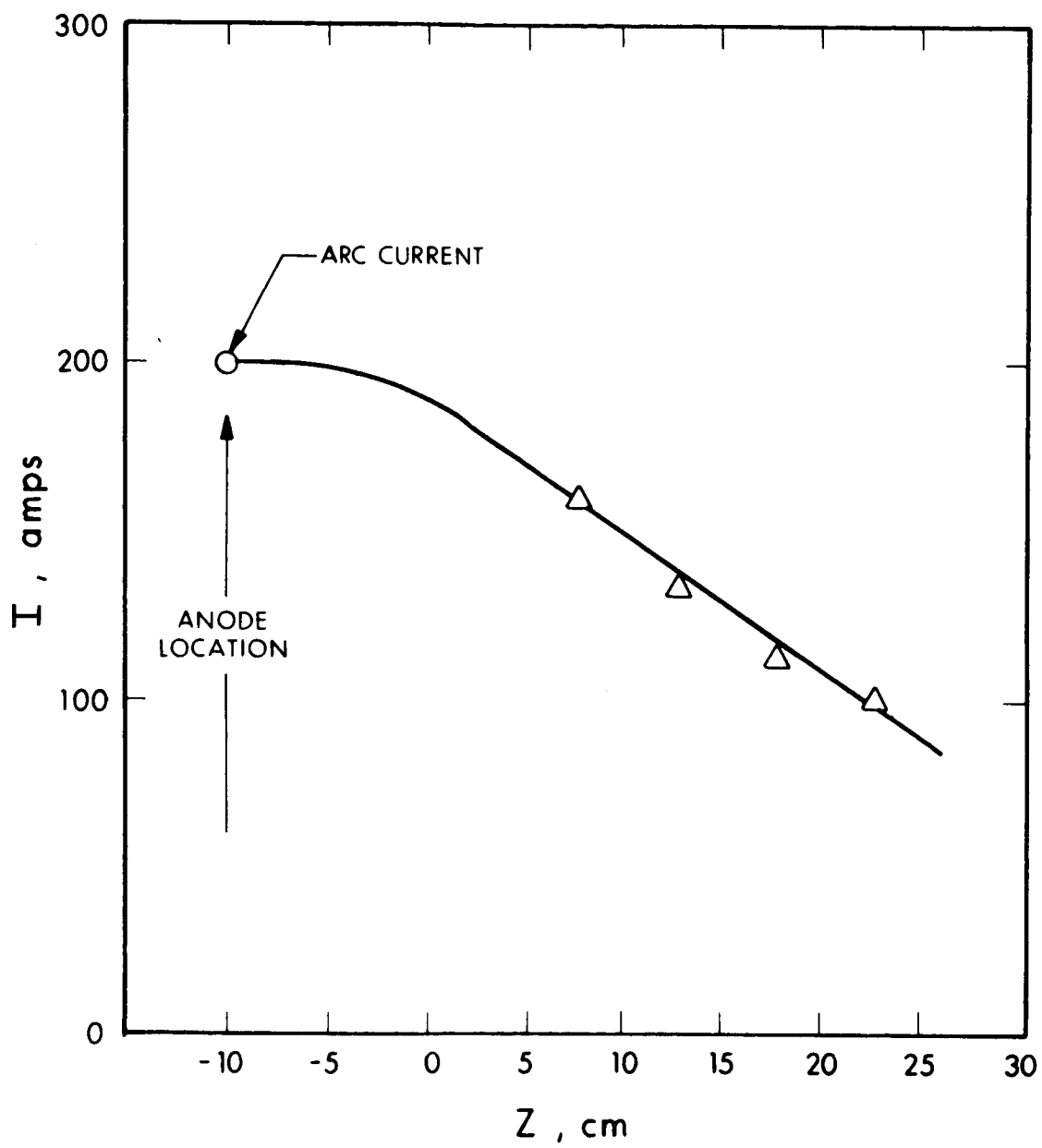
Figure 40. Axial Extent of Currents

4.6 DIAGNOSTIC MEASUREMENTS WITH A LOOP MAGNETIC PROBE

4.6.1 INTRODUCTION

The ALPHA device, which is nominally a dc powered, steady state thrustor, actually exhibits certain time varying characteristics. The very existence of fluctuating signatures, and regular frequencies, apparent in the the phototracer results suggested the possibility of other time varying phenomena. For this reason, it was decided to investigate the possible existence of time varying magnetic fields and to study what, if any, characteristic frequencies might be observed.

4.6.2 DIAGNOSTIC MEASUREMENTS

The primary diagnostic results of this technique were measurements of the time variations of the radial component of the magnetic field. A noncooled probe, consisting of 60 turns of 0.010 in. insulated copper wire in the form of a loop, was fabricated. The active diameter (i.e., across the loop) is 0.5 in.

The theoretical foundation upon which the magnetic loop (or magnetic induction) probe is based (see Refs. 25 and 26) is essentially Maxwell's induction equation, integrated over the active probe area, which gives

$$V = NA\frac{dB}{dt}$$

For this probe, N = 60 turns and A = 1.26×10^{-4} m^2. If B is expressed in gauss, t in seconds and V in volts, one finds

$$V = 7.6 \times 10^{-7} \frac{dB}{dt}$$

The probe was placed 6 inches downstream of the downstream magnet housing face, and 6 inches off the centerline (just outside the plasma). The amplitude of the induced voltage (displayed on a Tektronix 551 oscilloscope) varied from 0.1 millivolt for the case of an applied magnetic field with the arc off, to about 1 millivolt when the arc was operated on lithium to about 6-8 millivolts when the arc was operated on hydrogen (see Fig. 41). Distinctly reproducible frequencies were also observed. These fell into three groups. The first group showed characteristic frequencies of 60, 120 and 360 Hz. It is believed that these values are associated with power supply "ripple." The next group consisted of values between 200,000 and 400,000 Hz. For any given applied magnet current the frequency was unique and constant. As the magnet current was increased the observable frequency in the output of the dBr/dt probe was found to increase in a simple direct proportion. That is, frequency was directly **proportional to B.** Somewhat surprisingly, only the <u>frequency</u> varied, not the <u>amplitude</u> of the induced voltage. These results are shown in Fig. 42. Finally a frequency of about 1 megacycle/sec was also observed. Since the L-C ringing **frequency** of the equivalent R-L-C probe circuit was about 1 megacycle/sec, this may be the source of **this** particular frequency although the possibility of plasma origin has not been systematically studied to date.

The linear dependence of the observed characteristic frequency with the applied magnetic field coil current (approximately 265 kHz at 300 amperes, 310 kHz at 350 amperes and 350 kHz at 400 amperes **magnet** coil current), and the inverse effect of the **molecular** weight upon the amplitude of the probe output suggest possible ion cyclotron motions. This is not completely **certain, however, since the effects of molecular weight** and magnetic field seem to be uncoupled; that is the former affects the amplitude while the latter only affects the frequency of the response of the magnetic loop probe.
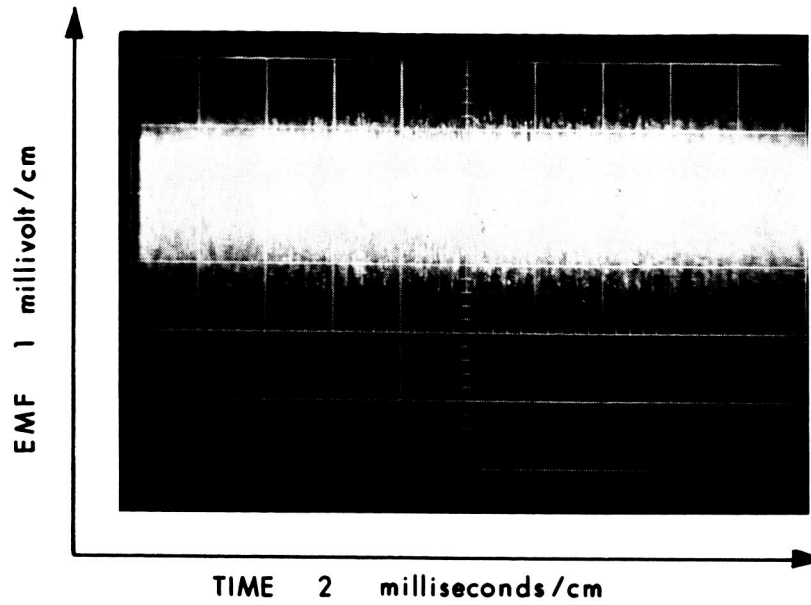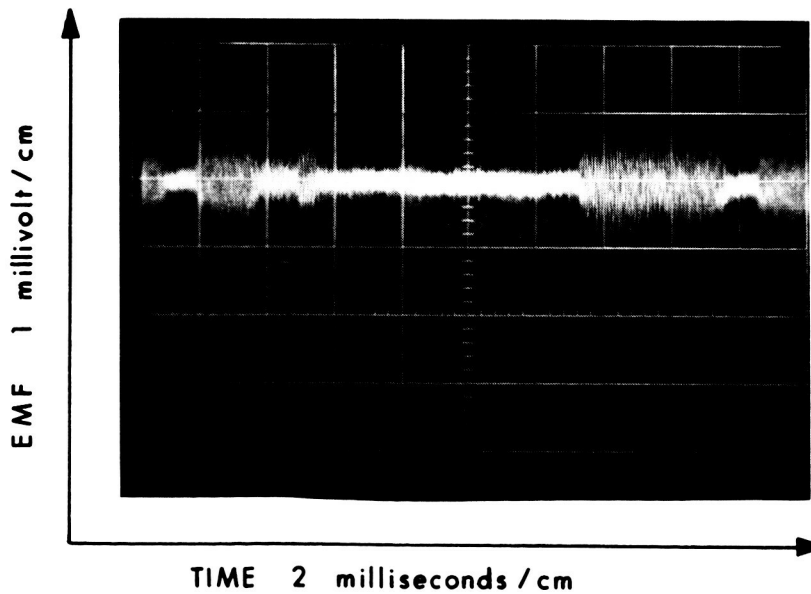
Figure 41. Loop Magnetic Probe Signals for Hydrogen
and Lithium

P0311

7 MARCH 1967
RUN 738

TIME 2:00 p.m.
HYDROGEN

MAGNET CURRENT
300 AMPS

EMF 2 millivolt/cm

TIME 5 μsec/cm
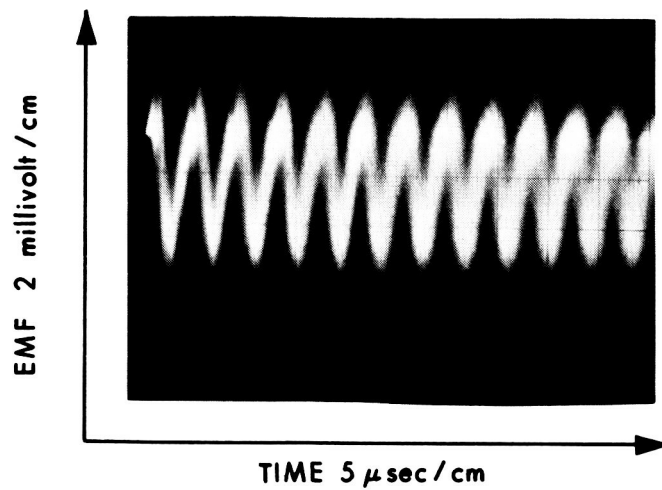
TIME 2:14 p.m.
HYDROGEN

MAGNET CURRENT
350 AMPS

EMF 2 millivolt/cm

TIME 5 μsec/cm

TIME 2:15 p.m.
HYDROGEN

MAGENT CURRENT
400 AMPS

EMF 2 millivolt/cm

TIME 5 μsec/cm
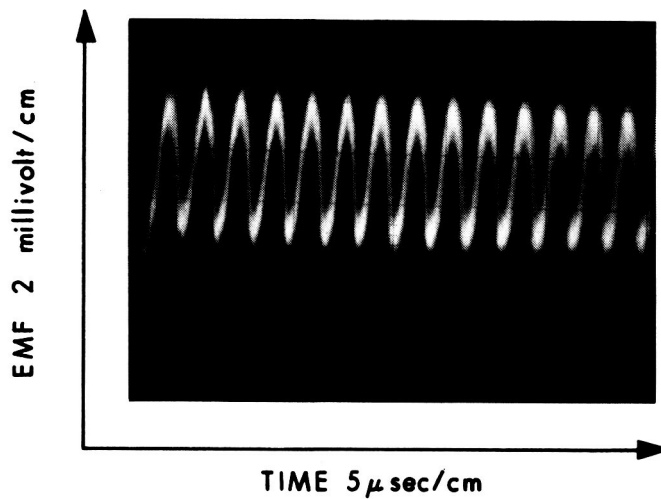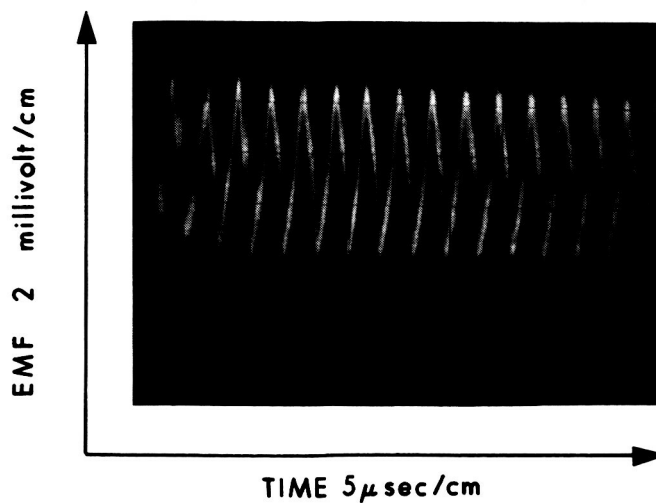
Figure 42. Effect of Magnetic Field on the Output Frequency
of the Loop Magnetic Probe

4.7 MASS-FLUX MEASUREMENTS

4.7.1 MASS-FLUX PROBE

A unique deposition probe (see Figs. 43 and 44) for the determination of the local lithium mass flux has been designed and fabricated. The measurement is based upon the time rate of change of the resistance of a continuously depositing layer of alkali metal upon an insulating substrate. A schematic of this device is shown in Fig. 44.

Basically the probe consists of a water cooled base, a boron nitride insulating substrate of width W, and two parallel conducting elements separated by a distance L. A constant potential V_o is applied through an external limiting resistance R_o. An ammeter measures the current in the circuit.

Initially, when the probe is first placed in the plasma, there is no lithium depsoited upon the insulating substrate so the circuit is open and zero current flows. As the lithium is deposited on the insulating substrate, the current is given by

$$I = \frac{V_o}{R_o + R_{Li}}$$

where

$$R_{Li} = \rho_{Li} \, L/Wd$$

$$\rho_{Li} = \text{resistivity of lithium}$$

$$d = \text{thickness of deposited lithium}$$

Since the thickness is given by

Figure 43. Photo of Mass Probe
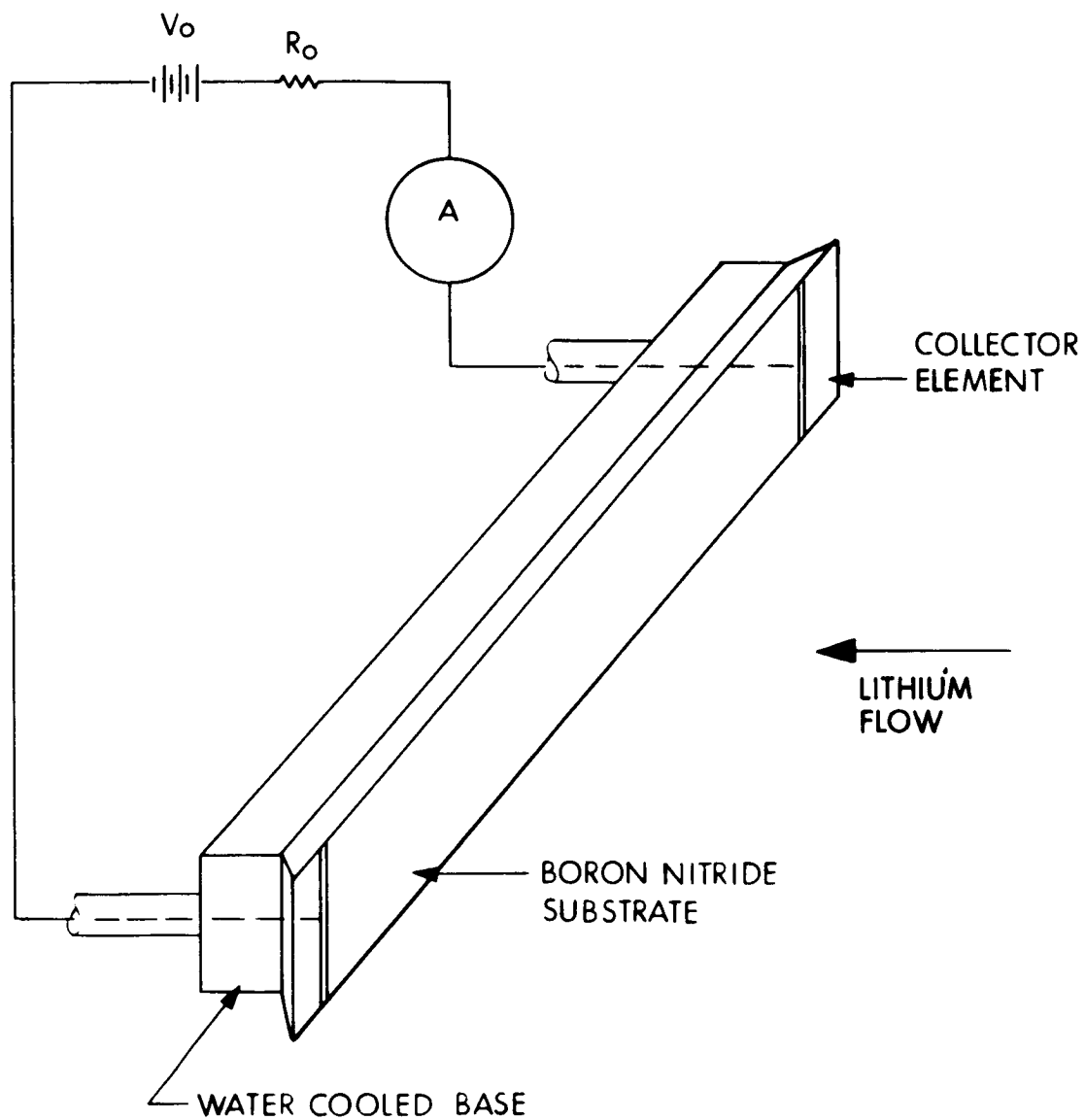
Figure 44. Schematic of Lithium Deposition Probe

73621216

$$d = \int_0^t \alpha(t) \, dt$$

where

α = rate of deposition of solid lithium

$$= \frac{\xi(t)}{\delta_{Li}} \text{ (cm/sec)}$$

where $\xi(t)$ = time dependent mass flux (g/cm^2-sec)

δ_{Li} = density of solid lithium (g/cm^3)

then

$$I = \frac{V_o}{R_o + \dfrac{\rho_{Li} \, L \, \delta_{Li}}{W \int_0^t \Phi(t) \, dt}}$$

or

$$I = \frac{V_o \int_0^t \Phi(t) \, dt}{R_o \int_0^t \xi(t) \, dt + \dfrac{\rho_{Li} \, L \, \delta_{Li}}{W}}$$

Provided the proper choice of L, W and R_o is made, there will be a considerable period during which the resistance of the lithium deposit is much greater than the external resistance, that is

$$\frac{\rho_{Li} \, L \, \delta_{Li}}{W} \gg R_o \int_o^t \dot{\imath}(t) \, dt$$

During this period

$$I \approx \frac{V_o W}{\rho_{Li} \, L \, \delta_{Li}} \int_o^t \dot{\imath}(t) \, dt$$

Differentiating with respect to time and rearranging

$$\dot{\imath}(t) = \frac{\rho_{Li} \, L \, \delta_{Li}}{V_o W} \frac{dI}{dt}$$

Thus the instantaneous value of the mass flux is proportional to the time rate of change of the current as measured by the ammeter. Changes in mass flux with either time or position are apparent from changes in the slope of the plot of current versus time of immersion. The current and time of immersion are monitored simultaneously on a recording potentiometer. The instant of immersion is controlled by placing the probe behind a shadow shield and quickly moving it to the desired radial position by means of a preset mechanical stop.

Essentially the probe behavior falls into three distinct ranges of physical phenomena. During the first brief period the lithium strikes bare substrate and condenses in a somewhat erratic fashion until a few monolayers are deposited. After about 10 monolayers have been built up, the basic interaction is lithium upon lithium and persists until about 1000-10,000 monolayers have been deposited (Refs. 27, 28,29). Finally, the layer of lithium gets so thick that edge effects and heating (due to poor thermal conduction to the water-cooled base) become important.

However, since proper choice of L, W, V_o, R_o and $\dot{m}$ can provide a period of the order of minutes during which the second mode is occurring, this is the interval during which useful data is obtained; the initial and final stages of deposition being ignored.

The reason for placing an external resistance in the circuit becomes apparent in the limit of long duration. Eventually a sufficiently thick layer of lithium is deposited that the resistance between the collectors becomes quite small (e.g., less than 1 ohm) and large currents would flow causing additional ohmic heating and nonuniformities in the lithium resistivity.

Since not all of the mass flux incident upon the probe will adhere, the true mass flux is related to the measured mass flux by

$$\xi_{true} = \frac{1}{\bar{\beta}} \xi_{meas}$$

where $\bar{\beta}$ is the average sticking fraction. In order to determine the true mass flux one must determine $\bar{\beta}$ by calibration. Probably the most direct method involves a numerical integration of the measured mass flux over the entire surface of the plasma and comparison with the total mass flow of lithium entering the system.

In order to insure that the effect of impurities upon the resistivity of the lithium deposit is small, the probe should operate in an environment in which the partial pressure of all impurities is less than 10^{-4} torr and preferably less than 10^{-5} torr (Ref. 29). Increased impurity levels will manifest themselves by greatly increasing the resistivity of the deposited layer and thereby decreasing the current flow at a given time relative to a case with negligible impurities.

Preliminary tests showed the practicality of this concept, and yielded mass fluxes in reasonable agreement with run conditions. However, two major difficulties became apparent. The first of these is related to local plasma potential fluctuations which distort (and sometimes even overwhelm) the probe voltage, making interpretation of the results very difficult. To overcome this problem, a modified deposition probe was designed and fabricated. In this device the constant potential source (i.e., a battery) is replaced with a variable power supply and an oscillator. This modulated voltage is then applied to the probe at a specific frequency and the output of the probe is passed through a narrow band-pass filter with the intent of eliminating the effects of all plasma oscillations and/or fluctuations at frequencies other than the predetermined value. Hopefully, by picking a frequency which is different from the natural values occurring within the plasma, these spurious effects can be eliminated. Of course, in this case the current versus time plot is not a simple monotonic curve but rather a periodic function with an amplitude that increases with time. By determining the time rate of change of the envelope of this signal the mass flux may, in principal, be determined.

The second major problem which remains is one of calibration. Presumably the method mentioned earlier (i.e., numerical integration across the beam) would be valid provided the value of the total propellant mass flow rate were known during the measurement. However, due to fluctuations in the feed system it is difficult to obtain an accurate **instantaneous** value of the total mass flow rate. Methods such as vacuum deposition in a bell jar were also considered, but are also subject to certain uncertainties.

Unfortunately, actual tests with the mass deposition probe (even the modified ac version) did not produce reliable results. Substantially, the device was found to be too sensitive to local plasma potential

variations. This sensitivity was emphasized by the fact that entirely different results were obtained when the probe was simply rotated at the same position within the plasma. In a sense, the deposition probe was behaving more like an E-field probe than a **mass-flux** probe. It is believed that the basic concept of the deposition probe remains valid, but a definite effort to eliminate E-field effects would be required of any future design.

4.7.2 MASS-FLUX MEASUREMENTS

The distribution of the mass of lithium accumulated on the walls of the tank was measured after a run of 30 hours duration. The various thicknesses of deposited material were measured with a micrometer. Since the tank was opened to the atmosphere for some time before the thicknesses were determined, the resultant material is **chemically** reacted lithium (probably mostly lithium-oxide, lithium-nitride and lithium-hydride). However, since the environment was common to all sections, the relative thicknesses of the deposit probably give a reasonably good picture of the lithium distribution.

The disposition of the deposit upon the tank walls is shown in Fig. 45. These measurements indicate:

    a. Very little deposit occurs on the tank walls near the engine (e.g., a window behind and to the right of the engine was clear, and objects within the tank were distinctly visible through this window, after 30 hours of operation).

    b. There is an unexplained peak in the deposit thickness on the right side of the tank at a position 6 ft from the anode, and a peak on the bottom of the tank at 7 ft.

    c. The maximum deposited thickness occurred on the end of the tank (**viz.**, 0.034 inch). Also, the end of the tank showed an asymmetry as well as a reduced value of deposition of the centerline. Note that the pressure was 10^{-4} torr, slightly higher than other recent runs.
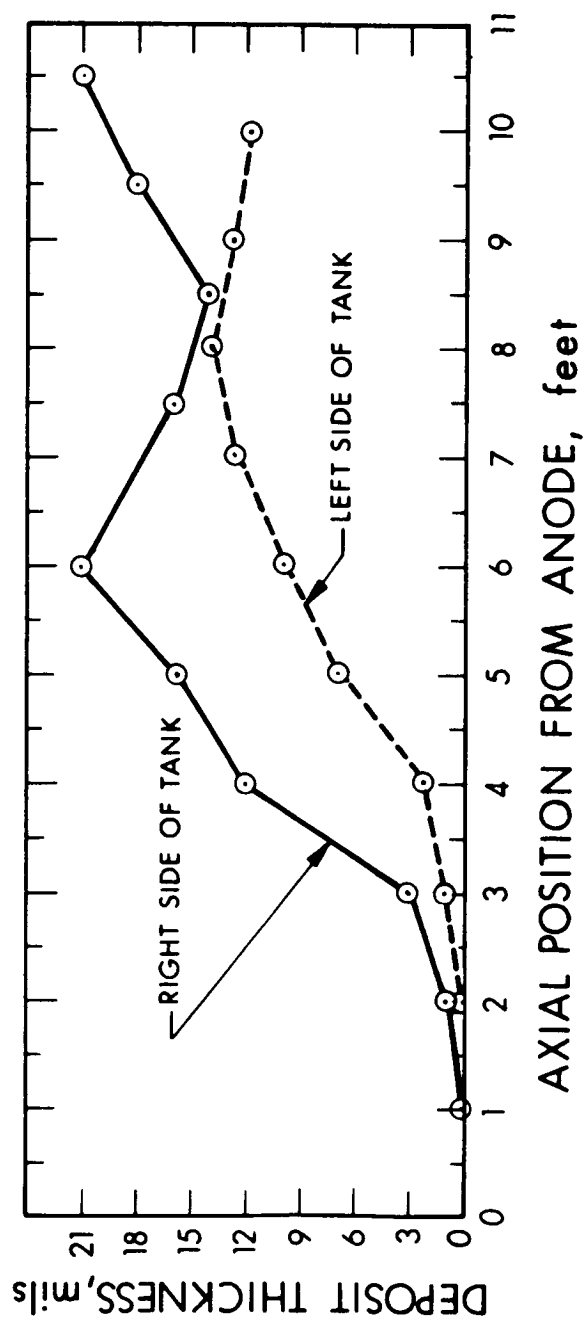
Figure 45a. Measured Deposit Thicknesses
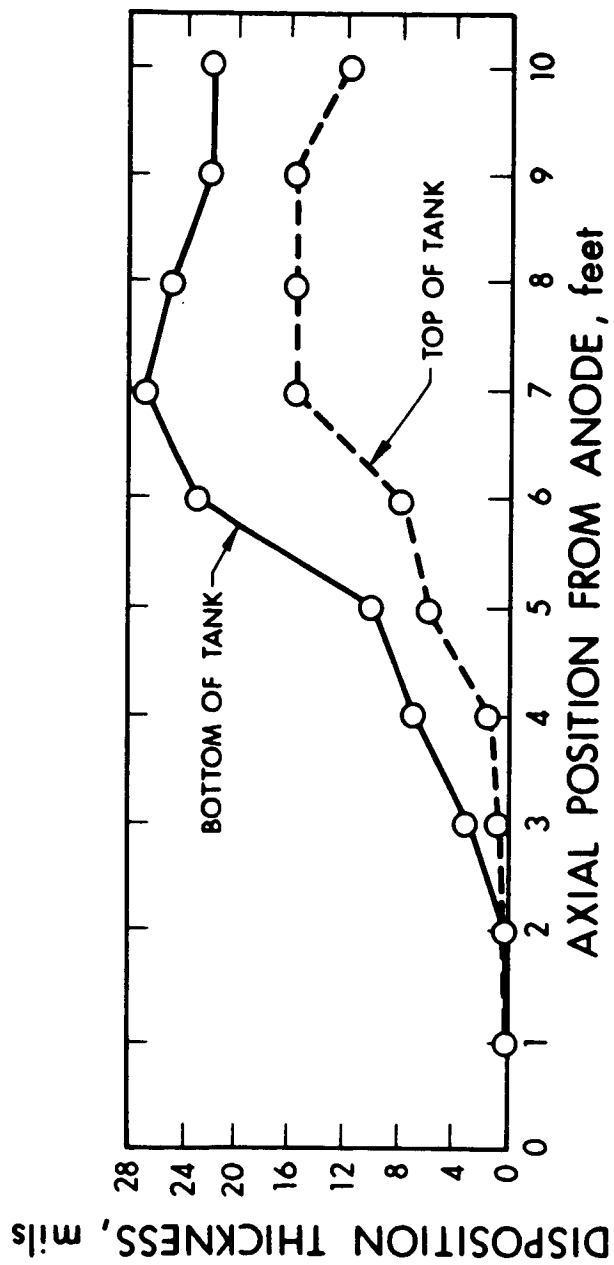
Figure 45b. Measured Deposit Thicknesses

73626594
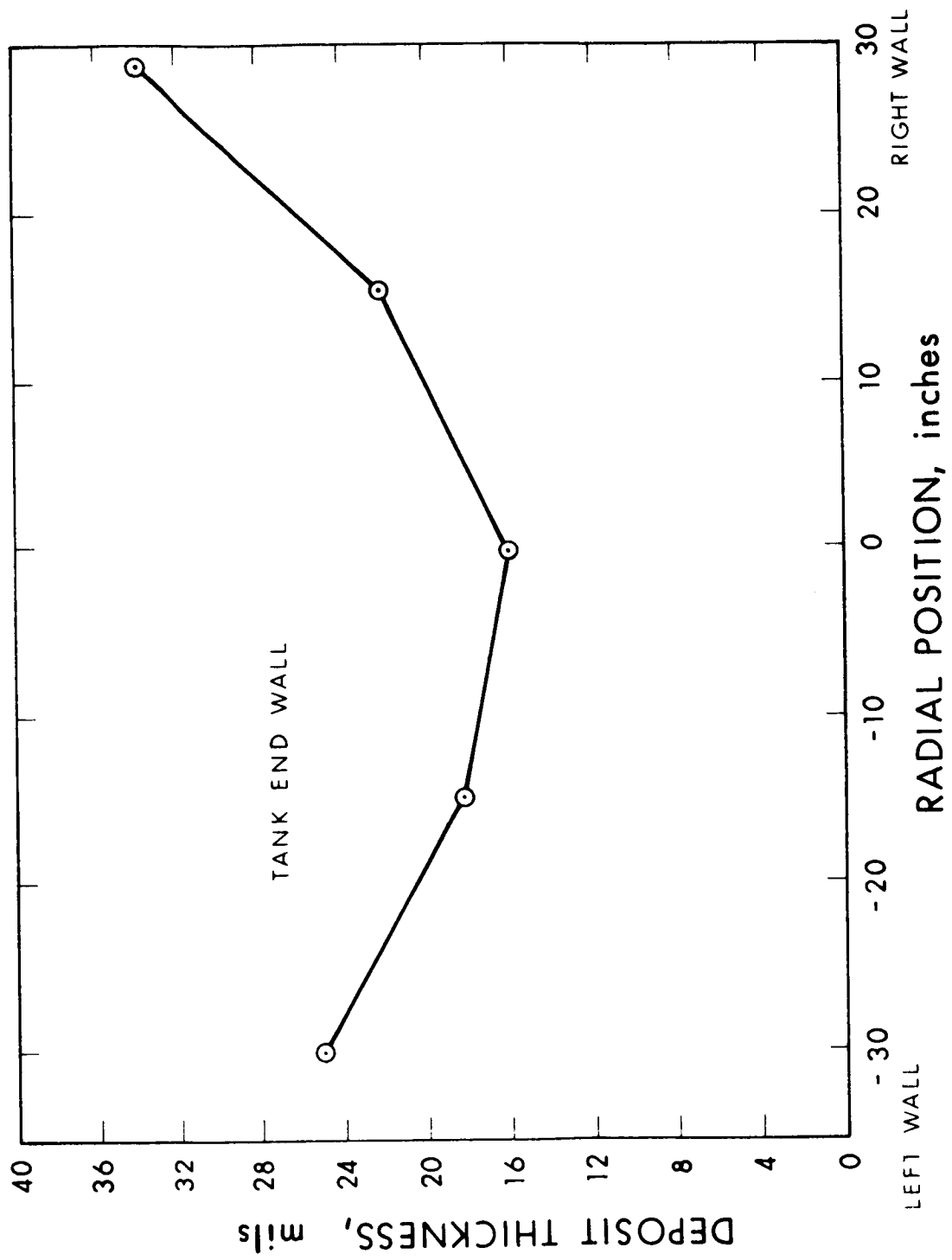
Figure 45c. Measured Deposit Thicknesses

4.7.3 PHOTOMULTIPLIER AND SOLAR CELL EXPERIMENTS

A series of measurements was made using photomultiplier tubes and solar cells to determine the relative alkali metal mass-flux rates at two specific positions on the ALPHA test chamber. The first of these positions, designated A, was at the end of the test chamber opposite, and facing, the exhaust of ALPHA. The center of the window is located in the horizontal midplane of the tank and is at a radial position approximately 2 feet from the horizontal major-centerline of the chamber (i.e., 2 feet out from the center of the end of the 6-foot-diameter tank). The second of the positions, designated B, was located approximately 10 degrees above the horizontal midplane and approximately 2 feet 6 inches from the horizontal major-centerline of the opposite end of the chamber (i.e., the same end as the ALPHA thrustor, with the plasma exhaust pointed away from the window).

The experimental observations, with both photomultipliers and conventional silicon type solar cells, were as follows:

At position A: The output of both the photomultiplier tubes and the solar cells was reduced to 1/2 the initial value in 8 seconds.

At position B: The output of both the photomultiplier tubes and the solar cells was reduced by about 10 percent after the entire duration of a 110 hour test. This included two brief "flooding" periods which accounted for roughly 80 percent of the attenuation.

If we assume the attenuation of the photomultiplier tube and solar cell outputs to be proportional to the local lithium mass-flux, then the mass-flux (Φ_M) ratios are given by:

$$\frac{(\Phi_M)_A}{(\Phi_M)_B} = \frac{(0.50)/(8.0)}{(0.02)/(110 \times 3600)} = 2.5 \times 10^5$$

where we have used the long-time-average value at position B. Clearly, the ratio of alkali metal (viz., lithium) deposition is vastly greater at the end of the tank which is intercepted directly by the plasma than at the end of the tank which is behind (but not shadow shielded) from the ALPHA thrustor. While the above ratio (i.e., 250,000 to 1) may vary somewhat for different run conditions, it seems quite clear that there is very little multiple scattering of alkali metal during an actual laboratory test of the alkali plasma Hall accelerator.

SECTION 5

ANALYSIS

5.1 INTRODUCTION

The primary purpose of the analysis is to correlate the diagnostic
results with engine mechanisms. Some of these analyses have been in-
cluded in the sections with the diagnostic data.

5.2 MECHANISMS

The primary thrust producing mechanism is electromagnetic acceleration
of ions. The ions are formed by collisions between electrons and the
atoms supplied. Both spectroscopic information and power balance data
indicate that there is some second ionization. A magnetic field is
supplied which "traps" the electrons; i.e., their Larmor radius is
small compared to the size of the accelerator. The ions are accelerated
through the magnetic field by the electric field. The electrons drift
in the azimuthal direction causing "Hall" currents. The experimental
data from magnetic field mapping indicates that these interactions
occur in a volume many anode diameters downstream from the anode.
Beam measurements indicate that the particles are well directed.
Velocity measurements have shown that high beam velocities have been
attained.

5.3 TEST CONDITIONS WHICH MAY INVALIDATE CONCLUSIONS

Do tests in an environmental test facility duplicate operation in the
environment of free space? The primary differences are:

a. Background gas density,

b. Presence of tank walls,

c. Gravity.

It has been observed that too high a background density does affect thrust (usually reduces it). One of the primary advantages of tests with alkali metals is their gettering ability which makes additional pumping requirements modest. The higher the alkali flow rate, the lower the impurity background density in the test chamber becomes. The reason that performance diminishes at high background density is that ions lose their energy and momentum to atoms by elastic and charge exchange collisions.

The effect of the tank walls is not completely understood, but much has been learned from the probes. The best information comes from the total beam calorimeter which is like a **large** plate. Pushing the calorimeter toward the accelerator is in many respects like reducing the tank size. It was observed that there was no effect upon performance as long as the calorimeter was more than a meter away.

The only essential component known to depend upon gravity is the feed system, which could easily be modified for zero gravity operation. There is no difficulty expected by very low "g" operation. Thus it seems that the present test facility is adequate to simulate the space environment.

Thus the amount of expellant which is ionized and accelerated need not be the same as that supplied. When too much is supplied in an open configuration such as that studied, the excess is rejected, representing a waste. When too little is supplied and there is a high background density, entrainment and acceleration of ambient gas will occur, thus giving invalid results.

5.4 MINIMUM POTENTIAL TO DETERMINE MASS FLOW RATE

Using the concept of an effective mass flow rate $\dot{m}_e$ which adjusts it-self to minimize the arc potential, some very general relations have been derived. It is found that the curve of η_T versus I_{sp} which had been computed (see Fig. 8-3 of Ref. 30) is valid for all electromagnetic thrust devices, provided the ionization and acceleration processes are intimately related. Following the procedure laid down in Ref. 30, an outline of the analysis is discussed below.

The energy balance equation is written as follows:

$$I V = (1 + n) \dot{m}_e \frac{|e| V_I}{m_a} + n^* I V_I + \frac{T^2}{2 \dot{m}_e} \qquad (1)$$

            ↑   ↑   ↑

Power to ionize   Power loss   Power in kinetic
and heat the   to electrodes. energy of exhaust
expellant.   beam.

where

$\dot{m}_e$ = mass flow rate that is ionized and accelerated

   = effective mass flow rate

$n = \dfrac{\text{internal energy}}{|e| V_I}$

$n^* = \dfrac{\text{power to electrodes}}{I V_I}$

For convenience we next assume that n, n* and T are independent of $\dot{m}_e$. Holding the current constant we can now determine the effective mass flow rate that will minimize the potential. This will be called the critical mass flow rate, $\dot{m}_{cr}$. In nondimensional terms, the critical mass flow rate can be expressed as follows:

$$\frac{|e|\dot{m}_{cr}}{m_a I} = \psi_{cr} = \frac{T/I}{\sqrt{\frac{2 m_a V_I}{|e|}(1 + n)}} \qquad (2)$$

Since $\dot{m}_{cr}$ equipartitions the kinetic energy and internal plus ioniza-
tion energy, a critical velocity exists which can be expressed in the
following form:

$$\frac{w}{w_{cr}(1 + n)^{1/2}} = \frac{I_{sp}}{I_{sp}^{o}(1 + n)^{1/2}} = \frac{\psi_{cr}}{\psi} \qquad (3)$$

where

$$w = \text{mass average exhaust velocity}$$

$$I_{sp}^{o} = \frac{1}{g}\sqrt{\frac{2|e|V_I}{m_a}}$$

$$w_{cr} = \sqrt{\frac{2|e|V_I}{m_a}}$$

When enough mass flow is available either through injection, entrain-
ment or electrode erosion, so that $\dot{m} > \dot{m}_{cr}$, then the efficiency and
arc potential can be written as follows:

Case I $\qquad \psi > \psi_{cr}$

then $\qquad \psi_e = \psi_{cr}$

$$\frac{V}{V_I} = 2(1 + n) \; \psi_{cr} + n* \tag{4}$$

$$\eta_{thrust} = \frac{I_{sp}/\sqrt{1 + n} \; I_{sp}^o}{2 + \dfrac{n*}{1 + n} \; \dfrac{1}{\psi_{cr}}} \tag{5}$$

When the accelerator is operating in this mode, the actual exhaust velocity of the gas is

$$\sqrt{\frac{(1 + n) \; 2 \; |e| \, V_I}{m_a}} \; .$$

In fact, it is not possible for the exhaust jet to have a lower velocity. If more propellant than $\dot{m}_{cr}$ is injected, it is rejected by the discharge.

When the discharge is forced to work with a mass flow rate less than $\dot{m}_{cr}$, then different relations exist for the thrust efficiency and arc voltage.

Case II $\quad \psi \; < \; \psi_{cr}$

then $\psi_e = \psi$

$$\frac{V}{V_I} = \left\{ \frac{I_{sp}}{\sqrt{1 + n} \; I_{sp}^o} + \sqrt{1 + n} \; \frac{I_{sp}^o}{I_{sp}} \right\} (1 + n) \; \psi_{cr} + n* \tag{6}$$

$$\eta_{thrust} = \frac{I_{sp}/\sqrt{1 + n} \; I_{sp}^o}{\dfrac{I_{sp}}{\sqrt{1 + n} \; I_{sp}^o} + \sqrt{1 + n} \; \dfrac{I_{sp}^o}{I_{sp}} + \dfrac{n*}{1 + n} \; \dfrac{1}{\psi_{cr}}} \tag{7}$$

SECTION 6

CONCLUSIONS

The following conclusions are indicated by the experimental results of
this program:

a. The total beam power, measured with a segmented total beam
calorimeter capturing virtually all of the flowing plasma,
agrees quite well with the input electrical power minus the
component cooling losses. Similar results were obtained in
both lithium and sodium plasmas.

b. The energy flux distribution, measured with the local energy
flux probe, was broader for lithium than for sodium. The
power in the beam, determined by numerical integration of
these distributions, also agreed quite closely with the input
electrical power minus the component cooling losses.

c. The position of the segmented total beam calorimeter was found
to have no measurable (i.e., < 1%) effect upon either the in-
dicated thrust or arc voltage whenever the plane of the calo-
rimeter was further than 50 cm from the anode face. At 50 cm,
tiny shifts and/or fluctuations in both thrust and voltage
readings were observed as well as a faint "glow-type" dis-
charge from the central segment to the first or second segment
(radially outward). At less than 50 cm downstream these
effects increased. Due to intense heating of the central
segment, as a result of direct impingement of the cathode jet,
the total beam calorimeter was not kept at positions closer
than 50 cm from the anode for periods of more than a few seconds.

d. Phototracer measurements, at a median position 14 cm downstream
of the anode face indicated velocities about 40 to 50% of the
effective exhaust velocity determined from thrust and mass flow
rate measurements. At a median position of 118 cm the measure-
ments were substantially in agreement with the effective exhaust
velocity, within the accuracy of this technique (viz. about 20%).
These measurements indicate significant acceleration of the
ALPHA exhaust beam in the region external to the electrodes.
Similar results were obtained for both lithium and sodium.

e. The phototracer outputs showed the existence of a number of
characteristic frequencies. The most obvious frequency was
360 Hz (with some 60 and 120 Hz also present). This is be-
lieved to be associated with power supply "ripple." The

second "group" of characteristic frequencies were in the range 10^5 to 3×10^5 Hz, depending upon the applied magnetic field strength. The frequencies were observed regardless of whether the phototracer was pointed at a downstream position (z = 114 cm) or near the anode (z = 14 cm).

f. Spectroscopic Doppler axial velocity measurements in a lithium plasma, with the optical system focused at a region near the exit plane, indicated lithium ion velocities in close agreement (viz. within 10%) of the phototracer results at the same location. This velocity was about half the effective exhaust velocity indicated by the thrust and mass flow rate measurements. A glow-discharge calibration source identified most of the 14 separate lithium ion lines in the wavelength region 5483.345Å to 5485.463Å which have been reported in the literature. However, during actual operation of the ALPHA thrustor, only the three major peaks at (about) 5483.6Å, 5484.5Å, and 5485.1Å could be observed. This is presumably due to the "smearing" of the lines as a result of thermal (random) Doppler broadening. The measured Doppler shifts were in the correct sense (towards the "blue" for a plasma approaching the observer) and were typically of the order of 0.4Å.

g. The three-dimensional Hall-effect magnetic field probe data indicated that significant currents existed at considerable distances downstream of the arc. Specifically, for a test in which the total measured arc current was 200 amperes, 100 amperes of current were still flowing 32 cm (or 16 anode radii) downstream of the anode face.

h. The Hall probe registered a small (i.e., < 8%) but consistent diamagnetic effect. This was determined by measuring the magnetic field within the plasma discharge region and then shutting the arc off and measuring the magnetic field at the same point without plasma present.

i. Characteristic frequencies obtained using a $\partial B_r/\partial t$ loop magnetic probe were in the same range as those observed optically with the phototracer technique. Further the amplitude of the loop probe output signal was about 5 times higher in a pure hydrogen arc than in a lithium-hydrogen arc. Finally, for a lithium-hydrogen arc the frequency of the magnetic probe output was found to vary linearly with the applied magnetic field strength, while the amplitude of the signal showed little or no change with applied magnetic field.

j. The deposition rate of lithium on a window downstream of the ALPHA thrustor was measured and found to be over 200,000 times greater than the deposition rate of lithium on a window on the tank wall which was upstream of the thrustor.

REFERENCES

1. G. L. Cann and G. L. Marlotte, "Hall Current Plasma Accelerator," AIAA Journal, Vol. 2, No. 7, July 1964

2. G. L. Cann and R. L. Harder, "Follow-On Investigation of a Steady State Hall Current Accelerator," NASA-LRC, NAS CR-54062, 30 Oct 1964

3. G. L. Cann, "Annular Magnetic Hall Current Accelerator," AIAA Reprint No. 64-670

4. G. L. Cann, R. A. Moore, R. L. Harder, and P. F. Jacobs, "High Specific Impulse Thermal Arc Jet Thrustor Technology," AFAPL-TR-65-48, Part II, Jan 1967

5. P. F. Jacobs, L. R. Gallagher, and R. W. Prichard, "Diagnostic Measurements in an Alkali Plasma Hall Accelerator," AIAA Report No. 67-46

6. R. R. John, S. Bennett, and R. Connors, "Experimental Performance of a High Specific Impulse Arc Jet Engine," AIAA Reprint No. 64-669

7. R. R. John, S. Bennett, and R. Jahn, "Current Status of Plasma Propulsion," AIAA Reprint No. 66-565

8. S. Bennett, R. R. John, G. Enos, and A. Tuchman, "Experimental Investigation of the MPD Arc Jet," AIAA Reprint No. 66-239

9. W. E. Powers, "Measurements of the Current Density Distribution in the Exhaust of an MPD Arcjet," AIAA Journal, Vol. 5, No. 3, March 1967

10. A. C. Ducati, E. Muehlberger, and G. Giannini, "High Specific Impulse Thermo-Ionic Acceleration," AIAA Reprint No. 64-668

11. W. Grossman, R. V. Hess, and H. A. Hassan, "Experiments with a Coaxial Hall Current Plasma Accelerator," AIAA Reprint No. 64-700

12. P. Brockman, R. Hess, F. Bowen and O. Jarrett, "Diagnostic Studies in a Hall Accelerator at Low Exhaust Pressures", AIAA Journal, Vol. 4, No. 7, July 1966

13. T. F. Stratton, "High Current Steady State Coaxial Plasma Accelerators," AIAA Journal, Vol. 3, No. 10, Oct 1965

14. G. L. Cann, S. T. Nelson, R. L. Harder, and C. B. Shepard, Jr., "High Specific Impulse Thermal Arc Jet Thrustor Technology", AFAPL Contract AF 33(615)-1579, EOS Report 5090-IR-3, Feb 1967

REFERENCES (contd)

15. J. Grey, P. F. Jacobs, and M. P. Sherman, "Calorimetric Probe for the Measurement of Extremely High Temperature," Rev. Scientific Inst., Vol. 33, No. 7, July 1962

16. H. R. Griem, Plasma Spectroscopy, McGraw-Hill, 1964

17. G. Herzberg and H. R. Moore, Can. J. Phys., Vol. 37, 1959, pp 1293-1313

18. H. Schuler, "Uber Feinstrukturen Im Ersten Li-Funkenspektrum," Ann. Physik, Vol. 76, 1925, pp 292-298

19. H. Schuler, "Weitere Untersuchungen Am Ersten Li-Funkenspektrum," Z. Physik, Vol. 42, 1927, pp 487-494

20. C. E. Moore, "A Multiplet Table of Astrophysical Interest," NBS TN-36, Nov 1959

21. C. R. Harrison, R. C. Lord, and J. R. Loofbourow, Practical Spectroscopy, Prentice-Hall, 1948, pp 215-216

22. D. W. Esker, "Comparison of Exhaust Velocity with the Propagation Velocity of Random Light Fluctuations," J. Spacecraft & Rockets, Vol. 4, No. 5, May 1967

23. W. M. Van Camp, D. W. Esker, R. J. Checkley, W. G. Duke, et al., "Study of Arc Jet Propulsion Devices," NASA Report CR-54691, March 1966

24. P. F. Jacobs and G. L. Cann, "Diagnostics of an Alkali Plasma Hall Current Accelerator," NASA-LRC Contract NAS3-8902, EOS Report 7053-SA-1, Sep 1966

25. S. Glasstone and R. H. Lovberg, Controlled Thermonuclear Reactions, Chapter VI, "Plasma Diagnostic Techniques," D. Van Nostrand Co., 1960

26. R. H. Lovberg, "Magnetic Probes," Chapter 3 from Plasma Diagnostic Techniques (edited by R. H. Huddlestone and S. L. Leonard), Academic Press, 1965

27. G. R. Giedd and M. H. Perkins, "Evaporation Rate Monitor," Rev. Sci. Instr., Vol. 31, No. 7, Jul 1960, pp 773-775

28. A. L. Esquivel, A. C. Fung, H. U. Rhoads, and A. H. Weber, "Electron Optical Investigation of Thin Films of Lithium on Tantalum, Platinum and Carbon Substrates," J. Appl. Phys., Vol. 33, No. 8, Aug 1962, pp 2613-2618

REFERENCES (contd)

29. S. Maxman, "Self-Supporting Calcium, Potassium and Lithium Targets," Rev. Sci. Instr., Vol. 35, No. 11, Nov. 1964, pp 1572-1573

30. R. A. Moore, G. L. Cann, and L. R. Gallagher, "High Specific Impulse Thermal Arc Jet Technology," AFAPL-TR-65-48, Part 1, June 1965

31. "Technical Data on Lithium Hydride," Foote Mineral Co., Bulletin 102, Nov 1958

APPENDIX A

AN ANALYSIS OF THE EFFECTS OF LITHIUM-HYDROGEN
REACTION WITHIN AN ENERGY-FLUX PROBE

APPENDIX A

AN ANALYSIS OF THE EFFECTS OF LITHIUM-HYDROGEN REACTION WITHIN AN ENERGY-FLUX PROBE

Schematically:
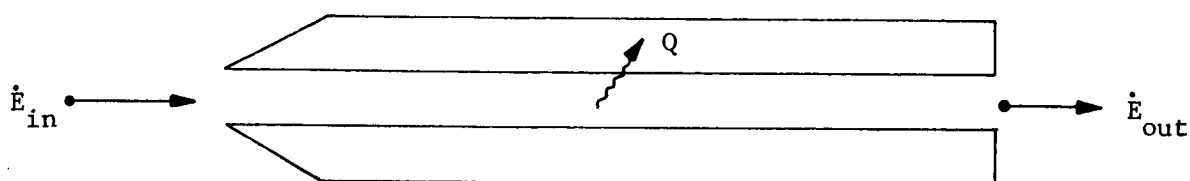
where $\dot{E}_{in} = \{\dot{E}_{Li} + \dot{E}_{H} + \dot{E}_{chem}\}_{in}$

$\dot{E}_{out} = \{\dot{E}_{Li} + \dot{E}_{H} + \dot{E}_{Li-H} + \dot{E}_{chem}\}_{out}$

Q = energy absorbed per unit time by probe coolant

Assumptions:

    a. One dimensional across probe inlet area

    b. Steady

    c. Equilibrium

    d. Common velocity for all species

Let us define the quantity

$$\beta \equiv \frac{\dot{m}_{Li}}{\dot{m}_{H}}$$

This quantity is determined as a test parameter and shall be assumed constant.

The total mass flux entering the probe is given by

$$\dot{m}_{tot} = \int_{A_x} \{m_{Li}N_{Li} + m_H N_H\} U dS$$

where m_{Li} = mass of lithium atom (grams)

  m_H = mass of hydrogen atom (grams)

  N_{Li} = number density of lithium (cm^{-3})

  N_H = number density of hydrogen (cm^{-3})

  U = flow velocity

  dS = element of area

  A_x = cross sectional probe entrance area

Provided these quantities are uniform this becomes

$$\dot{m}_{tot} = \dot{m}_{Li} + \dot{m}_H = \dot{m}_H (1 + \beta)$$

where $\dot{m}_H = m_H N_H U A_x$

  $\dot{m}_{Li} = m_{Li}N_{Li} U A_x$

Hence

$$\beta = \frac{m_{Li}}{m_H} \frac{N_{Li}}{N_H}$$

We now write the basic energy equation

$$\dot{E}_{in} = \dot{E}_{out} + Q$$

where $\dot{E}_{in} = m_{Li}N_{Li}\, U\, A_x\, [h_{Li} + \frac{1}{2}\, U^2]_{in} + m_H N_H\, U\, A_x\, [h_H + \frac{1}{2}\, U^2]_{in}$

$$+ \dot{E}_{chem}$$

$$\dot{E}_{out} = \alpha_{Li}\dot{m}_{Li}\, [h_{Li} + \frac{1}{2}\, U^2]_{out} + \alpha_H \dot{m}_H\, [h_H + \frac{1}{2}\, U^2]_{out}$$

$$+ \gamma_{Li-H}\, \dot{m}_{Li-H}\, [h_{Li-H} + \frac{1}{2}\, U^2]_{out}$$

and

$$\dot{E}_{chem} = \dot{E}_{condensation} + \dot{E}_{reaction}$$

$$= \left\{ (1-\alpha_{Li})\, \dot{m}_{Li} + (1-\gamma) \left[\frac{m_{Li}}{m_{Li} + m_H} \right] \dot{m}_{Li-H} \right\} H_{vap}$$

$$+ (1-\alpha_H)\, \chi\, \dot{m}_H$$

where α_{Li} = fraction of lithium which exits probe

α_H = fraction of hydrogen which exits probe

γ = fraction of Li-H which exits probe

H_{vap} = heat of vaporization of lithium (cal/gm)

χ = heat of formation of lithium-hydride (cal/gm)

Define

$$\xi \equiv \frac{\dot{E}_{chem}}{Q}$$

Thus, ξ is a measure of the importance of energy release due to chemistry within the probe.

It can be shown from simple algebra that

$$\zeta \;=\; \frac{1}{1 + y - p} \qquad\qquad y \;\equiv\; \frac{\dot{E}_{in} - \dot{E}_{chem}}{\dot{E}_{chem}}$$

$$y \;\equiv\; \frac{\dot{m}_{Li}\,[h_{Li} + \tfrac{1}{2}\,U^2] + \dot{m}_{H}\,[h_{H} + \tfrac{1}{2}\,U^2]}{\left\{ (1-\alpha_{Li})\,\dot{m}_{Li} + (1-\gamma)\left[\dfrac{m_{Li}}{m_{Li} + m_{H}}\right]\dot{m}_{Li-H} \right\} H_{vap} + (1-\alpha_{Li})\,\dot{m}_{H}\,\chi}$$

$$p \;\equiv\; \frac{\left\{ \alpha_{Li}\dot{m}_{Li}\,[h_{Li} + \tfrac{1}{2}\,U^2]_{out} + \alpha_{H}\dot{m}_{H}\,[h_{H} + \tfrac{1}{2}\,U^2]_{out} + \gamma\dot{m}_{Li-H}\,[h_{Li-H} + \tfrac{1}{2}\,U^2]_{out} \right\}}{\left\{ (1-\alpha_{Li})\,\dot{m}_{Li} + (1-\gamma)\left[\dfrac{m_{Li}}{m_{Li} + m_{H}}\right]\dot{m}_{Li-H} \right\} H_{vap} + (1-\alpha_{Li})\,\dot{m}_{H}\,\chi}$$

From physical experience it is known that the quantity $\dot{E}_{out}/\dot{E}_{in} \ll 1$. This corresponds to $p \ll y$ and

$$\alpha_{Li} \approx 0 \qquad (1-\alpha_{Li}) \approx 1$$

$$\alpha_{H} \approx 0 \qquad (1-\alpha_{H}) \approx 1$$

$$\gamma \approx 0$$

$$[h_{Li-H} + \tfrac{1}{2}\,U^2]_{out} \approx [h_{Li} + \tfrac{1}{2}\,U^2]_{out} \approx [h_{H} + \tfrac{1}{2}\,U^2]_{out} \ll [h_{H} + \tfrac{1}{2}\,U^2]_{in}$$

In this case

$$\zeta \;\simeq\; \frac{1}{1 + y}$$

and

$$y \;\simeq\; \frac{\dot{m}_{Li}\,[h_{Li} + \tfrac{1}{2}\,U^2] + \dot{m}_{H}\,[h_{H} + \tfrac{1}{2}\,U^2]}{\dot{m}_{Li}\,H_{vap} + \dot{m}_{H}\,\chi}$$

We shall also assume

$$[h_{Li} + \frac{1}{2} U^2] \approx [h_H + \frac{1}{2} U^2] = h + \frac{1}{2} U^2$$

This follows from the fact that the quantity

$$\frac{U^2}{2h} = \frac{\gamma-1}{2} M^2 \gg 1$$

Hence

$$y \simeq \frac{\dot{m}_{Li} + \dot{m}_H}{\dot{m}_{Li}} \left[\frac{h + \frac{1}{2} U^2}{H_{vap} + \frac{\dot{m}_H}{\dot{m}_{Li}} \chi} \right]$$

or

$$y \simeq (\beta+1) \left[\frac{h + \frac{1}{2} U^2}{\chi + \beta H_{vap}} \right]$$

We may note that this equation assumes (quite conservatively)

    a. All the lithium entering the probe condenses

    b. All the hydrogen entering the probe reacts with lithium

Clearly, this gives the upper limit of the lithium-hydrogen reaction energy. Hence $\dot{E}_{chem} = (\dot{E}_{chem})_{max}$, $y = y_{min}$ and $\xi = \xi_{max}$.

NUMERICAL ESTIMATES

From experiment $U \simeq 5 \times 10^4$ m/sec $= 5 \times 10^6$ cm/sec^2; thus $1/2 \ U^2 = 1/2 \times 25 \times 10^{12} = 12.5 \times 10^{12}$ cm^2/sec^2.

Before estimating chemical energies, we note the following

$$1 \text{ calorie } = 4.18 \text{ joule}$$
$$1 \text{ joule } = 10^7 \text{ erg}$$

Hence

$$1 \text{ kilocalorie } = 4.18 \times 10^{10} \text{ erg}$$

and

$$\frac{1 \text{ kilocalorie}}{\text{gram}} = 4.18 \times 10^{10} \frac{cm^2}{sec^2}$$

Since chemical data are generally given in kcal/mole it is convenient to write

$$\frac{kcal}{gram} = \frac{kcal}{mole} \times \frac{moles}{gram} = \frac{kcal/mole}{M}$$

where M = molecular weight

Hence an enthalpy/mole, H, becomes

$$\frac{H \ (kcal/mole)}{M} \times 4.18 \times 10^{10} = (\quad) \frac{cm^2}{sec^2}$$

Now, for lithium at 8000°K

$$h_{Li} = 57 \text{ kcal/mole}$$

$$= 57/7 \times 4.18 \times 10^{10}$$

$$h_{Li} = 0.34 \times 10^{12} \text{ cm}^2/\text{sec}^2$$

Clearly $1/2 \, U^2 \gg h$ (high Mach number limit) (i.e., $40 \gg 1$)

From the technical data by Foote — Bulletin 102 (Ref. 31) on lithium hydride, we note $M_{LiH} = 8$

Heat of Sublimation $= 41.7$ **kcal**/mole (analogous to H_{vap})

Heat of Formation $= 21.6$ kcal/mole (i.e., heat given up upon formation of the crystal)

Heat of Dissociation $= 59$ kcal/mole (i.e., heat liberated when hydrogen and lithium recombine)

Hence we may use

$$\beta \approx 10 \; \{\text{actual case; } \dot{m}_{Li} \approx 10 \text{ mg/sec}, \; \dot{m}_H \approx 1 \text{ mg/sec}\}$$

$$H_{vap} = H_{sublimation} = 41.7 \text{ kcal/mole}$$

$$= \frac{41.7}{(7+1)} \times 4.18 \times 10^{10} = 0.22 \times 10^{12} \text{ cm}^2/\text{sec}^2$$

$$\chi = H_F - H_{diss} = 21.6 \frac{\text{kcal}}{\text{mole LiH}} + 59 \frac{\text{kcal}}{\text{mole H}}$$

$$= \frac{21.6 \times 4.18 \times 10^{10}}{(7+1)} + \frac{59 \times 4.18 \times 10^{10}}{(1)} \quad \frac{\text{cm}^2}{\text{sec}^2}$$

$$= 2.58 \times 10^{12} \text{ cm}^2/\text{sec}^2$$

Thus,

$$y = (10 + 1) \left[\frac{(0.34 + 12.5) \times 10^{12} \text{ cm}^2/\text{sec}^2}{(2.58 + (10)(0.22)) \times 10^{12} \text{ cm}^2/\text{sec}^2} \right]$$

$$= 11 \left[\frac{12.84}{4.78} \right]$$

or

$$y = 29.5$$

and

$$\xi = \frac{\dot{E}_{chem}}{Q} = \frac{1}{1 + 29.5} = 0.033$$

So that the effect of the chemical reaction is less than 4%.

This result may be achieved very simply by noting that to close approximation

$$y \equiv \frac{E_{in} - E_{chem}}{E_{chem}} \approx \frac{\frac{1}{2} m_{Li} U^2}{m_H \chi}$$

Since $1/2 \, m_{Li} \, U^2$ is the dominant term in the numerator while $m_H \chi$ is the dominant term in the denominator.

From experiment $1/2 \, m_{Li} \, U^2 \approx 60$ eV and $m_H \chi \approx 2$ eV ---- so that $y \approx 30$.

APPENDIX B
ALPHA PERFORMANCE DATA

TABLE B-I
SUMMARY OF TESTS CONDUCTED

Run Number	Date	Elapsed Time (hrs/min)	Configuration	Propellant	Chamber	Feed System
			Buffer Configuration Test			
702	3-22-66	3:41	LAJ-AF-BG-1A	Li/N$_2$	6 x 6	Bellows
			Magnet Configuration Tests			
703	3-28-66	--	LAJ-AF-CG-1	Li/N$_2$	6 x 6	Bellows
704	3-31-66	1:25	LAJ-AF-CG-1	Li/N$_2$	6 x 6	Bellows
705	4-11-66	3:00	LAJ-AF-CG-1B	Li/N$_2$	6 x 6	Bellows
706	4-19-66	--	LAJ-AF-CG-1C	Li/H$_2$, Li/N$_2$	6 x 6	Bellows
707	4-26-66	2:08	LAJ-AF-CG-1C	Li/H$_2$, Li/N$_2$	6 x 6	Bellows
708	5-6-66	4:17	LAJ-AF-CG-1C	Li/H$_2$,	6 x 6	Bellows
709	5-9-66	3:05	LAJ-AF-CG-1D	Li/H$_2$	6 x 6	Bellows
710	5-12-66	:38	LAJ-AF-CG-1D	Li/H$_2$	6 x 6	Bellows
			Endurance Tests			
711	6-30-66	:09	LAJ-AF-CG-1D	Li	6 x 14	Bellows
712	7-1-66	--	LAJ-AF-CG-1D	Li	6 x 14	Bellows
713	7-6-66	--	LAJ-AF-CG-1D	Li	6 x 14	Bellows
714	7-7-66	1:24	LAJ-AF-CG-1D	Li/H$_2$	6 x 14	Bellows
715	7-8-66	:28	LAJ-AF-CG-1D	Li/H$_2$	6 x 14	Bellows
716	7-8-66	4:13	LAJ-AF-CG-1D	Li/H$_2$	6 x 14	Bellows
717	7-9-66	2:15	LAJ-AF-CG-1D	Li/H$_2$	6 x 14	Bellows
718	7-12-66	2:58	LAJ-AF-CG-1D	Li/H$_2$	6 x 14	Bellows

TABLE B-I
SUMMARY OF TESTS CONDUCTED (contd)

Run Number	Date	Elapsed Time (hrs/min)	Configuration	Propellant	Chamber	Feed System
			Endurance Tests (contd)			
719	7-13-66	:54	LAJ-AF-CG-1D	Li/H_2	6 x 14	Bellows
720	7-14-66	9:16	LAJ-AF-CG-1D	Li/H_2	6 x 14	Bellows
721	7-15-66	4:50	LAJ-AF-CG-1D	Li/H_2	6 x 14	Bellows
722	7-20-66	1:15	LAJ-AF-CG-1D	Li/H_2	6 x 14	Bellows
723	7-28-66	9:04	LAJ-AF-CG-1D	Li/H_2	6 x 14	Bellows
724	8-8-66	6:47	LAJ-AF-CG-1D	Li/H_2	6 x 14	Bellows
725	8-23-66	1:46	LAJ-AF-CG-2A	Li/H_2	6 x 14	GAF-II-1
726	8-25-66	--	LAJ-AF-CG-2A	Li/H_2	6 x 14	GAF-II-1
727	9-28-66	30:05	LAJ-AF-CG-2A	Li/H_2	6 x 14	GAF-II-1
			Calibration Tests			
728A	10-19-66	6:26	LAJ-AF-CG-2A	Li/H_2	3 x 6	GAF-II-2
728B	10-20-66	11:15	LAJ-AF-CG-2A	Li/H_2	3 x 6	GAF-II-2
728C	10-21-66	5:57	LAJ-AF-CG-2A	Li/H_2	3 x 6	GAF-II-2
728D	11-2-66	5:35	LAJ-AF-CG-2A	Li/H_2	3 x 6	GAF-II-2
728E	11-9-66	4:20	LAJ-AF-CG-2A	Li/H_2	3 x 6	GAF-II-2
728F	11-11-66	5:20	LAJ-AF-CG-2A	Li/H_2	6 x 6	GAF-II-2
728G	11-15-66	3:20	LAJ-AF-CG-2A	Li/H_2	3 x 6	GAF-II-2
			Ammonia Tests			
729	12-16-66	:20	NH_3AJ-AF-CG-2A	NH_3	6 x 14	Ammonia Feed
730	12-23-66	:54	NH_3AJ-AF-CG-2A	NH_3	6 x 14	Ammonia Feed

TABLE B-I
SUMMARY OF TESTS CONDUCTED (contd)

Run Number	Date	Elapsed Time (hrs/min)	Configuration	Propellant	Chamber	Feed System
			Three Magnet Configuration Tests			
501	12-9-66	1:00	LAJ-AF-CG-2A	Li/H_2	6 x 14	GAF-II-2A
502	12-21-66	5:59	LAJ-AF-CG-2A	Li/H_2	6 x 14	GAF-III-2
731	12-28-66	4:57	LAJ-AF-CG-2A	Li/H_2	6 x 14	GAF-IV-1
			Performance and Life Tests			
732	1-4-67	111:26	LAJ-AF-CG-2B	Li/H_2	6 x 14	GAF-IV-1
733	1-30-67	7:40	LAJ-AF-CG-2B	Li/H_2	6 x 14	GAF-IVA-2
734	2-1-67	3:01	LAJ-AF-CG-2B	Li/H_2	6 x 14	GAF-IVA-2
735	2-8-67	2:23	LAJ-AF-CG-2B	Li/H_2	6 x 14	GAF-IV-2
736	2-15-67	7:24	LAJ-AF-CG-2C	Li/H_2	6 x 14	GAF-V-2
737	3-2-67	:54	LAJ-AF-CG-2D	Li/H_2	6 x 14	GAF-V-2
738	3-7-67	5:52	LAJ-AF-CG-2D	Li/H_2	6 x 14	GAF-V-2
739	3-27-67	:30	LAJ-AF-CG-2D	Li/H_2	6 x 14	GAF-VI-3
740	3-31-67	8:31	LAJ-AF-CG-2D	Li/H_2	6 x 14	GAF-VIA-3
741	4-7-67	1:03	LAJ-AF-CG-2D	Li/H_2	6 x 14	GAF-VIA-3
742	4-9-67	6:32	LAJ-AF-CG-2D	Li/H_2	6 x 14	GAF-VIA-3
			Sodium Tests			
503	4-19-67	5:20	NaAJ-AF-CG-2D	Na/H_2	6 x 14	GAF-VIB-2
504	5-1-67	5:25	NaAJ-AF-CG-2D	Na/H_2	6 x 14	GAF-VIB-2

TABLE B-II

TEST RESULTS

Run No.	Point No.	I_A amps	V_A volts	P_A kW	I_C amps	$\dot{m}$ mg/sec	P_t torr	P_{ca} kW	P_{an} kW	T grams	I_{sp} sec	η_o
702	2A	168	47	7.90	400	18.4	1.6×10^{-4}	1.83	2.45	14.25	770	0.067
	2B	168	47	7.90	450	18.4	1.6×10^{-4}	1.83	2.45	15.0	815	0.067
	2C	168	47	7.90	500	18.4	1.6×10^{-4}	1.83	2.45	16.1	870	0.067
	3	168	50	8.40	500	18.4	1.4×10^{-4}	1.70	2.49	15.9	860	0.079
	4	168	50	8.40	600	18.4	1.4×10^{-4}	1.70	2.40	17.4	950	0.094
	5	163	54	8.80	800	18.4	1.4×10^{-4}	1.73	2.47	18.6	1010	0.103
	6	250	56	14.00	800	18.4	1.2×10^{-4}	1.83	2.71	27.4	1490	0.140
	7A	300	53	15.75	800	18.4	1.3×10^{-4}	1.95	3.54	32.3	1760	0.173
	7B	300	40	12.00	800	18.4	1.3×10^{-4}	1.95	3.54	25.5	1390	0.141
	8A	300	41	12.15	800	18.4	1.4×10^{-4}	2.10	3.53	25.5	1390	0.140
	8B	300	41	12.15	700	18.4	1.4×10^{-4}	2.10	3.53	23.6	1280	0.140
	8C	300	41	12.15	600	18.4	1.4×10^{-4}	2.10	3.53	21.4	1160	0.140
	8D	300	41	12.15	500	18.4	1.4×10^{-4}	2.10	3.53	19.5	1060	0.140
	9A	300	33	9.75	400	18.4	1.4×10^{-4}	2.12	3.53	19.2	1040	0.099
	9B	300	35	10.50	500	18.4	1.4×10^{-4}	2.12	3.53	21.8	1180	0.118
	9C	300	37	11.10	600	18.4	1.4×10^{-4}	2.12	3.53	22.8	1240	0.122
	9D	300	39	11.55	700	18.4	1.4×10^{-4}	2.12	3.53	24.2	1320	0.132
	9E	300	40	12.00	800	18.4	1.4×10^{-4}	2.12	3.53	25.5	1390	0.141

Thrustor Model: LAJ-AF-BG-1A
Propellant: Lithium/Nitrogen
Test Chamber: 6' x 6'

TABLE B-II

TEST RESULTS (contd)

Run No.	Point No.	I_A amps	V_A volts	P_A kW	I_C amps	ṁ mg/sec	P_t torr	P_{ca} kW	P_{an} kW	T grams	I_{sp} sec	η_o
702	10	350	41	14.35	800	18.4	1.0×10^{-4}	2.17	3.89	30.8	1670	0.172
	12	350	39	13.65	800	12.2	1.2×10^{-4}	2.22	5.01	25.8	2110	0.192
	13	300	39	11.70	800	12.2	1.1×10^{-4}	2.00	4.55	24.8	2030	0.207
	14	250	39	9.75	800	12.2	1.0×10^{-4}	1.58	3.61	22.0	1800	0.195
	15A	200	39	7.70	800	12.2	1.0×10^{-4}	1.43	3.22	20.4	1670	0.213
	15B	168	39	6.47	800	12.2	1.0×10^{-4}	1.43	3.22	17.0	1400	0.176
	15C	168	32	5.38	700	12.2	1.0×10^{-4}	1.43	3.22	15.5	1270	0.176
	15D	168	31	5.21	600	12.2	1.0×10^{-4}	1.43	3.22	15.0	1230	0.170
	15E	168	35	5.88	500	12.2	1.0×10^{-4}	1.43	3.22	14.4	1180	0.139
	15F	168	33	5.46	400	12.2	1.0×10^{-4}	1.43	3.22	13.0	1070	0.122
	15G	168	32	5.38	400	12.2	1.0×10^{-4}	1.43	3.22	12.0	980	0.105
	27A	355	38	13.50	800	8.3	0.8×10^{-4}	1.68	4.01	26.4	3180	0.299
	27B	350	38	13.30	800	8.3	0.5×10^{-4}	1.68	4.01	26.4	3180	0.303
704	1	300	59	17.7	1200	39.5	2.4×10^{-4}	1.62	1.97	52.4	1315	0.185
	3	350	58	19.9	1200	31.7	2.8×10^{-4}	1.80	1.80	61.6	1940	0.285
	4	348	58	20.0	1200	29.0	2.8×10^{-4}	1.75	1.80	61.4	2120	0.312
	5	400	53	21.2	1200	29.0	1.4×10^{-4}	1.85	2.01	66.0	2280	0.340
	6	400	56	22.2	1200	19.65	0.7×10^{-4}	2.02	2.09	62.6	3190	0.432
	7	400	56	22.3	1200	19.65	0.5×10^{-4}	1.92	1.99	67.2	3420	0.495
705	4	300	37	11.10	800	19.65	0.9×10^{-4}	2.47	3.93	33.85	1722	0.185
	6	300	29	8.70	1200	19.65	2.0×10^{-4}	2.35	3.12	45.00	2290	0.325
	7	300	27	8.10	1200	19.35	1.8×10^{-4}	2.25	2.46	46.91	2420	0.350

704
Thrustor Model: IAJ-AF-CG-1
Propellant: Lithium/Nitrogen
Test Chamber: 6' x 6'

705
Thrustor Model: AF-CG-1B
Propellant: Lithium/Nitrogen
Test Chamber: 6' x 6'

7053-Final

141

TABLE B-II

TEST RESULTS (contd)

Run No.	Point No.	I_A amps	V_A volts	P_A kW	I_C amps	$\dot{m}$ mg/sec	P_t torr	P_{ca} kW	P_{an} kW	T grams	I_{sp} sec	η_o
705	8	300	25	7.50	1200	19.35	1.8×10^{-4}	2.33	2.34	45.61	2360	0.339
	9	350	26	9.10	1200	19.35	1.5×10^{-4}	2.30	2.72	44.77	2310	0.345
	10	350	28	9.80	1200	19.05	1.2×10^{-4}	2.60	3.36	44.30	2320	0.316
	11	350	33	11.55	1200	12.3	0.6×10^{-4}	3.02	4.04	38.70	3145	0.343
	12A	350	36	12.60	1200	12.5	1.8×10^{-4}	3.51	4.20	40.1	3200	0.342
	12B	350	36	12.60	1200	12.5	1.8×10^{-4}	3.51	4.20	39.8	3180	—
	13	350	35	12.25	1200	12.5	2.8×10^{-4}	—	—	43.6	3480	—
	14	350	36	12.60	1200	12.5	4.0×10^{-4}	—	—	47.4	3792	—
	15	350	36	12.60	1200	12.5	5.0×10^{-4}	—	—	49.8	3984	—
	16	350	34	11.90	1200	12.5	5.6×10^{-4}	—	—	48.6	3888	—
	17	350	33	11.55	1200	12.5	6.4×10^{-4}	—	—	51.1	4088	—
	18	350	32	11.20	1200	12.5	—	—	—	52.4	4192	—
	19	350	31	10.85	1200	12.5	—	—	—	54.9	4392	—
	20	350	28	9.80	1200	12.5	—	—	—	60.5	4840	—
	22	350	25	8.75	1200	12.5	—	—	—	69.9	5592	—
	23	350	17	5.95	1200	12.5	—	—	—	63.6	5088	—
	24	350	19	6.65	1200	12.5	—	—	—	63.0	5040	—
	25	350	30	10.50	1200	10.3	—	3.34	3.80	35.8	3480	0.374
	26	350	34	11.90	1200	10.3	4.4×10^{-5}	3.64	4.08	39.0	3780	0.378
	27	350	40	14.00	1200	10.3	4.2×10^{-5}	3.66	4.00	39.6	3840	0.396
	28	400	38	15.20	1200	10.3	5.8×10^{-5}	4.50	4.80	38.6	3750	0.334

Run No.	Point No.	I_A amps	V_A volts	P_A kW	I_C amps	$\dot{m}$ mg/sec	P_t torr	P_{ca} kW	P_{an} kW	T grams	I_{sp} sec	η_o —
705	29	400	34	13.60	1000	10.3	3.0×10^{-5}	4.28	4.85	38.8	3760	0.370
	30	400	28	11.20	800	10.3	2.0×10^{-5}	4.55	3.09	35.2	3420	0.340
	31	400	22	8.80	600	10.3	2.0×10^{-5}	3.83	2.60	30.2	2420	0.244
707	2	136	93	12.6	1200	20.5	5.4×10^{-4}	2.72	2.42	40.9	2000	0.318
	3	220	86	18.9	1200	20.5	3.6×10^{-4}	3.08	3.25	40.8	1990	0.210
	4	220	97.5	21.5	1200	14.5	0.8×10^{-4}	3.60	3.57	47.1	3250	0.349
	5	240	100	24.0	1200	14.5	0.8×10^{-4}	3.95	3.85	55.6	3830	0.435
	6	250	102	25.5	1200	14.5	0.5×10^{-4}	3.76	4.22	60.0	4140	0.477
	7	250	107	26.8	1200	11.45	1.1×10^{-4}	2.96	2.63	62.0	5410	0.613
	8	250	102	25.5	1200	11.45	1.5×10^{-4}	—	—	66.5	5810	0.742
	9	258	100	25.8	1200	11.45	2.4×10^{-4}	—	—	67.1	5860	0.747
	10	256	102	26.1	1200	11.45	2.9×10^{-4}	—	—	60.5	5280	0.600
	11	258	94	24.3	1200	11.45	3.6×10^{-4}	—	—	56.6	4940	0.564
	12	254	92	23.4	1200	11.8	5.0×10^{-4}	—	—	55.6	4710	0.548
	13	250	98	24.5	1200	11.45	2.0×10^{-4}	—	—	57.0	4980	0.568
	14	252	92	23.2	1200	11.45	1.0×10^{-4}	2.88	2.88	59.7	5210	0.657
	15	250	102	25.5	1200	11.45	1.0×10^{-4}	3.49	3.49	60.4	5280	0.613
	16	195	93.0	18.1	1200	11.45	1.2×10^{-4}	2.64	2.64	46.5	4060	0.511
	17	204	82.5	16.8	1200	11.45	1.3×10^{-4}	2.36	2.36	46.4	4050	0.548

Thrustor Model: CG-1C
Propellant: Li/N_2 pts. 2-6, Li/H_2 pts. 7-17
Test Chamber: 6' x 6'

TABLE B-II

TEST RESULTS (contd)

Run No.	Point No.	I_A amps	V_A volts	P_A kW	I_C amps	$\dot{m}$ mg/sec	P_t torr	P_{ca} kW	P_{an} kW	T grams	I_{sp} sec	η_o
708	1	104	86.5	9.0	1200	38.5	—	1.85	3.05	—	—	—
	2	241	90	21.4	1200	11.84	3×10^{-4}	2.40	1.89	—	—	—
	3	252	62.5	15.8	400	11.36	2×10^{-4}	2.43	2.08	35.3	3100	0.332
	4	280	72	20.2	500	11.36	1.4×10^{-4}	2.62	2.72	45.9	4040	0.441
	5	280	80	22.4	600	11.36	1.2×10^{-4}	2.80	2.49	50.7	4460	0.485
	6	280	72	20.4	600	11.36	0.9×10^{-4}	2.53	2.71	50.8	4470	0.534
	7	280	74	20.7	600	11.36	1.0×10^{-4}	2.72	2.77	50.7	4460	0.524
	8	280	72.5	20.5	600	11.36	1.0×10^{-4}	2.57	2.64	51.2	4510	0.541
	9	280	75	21.0	600	11.36	1.0×10^{-4}	2.61	2.64	50.3	4430	0.509
	10	279	75	20.9	600	11.36	1.0×10^{-4}	2.66	2.64	47.6	4190	0.458
	11	279	75	20.9	600	11.36	0.9×10^{-4}	2.50	2.54	46.1	4060	0.430
	12	282	78	22.0	600	11.36	1.0×10^{-4}	2.77	2.92	51.6	4540	0.511
	13	282	74	20.9	600	11.36	0.9×10^{-4}	2.62	2.72	51.6	4540	0.538
	14	282	75	20.6	600	11.36	1.2×10^{-4}	2.57	2.61	51.1	4500	0.536
	15	278	78	21.7	600	11.36	1.0×10^{-4}	2.69	2.73	49.8	4380	0.482
	16	280	76	21.3	600	11.36	1.0×10^{-4}	2.63	2.63	50.7	4460	0.510
	17	282	75	21.2	600	11.36	1.2×10^{-4}	2.61	2.61	49.9	4390	0.496
	18	282	76	21.4	600	11.36	1.2×10^{-4}	2.72	2.83	50.4	4440	0.502
	19	282	78	22.0	600	11.30	1.2×10^{-4}	2.83	2.99	51.7	4580	0.517
	20	280	82	23.0	600	11.30	1.2×10^{-4}	3.02	3.09	50.2	4440	0.465
	21	276	88	24.3	600	11.30	1.2×10^{-4}	2.58	2.80	48.1	4260	0.405
	22	280	79	22.1	600	11.30	0.9×10^{-4}	2.62	2.82	47.4	4190	0.431

Thrustor Model: CG-1C
Propellant: Li/H$_2$
Test Chamber: 6' x 6'

TABLE B-II

TEST RESULTS (contd)

Run No.	Point No.	I_A amps	V_A volts	P_A kW	I_C amps	$\dot{m}$ mg/sec	P_t torr	P_{ca} kW	P_{an} kW	T grams	I_{sp} sec	η_o
708	23	284	75	21.3	600	11.30	1.0×10^{-4}	2.74	2.92	50.1	4430	0.500
	24	282	77	21.7	600	11.30	1.1×10^{-4}	2.84	3.00	49.6	4390	0.482
	25	280	79	22.1	600	11.30	1.1×10^{-4}	2.98	3.05	49.6	4390	0.473
	26	276	84	23.2	600	11.30	1.4×10^{-4}	3.02	2.77	49.6	4390	0.451
	27	282	79	22.3	600	11.30	1.0×10^{-4}	2.65	2.86	48.9	4330	0.456
	28	282	78	22.0	600	11.30	1.2×10^{-4}	2.77	2.90	51.3	4540	0.508
	29	282	76.5	21.6	600	11.30	1.0×10^{-4}	2.77	2.89	51.3	4540	0.518
	30	281	76.5	21.5	600	11.30	1.2×10^{-4}	2.62	2.80	50.9	4500	0.511
	31	282	78.5	22.1	600	11.30	1.1×10^{-4}	3.03	3.09	51.7	4580	0.515
	32	286	73	20.9	600	11.30	2.3×10^{-4}	2.84	3.09	—	—	—
	33	280	70	19.6	600	11.30	2.4×10^{-4}	2.50	2.77	—	—	—
	34	280	68	19.0	600	11.30	4.6×10^{-4}	2.50	3.06	—	—	—
	35	280	69.5	19.5	600	11.30	4.4×10^{-4}	2.43	2.92	40.3	3570	0.354
710	1A	300	80	24.0	600	11.45	3.7×10^{-4}	3.42	3.49	41.2	3600	0.165
	1B	300	80	24.0	600	11.45	3.7×10^{-4}	3.42	3.49	43.7	3820	0.186
	2	300	60	18.0	350	11.45	0.7×10^{-4}	3.05	2.70	45.2	3950	0.350
	3A	300	58	17.4	300	11.45	4.2×10^{-4}	3.05	2.70	40.3	3520	0.310
	3B	300	58	17.4	300	11.45	4.2×10^{-4}	3.05	2.70	38.8	3400	0.287
	4	300	57	17.1	350	11.45	4.8×10^{-4}	2.96	2.53	39.7	3470	0.282

Thrustor Model: AF-CG-1D
Propellant: Li/H_2
Test Chamber: 6' x 6'

TABLE B-II

TEST RESULTS (contd)

Run No.	Point No.	I_A amps	V_A volts	P_A kW	$\dot{m}$ mg/sec	p_t torr	P_{C+B} kW	P_{an} kW	P_{mag} kW	T grams	I_{sp} sec	η_o
716	1	200	160	32.00	—	—	1.29	8.85	5.60	—	—	—
	2	350	72	25.20	11.25	3.4×10^{-4}	3.81	3.21	5.56	30.12	2680	0.126
	3	345	69	23.81	10.92	5.0×10^{-5}	3.72	4.29	5.63	40.50	3700	0.244
	4	350	61.5	21.53	11.00	2.6×10^{-5}	3.90	3.69	4.86	41.37	3760	0.283
	5	350	58	20.30	11.00	3×10^{-5}	3.52	2.86	4.92	47.00	4270	0.382
	6	350	59	20.65	11.00	2.4×10^{-5}	3.75	3.03	4.86	46.50	4220	0.295
	7	375	58.5	21.94	11.12	3×10^{-5}	4.21	3.27	4.86	39.62	3560	0.253
	8	400	57.5	23.00	11.12	3×10^{-5}	4.27	3.52	4.58	42.50	3820	0.282
	9	400	57	22.80	11.12	2.4×10^{-5}	4.26	3.42	4.58	43.50	3910	0.298
	10	400	56	22.40	11.12	2.4×10^{-5}	3.82	2.98	4.58	50.75	4560	0.411
	11	400	58	23.20	11.12	2.4×10^{-5}	4.29	3.45	4.55	50.62	4550	0.271
	12	395	58	22.91	11.12	2.4×10^{-5}	4.34	3.50	4.55	46.00	4130	0.290
	13	395	56	22.12	11.12	2.2×10^{-5}	4.25	3.32	4.52	52.75	4740	0.450
	14	395	56	22.12	11.12	2.4×10^{-5}	3.98	2.86	4.50	51.75	4650	0.384
	15	395	56	22.12	11.12	2.6×10^{-5}	4.21	2.98	4.42	41.37	3720	0.278
	16	395	58.5	23.11	11.12	2.2×10^{-5}	4.37	3.53	4.52	42.00	3770	0.275
	17	420	56.5	23.73	11.12	2.8×10^{-5}	4.66	4.03	4.42	41.75	3750	0.267
	18	375	55	20.63	11.12	1.8×10^{-5}	3.63	3.07	4.55	49.25	4420	0.415
	19	350	57.5	20.13	11.12	2.3×10^{-5}	3.07	2.66	4.58	38.25	3440	0.256
	20	350	58	20.30	11.12	2.7×10^{-5}	3.20	2.76	4.72	43.87	3940	0.332
	21	350	58	20.30	11.12	2.3×10^{-5}	3.23	2.78	4.72	44.00	3950	0.334

TABLE B-II
TEST RESULTS (contd)

Run No.	Point No.	I_A amps	V_A volts	P_A kW	$\dot{m}$ mg/sec	P_t torr	P_{C+B} kW	P_{an} kW	P_{mag} kW	T grams	I_{sp} sec	η_o
716	22	350	58	20.30	11.12	2.5×10^{-5}	3.22	2.78	4.86	44.12	3960	0.333
	23	325	58	18.85	11.12	2.6×10^{-5}	3.13	2.69	4.92	39.62	3560	0.285
	24	300	61	18.30	11.12	3.4×10^{-5}	3.04	2.65	4.92	38.25	3440	0.272
718	1	350	63	22.05	7.91	1.0×10^{-4}	3.68	4.86	4.86	31.87	4029	0.229
	2	350	63.5	22.23	6.86	7.2×10^{-5}	3.89	5.00	4.86	32.75	4774	0.277
	3	350	63	22.05	6.86	6.2×10^{-5}	3.93	4.88	4.86	31.87	4645	0.264
	4	350	63	22.05	5.74	3.8×10^{-5}	4.01	4.85	4.86	32.50	5662	0.328
	5	350	63	22.05	5.74	3.5×10^{-5}	4.01	4.90	4.86	32.37	5639	0.325
	6	350	63	22.05	4.63	3.1×10^{-5}	4.05	4.96	4.86	32.25	6965	0.400
	7	350	64	22.40	4.63	3.4×10^{-5}	4.24	5.14	4.86	32.12	6937	0.392
	8	350	64	22.40	4.63	3.2×10^{-5}	4.37	5.14	4.86	32.37	6991	0.398
	9	350	64	22.40	4.63	3.0×10^{-5}	4.51	5.15	4.86	32.00	6911	0.390
	10	350	64	22.40	4.50	3.0×10^{-5}	4.60	5.15	4.86	31.87	7082	0.397
	11	350	64	22.40	4.50	2.8×10^{-5}	4.72	5.14	4.86	31.50	7000	0.388
	12	350	64	22.40	4.50	2.9×10^{-5}	4.89	5.13	4.86	30.50	6777	0.364
720	1A	202	77.5	15.66	—	—	0.97	5.31	10.75	—	—	—
	1B	202	77.5	15.66	—	—	0.97	5.31	10.75	—	—	—
	2A	299	60.0	17.94	11.10	2.0×10^{-4}	2.87	3.76	4.57	29.87	2690	0.173
	2B	299	60.0	17.94	9.14	2.0×10^{-4}	2.87	3.76	4.57	37.37	4080	0.325
	3	350	60.0	21.00	6.83	3.6×10^{-4}	3.43	3.47	4.62	41.87	6130	0.480
	4	350	60.0	21.00	6.77	4.0×10^{-5}	3.61	3.99	4.62	39.50	5830	0.431

Thrustor Model: LAJ-AF-CG
Propellant: Li/H_2
Test Chamber: 6' x 14'

7053-Final

TABLE B-II

TEST RESULTS (contd)

Run No.	Point No.	I_A amps	V_A volts	P_A kW	$\dot{m}$ mg/sec	P_t torr	P_{C+B} kW	P_{an} kW	P_{mag} kW	T grams	I_{sp} sec	η_o —
720	5A	350	60.0	21.00	6.77	4.2×10^{-5}	3.61	4.07	4.71	37.00	5465	0.378
	5B	350	60.0	21.00	6.77	4.2×10^{-5}	3.61	4.07	4.71	36.37	5372	0.365
	6	350	58.0	20.30	6.77	2.2×10^{-5}	3.61	3.97	4.62	36.37	5372	0.376
	7	350	58.0	20.30	5.74	3.5×10^{-5}	3.65	4.15	4.62	34.37	5076	0.336
	8	350	58.0	20.30	5.74	3.5×10^{-5}	3.65	4.22	4.57	33.75	4985	0.325
	9	350	58.0	20.30	5.74	3.4×10^{-5}	3.74	4.27	4.60	32.12	4744	0.294
	10	350	58.0	20.30	5.74	3.3×10^{-5}	3.76	4.27	4.60	32.12	4892	0.312
	11	350	58.0	20.30	5.74	3.2×10^{-5}	3.80	4.26	4.60	32.12	4892	0.312
	12	350	58.0	20.30	5.70	3.1×10^{-5}	3.83	4.26	4.60	33.12	5810	0.371
	13	350	58.0	20.30	5.70	3.1×10^{-5}	3.87	4.24	4.60	33.12	5810	0.371
	14	350	58.0	20.30	5.70	2.9×10^{-5}	3.93	4.20	4.60	32.25	5657	0.352
	15	350	57.5	20.13	5.70	2.8×10^{-5}	3.88	4.10	4.66	31.87	5591	0.345
	16A	350	57.0	19.95	5.70	2.8×10^{-5}	3.90	4.05	4.50	26.87	4714	0.248
	16B	350	57.0	19.95	5.70	2.8×10^{-5}	3.90	4.05	4.50	29.37	5152	0.297
	17	350	58.0	20.30	5.70	3.0×10^{-5}	4.22	4.09	4.47	31.25	5482	0.332
	18A	350	59.0	20.65	5.78	4.2×10^{-5}	4.31	4.04	4.44	32.50	5622	0.349
	18B	350	59.0	20.65	5.78	4.2×10^{-5}	4.20	4.04	4.44	34.87	6032	0.402
	19	350	60.0	21.00	5.78	4.0×10^{-5}	4.20	4.05	4.92	34.00	5882	0.370
	20	350	60.0	21.00	5.78	4.1×10^{-5}	4.20	4.10	4.92	34.37	5944	0.378
	21	345	60.0	21.00	5.78	4.8×10^{-5}	4.18	4.06	4.86	34.12	5903	0.374
	22	345	60.0	21.00	5.78	3.9×10^{-5}	4.25	4.06	4.83	34.00	5882	0.372

TABLE B-II

TEST RESULTS (contd)

Run No.	Point No.	I_A amps	V_A volts	P_A kW	$\dot{m}$ mg/sec	P_t torr	P_{C+B} kW	P_{an} kW	P_{mag} kW	T grams	I_{sp} sec	η_o —
720	23A	345	58.5	20.18	5.78	3.8×10^{-5}	4.09	3.84	4.80	35.00	6055	0.407
	23B	345	58.5	20.18	5.78	3.8×10^{-5}	4.09	3.84	4.80	34.37	5944	0.392
	24	345	59.0	20.36	5.78	4.1×10^{-5}	4.02	4.00	4.80	32.75	5666	0.354
	25A	345	60.0	20.70	5.78	5.5×10^{-5}	4.14	4.50	4.80	30.62	5297	0.305
	25B	345	60.0	20.70	5.78	5.5×10^{-5}	4.14	4.50	4.80	29.37	5081	0.280
	26A	345	61.0	21.05	5.78	4.5×10^{-5}	4.01	4.40	4.77	32.50	5622	0.339
	26B	345	61.0	21.05	5.78	4.5×10^{-5}	4.01	4.40	4.77	35.62	6162	0.408
	27	345	54.0	18.73	5.78	3.4×10^{-5}	4.20	3.84	4.74	35.00	6055	0.433
	28A	345	56.0	19.32	5.78	3.6×10^{-5}	4.25	3.68	4.05	35.62	6162	0.438
	28B	345	56.0	19.32	5.78	3.6×10^{-5}	4.25	3.68	3.90	33.75	5839	0.393
	29A	345	57.0	19.66	5.78	3.8×10^{-5}	4.12	3.84	3.87	33.37	5773	0.378
	29B	345	57.0	19.66	5.78	3.8×10^{-5}	4.12	3.84	4.05	35.62	6162	0.430
	30	345	55.5	19.15	5.78	3.4×10^{-5}	4.28	3.86	4.05	35.62	6162	0.440
	31	345	56.5	19.49	5.78	4.6×10^{-5}	4.17	3.74	3.85	35.62	6162	0.435
	32A	345	57.5	19.83	5.78	4.5×10^{-5}	4.17	4.00	3.90	36.25	6271	0.444
	32B	345	57.5	19.83	5.78	4.5×10^{-5}	4.00	4.17	4.00	35.00	6055	0.414
	33	345	56.5	19.49	5.78	3.4×10^{-5}	3.62	4.17	3.92	34.00	5882	0.396
	34	345	57.5	19.83	5.78	3.8×10^{-5}	3.91	4.17	3.81	32.62	5643	0.359
	35	345	57.0	19.66	5.78	3.6×10^{-5}	3.83	4.23	3.92	34.00	5882	0.395
	36	345	58.0	20.01	5.78	3.7×10^{-5}	3.92	4.21	3.88	33.50	5795	0.376
	37	345	56.0	19.32	5.78	3.4×10^{-5}	3.74	4.19	3.92	33.50	5795	0.387
	38	345	58.5	20.18	5.78	4.1×10^{-5}	3.85	4.21	3.85	32.62	5626	0.355

TABLE B-II

TEST RESULTS (contd)

Run No.	Point No.	I_A amps	V_A volts	P_A kW	$\dot{m}$ mg/sec	P_t torr	P_{C+B} kW	P_{an} kW	P_{mag} kW	T grams	I_{sp} sec	η_o —
720	39	345	57.0	19.66	5.78	4.0×10^{-5}	3.94	4.15	3.90	33.25	5752	0.377
	40	345	58.0	20.01	5.78	4.0×10^{-5}	3.92	4.19	3.87	32.87	5687	0.363
	41A	348	53.0	18.44	5.80	3.4×10^{-5}	4.21	4.32	3.75	31.37	5408	0.350
	41B	348	53.0	18.44	5.80	3.4×10^{-5}	4.21	4.32	3.66	28.75	4956	0.294
	42	345	58.0	20.01	5.80	3.6×10^{-5}	3.96	4.54	3.51	28.37	4891	0.268
	43	342	56.0	19.15	5.80	4.1×10^{-5}	4.36	4.32	3.61	29.62	5106	0.308
	44	351	56.0	19.66	5.80	3.5×10^{-5}	4.21	4.41	3.65	30.12	5193	0.305
	45	350	57.0	19.95	5.83	3.5×10^{-5}	4.37	4.08	4.80	31.12	5337	0.322
	46	350	57.0	19.95	5.83	3.4×10^{-5}	4.39	3.99	4.80	31.87	5466	0.338
	47	350	55.5	19.43	5.83	3.4×10^{-5}	4.39	3.91	4.90	32.00	5488	0.346
	48	351	56.0	19.66	5.83	3.3×10^{-5}	4.37	3.83	4.96	30.75	5274	0.316
	49	301	61.0	18.36	—	—	2.09	7.26	5.05	—	—	—
	50	200	80.5	16.10	—	—	1.46	7.15	10.56	—	—	—
721	1	350	51.0	17.85	5.73	5.4×10^{-5}	4.55	3.42	4.83	30.00	5235	0.332
	2	355	49.0	17.40	5.73	2.8×10^{-4}	8.58	5.02	4.80	10.87	1897	—
	3	355	53.0	18.82	5.68	4.9×10^{-5}	4.87	3.85	4.77	28.37	4995	0.346
	4	350	55.0	19.25	5.73	5.4×10^{-5}	4.83	4.01	4.65	28.12	4908	0.276
	5	348	56.0	19.49	5.73	4.8×10^{-5}	4.90	4.40	4.65	28.37	4951	0.279
	6	355	57.0	20.24	5.73	4.7×10^{-5}	5.24	4.60	4.89	30.50	5323	0.309
	7	355	57.0	20.24	5.73	5.2×10^{-5}	5.56	4.82	4.92	30.37	5300	0.307
	8	355	57.0	20.24	6.76	4.4×10^{-5}	5.65	4.89	4.89	30.75	5489	0.322
	9	351	59.0	20.71	5.73	4.7×10^{-5}	6.03	5.03	4.89	30.12	5257	0.296

TABLE B-II

TEST RESULTS (contd)

Run No.	Point No.	I_A amps	V_A volts	P_A kW	$\dot{m}$ mg/sec	P_t torr	P_{C+B} kW	P_{an} kW	P_{mag} kW	T grams	I_{sp} sec	η_b —
721	10	351	55.0	19.31	5.73	4.0×10^{-5}	4.96	4.64	4.83	29.50	5148	0.301
	11	355	53.0	18.82	5.73	3.6×10^{-5}	4.87	4.23	4.83	30.25	5279	0.324
	12A	351	54.0	18.95	5.73	3.4×10^{-5}	4.92	4.01	4.83	29.37	5126	0.304
	12B	351	54.0	18.95	5.73	3.4×10^{-5}	4.92	4.01	4.83	28.75	5017	0.291
	13	351	58.0	20.35	5.73	3.8×10^{-5}	5.41	4.61	4.79	27.25	4756	0.247
	14	350	59.0	20.63	5.73	4.0×10^{-5}	5.70	4.63	4.70	25.25	4407	0.210
	15A	355	50.0	17.75	5.73	7.0×10^{-5}	6.23	3.86	4.70	22.12	3860	0.182
	15B	355	50.0	17.75	5.73	7.0×10^{-5}	6.23	3.86	4.70	20.25	3534	0.153
	16A	355	50.0	17.75	5.73	5.7×10^{-5}	6.16	3.53	4.70	23.87	4166	0.212
	16B	355	50.0	17.75	5.73	5.7×10^{-5}	6.16	3.53	4.70	22.87	3991	0.195
	17	355	51.5	18.30	5.73	5.8×10^{-5}	6.21	3.83	4.70	21.50	3752	0.168
	18	355	51.5	18.30	5.73	7.0×10^{-5}	6.18	3.74	4.74	22.25	3883	0.180
	19A	355	51.5	18.30	5.73	5.5×10^{-5}	6.16	3.72	4.66	23.87	4166	0.207
	19B	355	51.5	18.30	5.73	5.5×10^{-5}	6.16	3.72	4.66	22.25	3883	0.181
	20	355	50.5	17.90	5.73	4.4×10^{-5}	5.98	3.64	4.66	23.75	4145	0.209
	21A	360	33.0	11.90	5.73	1.2×10^{-5}	5.41	2.23	4.55	33.87	5911	0.489
	21B	360	33.0	11.90	5.73	1.2×10^{-5}	5.41	2.23	4.55	28.87	5038	0.356
	22	360	48.0	17.27	—	—	—	—	4.66	—	—	—
	23	350	59.0	20.63	—	—	—	—	4.87	—	—	—

TABLE B-II

TEST RESULTS (contd)

Run No.	Point No.	I_A amps	V_A volts	P_A kW	$\dot{m}$ mg/sec	P_t torr	P_{C+B} kW	P_{an} kW	P_{mag} kW	T grams	I_{sp} sec	η_b
722	1	134	121	16.21	36.7	—	1.04	5.64	19.26	32.62	888	0.039
	2	136	112	15.23	38.6	—	1.16	6.60	14.66	29.50	764	0.036
	3	138	102	14.08	38.4	—	1.19	6.36	8.91	29.50	768	0.047
	4	202	96.5	19.49	37.3	—	1.50	8.27	8.76	28.75	771	0.037
	5	172	99.0	17.03	37.1	—	1.39	7.62	8.91	31.50	849	0.049
	6	172	99.0	17.03	37.1	—	1.40	7.62	8.91	30.12	812	0.045
723	1	119	109.0	12.20	34.10	—	1.15	4.77	8.91	22.00	645	0.032
	2	200	100.0	20.00	33.80	—	1.51	7.90	8.91	27.87	824	0.038
	3	200	97.0	19.40	33.50	—	1.51	8.23	8.91	26.75	798	0.036
	4	200	97.0	19.40	33.30	—	1.48	8.24	8.91	26.50	795	0.035
	5	200	97.0	19.40	32.20	—	1.50	8.40	8.91	26.12	811	0.035
	6	200	97.0	19.40	32.00	—	1.52	8.40	8.91	26.00	812	0.035
	7A	250	77.0	19.25	6.82	1.2×10^{-4}	3.87	3.55	8.80	30.12	4416	0.227
	7B	250	77.0	19.25	6.82	1.2×10^{-4}	3.87	3.55	8.80	31.37	4600	0.246
	8A	250	77.0	19.25	6.82	1.2×10^{-4}	3.74	3.54	8.80	28.87	4231	0.208
	8B	250	77.0	19.25	6.82	1.2×10^{-4}	3.74	3.54	8.80	30.75	4508	0.237
	9	300	71.0	21.30	6.82	5.0×10^{-5}	3.87	3.49	8.72	45.37	6652	0.482
	10	300	70.0	21.00	6.82	4.5×10^{-5}	4.19	3.53	8.64	45.37	6652	0.488
	11	300	69.0	20.70	6.82	4.3×10^{-5}	4.29	3.53	8.49	45.37	6652	0.496
	12	300	69.0	20.70	6.82	4.0×10^{-5}	4.32	3.39	8.42	43.87	6433	0.465
	13	300	69.5	20.85	6.82	4.0×10^{-5}	4.39	3.41	8.45	44.00	6452	0.465

TABLE B-II

TEST RESULTS (contd)

Run No.	Point No.	I_A amps	V_A volts	P_A kW	$\dot{m}$ mg/sec	P_t torr	P_{C+B} kW	P_{an} kW	P_{mag} kW	T grams	I_{sp} sec	η_b —
723	14A	300	68.0	20.40	6.82	3.8×10^{-5}	4.44	3.26	8.35	45.12	6617	0.498
	14B	300	68.0	20.40	6.82	3.8×10^{-5}	4.44	3.26	8.35	45.75	6708	0.512
	15A	300	68.0	20.40	6.82	3.2×10^{-5}	4.50	3.10	8.35	45.87	6726	0.515
	15B	300	68.0	20.40	6.82	3.2×10^{-5}	4.50	3.10	8.35	43.87	6433	0.471
	16	300	68.0	20.40	6.82	4.2×10^{-5}	4.55	3.29	8.35	42.62	6249	0.444
	17	298	70.0	20.86	6.82	2.7×10^{-5}	4.58	3.14	8.35	42.50	6232	0.435
	18A	300	69.0	20.70	6.82	4.1×10^{-5}	4.62	3.45	8.35	42.00	6158	0.427
	18B	300	69.0	20.70	6.82	4.1×10^{-5}	4.62	3.45	8.35	44.50	6525	0.479
	19A	300	68.0	20.40	6.82	3.9×10^{-5}	4.59	3.24	8.35	42.00	6158	0.431
	19B	300	68.0	20.40	6.82	3.9×10^{-5}	4.59	3.24	8.35	41.37	6066	0.418
	20	300	68.0	20.40	6.82	4.2×10^{-5}	4.64	3.36	8.35	41.37	6066	0.418
	21	300	62.0	18.60	6.82	8.4×10^{-6}	3.50	2.79	8.35	54.30	7991	0.775
	22	300	69.0	20.70	6.82	2.8×10^{-5}	4.64	3.42	8.35	40.75	5975	0.402
	23A	300	67.0	20.10	6.82	3.8×10^{-5}	4.61	3.42	8.35	41.37	6066	0.423
	23B	300	67.0	20.10	6.82	3.8×10^{-5}	4.61	3.42	8.35	51.37	7532	0.652
	24A	300	63.0	18.90	6.82	2.0×10^{-5}	4.36	2.58	8.35	46.37	6799	0.555
	24B	300	63.0	18.90	6.82	2.0×10^{-5}	4.36	2.58	8.35	37.62	5516	0.365
	25	300	68.0	20.40	6.82	3.6×10^{-5}	4.61	3.43	8.35	39.50	5792	0.381
	26A	303	62.0	18.78	6.82	1.4×10^{-5}	3.99	2.92	8.35	49.50	7258	0.635
	26B	303	62.0	18.78	6.82	1.4×10^{-5}	3.99	2.92	8.35	46.37	6799	0.557
	27	300	69.0	20.70	6.82	3.4×10^{-5}	4.58	3.29	8.35	37.62	5516	0.342
	28	300	64.0	19.20	6.82	2.8×10^{-5}	4.40	3.22	8.35	40.75	5975	0.424

TABLE B-II

TEST RESULTS (contd)

Run No.	Point No.	I_A amps	V_A volts	P_A kW	$\dot{m}$ mg/sec	P_t torr	P_{C+B} kW	P_{an} kW	P_{mag} kW	T grams	I_{sp} sec	η_o
723	29	302	62.0	18.72	6.82	1.4×10^{-5}	3.92	2.87	8.35	48.87	7166	0.620
	30	300	69.0	20.70	6.82	3.5×10^{-5}	4.48	3.22	8.35	50.12	7349	0.608
	31	300	66.0	19.80	6.82	3.4×10^{-5}	4.61	3.31	8.35	38.87	5699	0.377
	38	300	69.0	20.70	6.82	2.8×10^{-5}	4.41	3.30	8.76	41.12	6029	0.403
	39	302	69.0	20.84	6.82	2.3×10^{-5}	4.62	3.43	8.80	41.25	6048	0.404
	40	302	67.0	20.23	6.82	3.4×10^{-5}	4.61	3.38	8.80	42.12	6176	0.430
	41A	304	63.0	19.15	6.82	1.6×10^{-5}	4.00	2.79	8.80	49.25	7221	0.610
	41B	304	63.0	19.15	6.82	1.6×10^{-5}	4.00	2.79	8.80	40.50	5938	0.412
	42	303	66.0	19.99	6.82	3.2×10^{-5}	4.66	3.32	8.80	42.37	6213	0.438
	43	304	63.0	19.15	6.82	1.8×10^{-5}	4.35	2.79	8.80	44.25	6488	0.492
	44A	304	64.0	19.46	6.82	2.0×10^{-5}	4.41	2.66	8.80	44.25	6488	0.487
	44B	304	64.0	19.46	6.82	2.0×10^{-5}	4.41	2.66	8.80	41.12	6029	0.421
	45	304	67.0	20.37	6.82	3.4×10^{-5}	4.65	3.44	8.80	41.75	6128	0.421
	46A	305	62.0	18.91	6.82	3.2×10^{-5}	4.10	2.55	8.80	47.37	6946	0.569
	46B	305	62.0	18.91	6.82	3.2×10^{-5}	4.10	2.55	8.80	40.50	5938	0.416
	47	300	70.0	21.00	6.82	3.2×10^{-5}	4.57	3.62	8.80	40.75	5975	0.392
	48	304	65.0	19.76	6.82	3.0×10^{-5}	4.69	3.21	8.80	44.25	6488	0.482
	49	300	73.0	21.90	6.82	2.4×10^{-5}	4.76	3.60	8.80	40.12	5883	0.368
	50	300	72.0	21.60	6.82	3.3×10^{-5}	4.71	3.81	8.80	40.75	5975	0.384
	51A	304	69.0	20.98	6.82	3.4×10^{-5}	4.66	3.68	8.59	37.00	5425	0.251
	51B	304	69.0	20.98	6.82	3.4×10^{-5}	4.66	3.68	8.59	38.87	5699	0.359
	52	306	64.0	19.58	6.82	1.6×10^{-5}	3.50	2.85	8.59	42.00	6158	0.440

TABLE B-II

TEST RESULTS (contd)

Run No.	Point No.	I_A amps	V_A volts	P_A kW	$\dot{m}$ mg/sec	P_t torr	P_{C+B} kW	P_{an} kW	P_{mag} kW	T grams	I_{sp} sec	η_o —
723	53	310	59.0	18.29	6.82	6.5×10^{-6}	4.12	2.86	8.59	50.75	7441	0.674
	54	300	79.0	23.70	6.82	6.2×10^{-5}	5.25	4.35	8.99	33.50	4912	0.241
	55	300	79.0	23.70	6.82	5.5×10^{-5}	5.30	4.59	9.14	33.50	4912	0.240
	56A	304	68.0	20.67	6.82	4.2×10^{-5}	4.81	4.44	9.14	37.75	4949	0.300
	56B	304	68.0	20.67	6.82	4.2×10^{-5}	4.81	4.44	9.14	29.50	4326	0.205
724	1	200	81.0	16.20	26.0	—	1.37	7.17	8.72	112.3	4310	0.931
	2A	296	76.5	22.64	6.83	0.5×10^{-4}	4.90	4.46	8.42	14.00	2052	0.044
	2B	296	76.5	22.64	6.83	0.5×10^{-4}	4.90	4.46	8.42	17.12	2506	0.066
	3	300	76.0	22.80	6.82	1.2×10^{-4}	4.91	4.51	8.42	17.62	2583	0.069
	4A	300	74.0	22.20	6.82	7×10^{-4}	5.14	4.29	8.34	24.50	3592	0.138
	4B	300	74.0	22.20	6.82	7×10^{-4}	5.14	4.29	8.34	27.62	4049	0.175
	5	300	71.0	21.30	6.82	5.8×10^{-4}	4.94	4.16	8.40	27.62	4049	0.180
	6A	303	60.0	18.18	6.82	0.9×10^{-4}	2.86	2.60	8.40	36.37	5332	0.350
	6B	303	60.0	18.18	6.82	0.9×10^{-4}	2.86	2.60	8.40	33.87	4966	0.303
	7	300	59.0	17.70	6.82	1×10^{-5}	2.88	1.79	8.34	33.25	4875	0.298
	8	292	77.0	22.48	6.82	2×10^{-5}	3.89	2.95	8.34	37.62	5516	0.323
	9A	303	68.0	20.60	6.82	2.6×10^{-5}	4.89	3.77	8.34	31.37	4599	0.239
	9B	303	68.0	20.60	6.82	2.6×10^{-5}	4.89	3.77	8.34	30.12	4416	0.220
	10	300	69.0	20.70	6.82	3.0×10^{-5}	4.79	4.02	8.34	30.12	4416	0.219
	11	300	69.0	20.70	6.82	2.2×10^{-5}	4.90	4.06	8.80	32.00	4692	0.244
	12	298	70.0	20.86	6.82	2.2×10^{-5}	5.11	4.19	8.84	32.62	4782	0.252

Thrustor Model: LAJ-AF-CG2
Propellant: Li/H_2
Test Chamber: 6' x 14'

7053-Final

155

TABLE B-II

TEST RESULTS (contd)

Run No.	Point No.	I_A amps	V_A volts	P_A kW	$\dot{m}$ mg/sec	p_t torr	P_{C+B} kW	P_{an} kW	P_{mag} kW	T grams	I_{sp} sec	η_o —
724	13A	298	66.0	19.66	6.82	2.5×10^{-5}	5.10	4.40	8.80	32.62	4782	0.263
	13B	298	66.0	19.66	6.82	2.5×10^{-5}	5.10	4.40	8.80	35.75	5241	0.315
	14A	300	68.0	20.40	6.82	2.5×10^{-5}	4.82	3.72	8.80	35.75	5241	0.307
	14B	300	68.0	20.40	6.82	2.5×10^{-5}	4.82	3.72	8.80	33.87	4966	0.276
	15	298	68.0	20.26	6.82	2.8×10^{-5}	4.83	3.93	8.80	32.12	4709	0.249
	16	298	69.0	20.56	6.82	3.0×10^{-5}	5.11	4.14	8.80	30.62	4489	0.224
	17	298	71.0	21.15	6.82	3.8×10^{-5}	5.45	4.33	8.80	29.62	4343	0.206
	18	298	68.0	20.26	6.82	4.2×10^{-5}	5.16	3.87	8.80	30.62	4489	0.227
	19	298	69.5	20.71	6.82	4.4×10^{-5}	6.70	3.95	8.80	30.62	4489	0.223
	20	298	69.5	20.71	6.82	4.4×10^{-5}	5.23	3.87	8.80	30.62	4489	0.223
	21	298	69.5	20.71	6.82	4.4×10^{-5}	5.13	3.89	8.84	30.50	4472	0.221
	22	298	69.5	20.71	6.82	4.2×10^{-5}	5.14	3.91	8.84	30.12	4416	0.215
	23	298	69.5	20.71	6.82	4.4×10^{-5}	5.18	3.89	8.88	30.62	4489	0.223
	24	298	69.0	20.56	6.82	4.2×10^{-5}	5.14	3.83	8.84	30.62	4489	0.224
	25	298	69.0	20.56	6.82	4.1×10^{-5}	5.15	3.87	8.88	30.62	4489	0.224
	26	300	69.5	20.85	6.82	4.1×10^{-5}	5.14	3.87	8.88	30.62	4489	0.221
	27	300	69.5	20.85	6.82	4.5×10^{-5}	5.35	3.96	8.84	30.75	4508	0.223
	28	300	70.0	21.00	6.82	4.2×10^{-5}	6.72	3.95	8.96	31.00	4545	0.225
	29A	300	70.0	21.00	6.82	4.0×10^{-5}	5.06	3.98	8.92	32.00	4692	0.240
	29B	300	70.0	21.00	6.82	4.0×10^{-5}	5.06	3.99	8.92	34.50	5058	0.280

156

TABLE B-II
TEST RESULTS (contd)

Point No.	T gram	ṁ mg/sec	I_{sp} sec	P_t 10^{-4} torr	1 I_A amp	2 V_A volt	3 P_A kW	P_{mag} kW	P_{c+b} kW	P_{an} kW	η_{TH}	η_F	η_o
Run 725*													
1	--	7.32	--	500	250	81.0	20.25	13.23	2.62	5.48	0.600	--	--
2	27.4	6.30	4349	1.4	302	74.0	22.35	9.07	4.26	4.35	0.615	0.255	0.182
3	26.9	6.35	4236	0.6	302	73.0	22.05	9.07	4.56	4.36	0.596	0.248	0.175
4	22.6	4.85	4659	0.8	298	80.5	23.99	9.07	4.91	5.16	0.581	0.210	0.152
5	25.7	7.05	3645	0.4	304	71.0	21.58	9.27	4.70	4.07	0.594	0.254	0.178
6	25.8	7.05	3659	0.4	293	73.0	21.75	9.23	4.75	4.01	0.598	0.208	0.146
7	27.5	8.35	3293	0.8	298	64.0	19.07	9.39	4.54	3.47	0.580	0.228	0.152
8	28.2	8.35	3377	0.8	298	64.0	19.07	9.46	4.50	3.15	0.600	0.239	0.160
9	27.9	8.35	3341	0.76	298	64.0	19.07	9.55	4.51	3.12	0.600	0.234	0.156
Run 727													
1	31.79	5.59	5687	1.4	295	75.0	22.13	18.88	3.85	5.31	0.586	0.392	0.212
2	31.27	7.03	4448	1.4	300	70.0	21.00	18.88	4.03	5.07	0.567	0.318	0.167
3	25.81	5.42	4762	1.2	309	61.0	18.54	8.80	4.09	5.32	0.493	0.318	0.216
4	25.86	5.59	4626	1.6	350	54.0	18.90	4.74	4.24	4.04	0.563	0.304	0.243
5	25.62	7.03	3644	1.4	350	50.0	17.50	4.77	5.25	4.08	0.467	0.256	0.201
6	25.23	6.95	3630	1.5	375	52.0	19.50	3.92	5.59	4.31	0.493	0.226	0.188

*Note: Data from Runs 725 through 732 are presented in a slightly different format.

TABLE B-II
TEST RESULTS (contd)

Point No.	T gram	ṁ mg/sec	I_{sp} sec	P_t 10^{-4} torr	I_A amp	V_A volt	P_A kW	P_{mag} kW	P_{c+b} kW	P_{em} kW	η_{TH}	η_F	η_o
Run 727 (contd)													
61	27.54	7.54	3653	1.1	425	36.9	15.68	3.97	6.10	3.25	0.404	0.308	0.246
62	32.67		4333	1.1	421	46.5	19.58	4.07	6.78	3.86	0.457	0.347	0.287
63	32.92		4366	1.1	421	44.0	18.52	4.03	6.38	3.77	0.452	0.373	0.306
64	31.92		4233	1.1	422	43.7	18.44	4.08	6.46	3.76	0.446	0.352	0.288
65	31.30		4218	1.1	422	43.5	18.36	4.03	6.56	3.65	0.444	0.351	0.287
66	30.67		4068	1.1	422	42.3	17.35	4.00	6.48	3.57	0.437	0.336	0.274
67	31.12		4167	1.1	422	42.7	18.02	3.97	6.62	3.53	0.437	0.349	0.286
68	31.27		4147	1.0	428	40.4	17.29	4.45	6.37	3.49	0.430	0.360	0.286
69	30.40		4032	1.0	427	40.3	17.21	3.93	6.48	3.37	0.428	0.342	0.278
70	31.64		4196	1.0	429	40.3	17.29	4.14	6.38	3.38	0.436	0.368	0.297
71	31.39	7.54	4163	1.1	428	39.7	16.99	3.99	6.35	3.27	0.434	0.369	0.299
72	31.63	7.54	4195	1.1	432	38.4	16.59	4.30	6.34	3.34	0.417	0.384	0.305
73	29.76	7.53	3952	1.1	430	37.5	16.13	4.23	6.51	3.29	0.393	0.350	0.278
74	30.37	7.55	4023	1.0	433	37.9	16.41	4.36	6.16	3.44	0.415	0.357	0.282
75	30.12	7.55	3989	1.1	433	38.0	16.45	4.03	6.00	3.44	0.426	0.351	0.282
76	29.75	7.55	3940	1.1	432	36.5	15.77	3.97	5.63	3.51	0.421	0.357	0.285
77	30.74	7.50	4099	1.1	432	37.9	16.37	3.96	5.49	3.52	0.450	0.370	0.298
78	31.13	7.55	4123	1.1	428	48.0	20.54	3.97	6.27	4.06	0.497	0.300	0.251

(In the ṁ column, an arrow indicates the value 7.54 mg/sec applies from point 61 through point 71.)

TABLE B-II

TEST RESULTS (contd)

Point No.	T gram	$\dot{m}$ mg/sec	I_{sp} sec	P_t 10^{-4} torr	I_A amp	V_A volt	P_A kW	P_{mag} kW	P_{c+b} kW	P_{en} kW	η_{TH}	η_F	η_o
Run 727 (contd)													
97	28.25	7.49	3772	1.1	430	42.0	18.06	4.13	6.07	4.04	0.440	0.283	0.230
98	31.25		4172	0.9	430	42.5	18.28	4.17	6.18	4.06	0.440	0.342	0.279
99	33.00		4406	1.0	430	42.0	18.06	4.13	6.23	4.02	0.433	0.386	0.315
100	33.37	7.49	4455	0.9	430	42.5	18.28	4.19	6.21	3.98	0.443	0.391	0.318
101	31.02	7.57	4098	1.0	429	42.5	18.23	3.89	6.23	3.97	0.441	0.335	0.276
102	29.25	7.49	3905	1.0	430	43.2	18.58	3.90	6.21	4.09	0.446	0.295	0.244
103	29.25	7.49	3905	1.0	430	42.5	18.28	3.92	6.24	3.97	0.442	0.300	0.247
104	28.74	7.45	3858	1.0	429	42.9	18.40	3.92	6.32	4.05	0.437	0.289	0.238
105	28.50	7.49	3805	1.0	430	43.0	18.49	3.97	6.40	4.09	0.433	0.282	0.232
106	27.87		3721	1.0	430	43.0	18.49	3.97	6.35	3.97	0.448	0.269	0.222
107	27.25		3638	1.0	430	42.9	18.45	4.01	6.32	4.00	0.441	0.258	0.212
108	26.25		3505	1.0	430	42.2	18.15	4.03	6.34	3.94	0.434	0.244	0.199
109	25.99		3470	1.0	431	41.5	17.89	4.14	6.37	3.83	0.430	0.242	0.197
110	27.36		3653	1.0	432	41.0	17.71	4.17	6.57	3.72	0.419	0.271	0.219
111	28.11		3753	1.0	432	41.0	17.71	4.23	6.51	3.73	0.422	0.286	0.231
112	26.98		3602	1.0	435	41.0	17.84	4.29	6.44	3.80	0.427	0.261	0.211
113	25.36	7.49	3386	1.0	403	40.4	16.28	4.13	6.08	3.39	0.419	0.253	0.202
114	25.23	7.48	3373	0.9	403	41.1	16.56	4.17	6.08	3.22	0.439	0.246	0.197

(Note: the $\dot{m}$ column shows arrows indicating a constant value of 7.49 mg/sec across rows 97–99 and 106–113.)

TABLE B-II

TEST RESULTS (contd)

Point No.	T gram	ṁ mg/sec	I_{sp} sec	P_t 10^{-4} torr	I_A amp	V_A volt	P_A kW	P_{mag} kW	P_{c+b} kW	P_{an} kW	η_{TH}	η_F	η_o
Run 727 (contd)													
115	24.57	7.48	3285	0.85	376	40.7	15.30	4.17	5.75	2.93	0.433	0.253	0.199
116	25.07	7.48	3352	0.80	376	40.5	15.23	4.19	5.66	2.74	0.449	0.265	0.208
117	26.20	7.48	3503	0.85	377	39.5	14.89	4.23	5.64	2.69	0.441	0.296	0.231
Run 729 (NH₃)													
1	3.82	14.2	269	5.6	148	72.0	10.66	6.93	3.06	4.19	0.320	0.005	0.003
2	13.57	8.3	1635	4.0	200	118.0	23.60	6.85	4.45	--	--	0.045	0.035
Run 730 (NH₃)													
1	9.27	14.4	644	2.0	244	79.0	19.28	12.56	3.94	8.74	0.343	0.015	0.009
2	7.70	11.2	687	2.2	250	73.5	18.38	4.28	3.88	8.12	0.348	0.014	0.011
3	7.75	9.1	852	2.4	350	67.0	23.45	1.84	6.25	10.2	0.299	0.014	0.013
4	12.11	8.9	1360	2.8	400	62.0	24.80	1.82	7.62	12.0	0.210	0.032	0.030
5	12.70	8.3	1530	2.2	450	68.0	30.60	1.77	7.86	15.4	0.242	0.030	0.029
Run 731													
1A	24.5	5.69	4306	3.8	300	57.0	17.10	6.81	4.50	3.42	0.537	0.296	0.211
1B	22.2	6.55	3389	4.6	300	49.0	14.70	6.34	6.26	3.19	0.357	0.246	0.168
2	25.0	6.53	3828	4.3	300	52.0	15.60	4.75	6.69	3.06	0.375	0.294	0.226

TABLE B-II

TEST RESULTS (contd)

Point No.	T gram	$\dot{m}$ mg/sec	I_{sp} sec	P_t 10^{-4} torr	I_A amp	V_A volt	P_A kW	P_{mag} kW	P_{c+b} kW	P_{en} kW	η_{TH}	η_F	η_o
Run 731 (contd)													
3	21.4	6.53	3277	4.4	300	47.0	14.10	3.00	6.97	2.64	0.319	0.239	0.197
4	22.1	5.66	3905	4.5	300	52.5	15.30	4.75	6.92	3.35	0.350	0.262	0.201
5	18.4	4.68	3932	4.5	300	54.0	16.20	4.75	6.72	3.58	0.364	0.214	0.166
Run 732													
1	8.1	6.00	1350	--	100	79.0	7.90	4.59	1.00		0.602	0.066	0.042
2	17.5	5.94	2946	--	254	76.0	19.30	4.53	3.08		0.658	0.128	0.104
3	25.0	5.94	4203	3.0	253	53.5	13.54	4.53	3.39		0.558	0.373	0.279
4	28.2	5.66	4982	2.0	300	62.0	18.60	4.53	4.40		0.621	0.362	0.291
5	30.0	5.65	5309	1.9	300	60.0	18.00	4.53	4.29		0.623	0.425	0.339
6	27.0	5.65	4778	2.0	300	60.5	18.15	3.98	4.54		0.603	0.341	0.280
7	28.7	5.65	5079	1.0	300	58.5	17.55	3.98	4.45		0.602	0.399	0.325
8	26.7	5.51	4845	3.2	300	58.5	17.55	3.15	4.76		0.577	0.354	0.300
9	26.6	5.36	4962	2.2	300	58.5	17.55	3.12	4.96		0.565	0.361	0.306
10	26.1	5.35	4878	2.2	300	58.5	17.55	3.12	4.98		0.564	0.348	0.296
11	25.1	5.35	4691	1.9	300	58.1	17.43	3.12	5.00		0.562	0.324	0.275
12	24.6	5.35	4598	1.7	300	58.0	17.40	3.12	5.03		0.562	0.312	0.265
13	24.3	5.35	4542	1.7	300	58.0	17.40	3.12	5.05		0.564	0.304	0.258

Point No.	T gram	$\dot{m}$ mg/sec	I_{sp} sec	P_t 10^{-4} torr	I_A amp	V_A volt	P_A kW	P_{mag} kW	P_{c+b} kW	P_{en} kW	η_{TH}	η_F	η_o
Run 732 (contd)													
31	32.1	5.42	5923	2.8	300	56.0	16.80	3.15	5.05		0.557	0.543	0.457
32	31.7		5848	2.4	300	56.0	16.80	3.15	5.12		0.549	0.530	0.446
33	30.1		5553	2.4	300	56.0	16.80	3.18	5.11		0.548	0.478	0.402
34	28.8		5313	2.3	300	56.0	16.80	3.18	5.07		0.551	0.437	0.368
35	28.1		5184	2.3	300	55.5	16.65	3.18	5.05		0.549	0.420	0.353
36	27.6		5092	2.4	300	55.5	16.65	3.20	4.98		0.553	0.405	0.340
37	26.2	5.42	4833	2.9	300	55.5	16.65	3.23	4.98		0.550	0.365	0.306
38	25.4	5.43	4677	2.4	300	55.5	16.65	3.23	5.00		0.551	0.342	0.287
39	24.3	5.43	4567	2.2	300	56.0	16.80	3.23	5.03		0.556	0.324	0.272
40	25.3	5.06	4558	2.9	300	56.0	16.80	3.25	4.94		0.559	0.336	0.281
41	25.7	5.64	4556	2.8	300	56.5	16.95	3.21	4.98		0.560	0.332	0.279
42	24.6	5.65	4353	2.8	300	55.5	16.65	3.21	4.95		0.555	0.309	0.259
43	24.1	5.65	4265	2.3	300	55.9	16.77	3.20	4.95		0.559	0.293	0.246
44	23.8	5.66	4204	2.8	300	56.5	16.95		4.88		0.567	0.283	0.238
45	24.0	5.65	4247	3.0	300	56.5	16.95		4.95		0.561	0.288	0.242
46	24.4	5.66	4310	3.2	301	56.5	16.95		4.97		0.561	0.297	0.250
47	23.5	5.65	4159	3.4	300	57.0	17.10		5.03		0.556	0.274	0.231
48	22.0	5.65	3893	3.0	300	56.2	16.86		5.03		0.553	0.244	0.205

TABLE B-II

TEST RESULTS (contd)

Point No.	T gram	ṁ mg/sec	I_{sp} sec	P_t 10^{-4} torr	I_A amp	V_A volt	P_A kW	P_{mag} kW	P_{c+b} kW	P_{sn} kW	η_{TH}	η_F	η_o
Run 732 (contd)													
85	24.0	5.63	4225	(1.0)	300	56.0	16.80	3.18	4.97		0.556	0.290	0.244
86	24.9	5.68	4383	--	300	56.0	16.80	3.18	5.04		0.552	0.312	0.262
87	25.2	5.65	4436	2.4	302	57.0	17.21	3.20	5.08		0.558	0.312	0.263
88	26.9	5.66	4752	(1.1)	300	54.5	16.35	3.18	4.68		0.617	0.375	0.314
89	31.0	5.67	5467	0.9	300	53.5	16.05		4.57		0.615	0.507	0.423
90	24.5	5.67	4320	2.1	300	56.0	16.80		5.20		0.548	0.302	0.254
91	24.3	5.66	4293	2.0	300	56.2	16.86		5.20		0.552	0.297	0.250
92	24.3	5.65	4300	2.2	300	56.3	16.89		5.30		0.541	0.297	0.250
93	24.1	5.65	4265	2.1	302	56.3	17.00		5.28		0.547	0.290	0.244
94	24.0	5.65	4389	2.1	303	55.7	16.88		5.26		0.536	0.309	0.260
95	23.7	5.66	4187	2.1	303	56.0	16.97		5.19		0.549	0.281	0.236
96	23.2	5.66	4098	2.1	303	54.5	16.51	3.18	5.08		0.545	0.276	0.232
97	22.8	5.66	4028	2.1	304	55.0	16.72	3.20	5.08		0.548	0.264	0.221
98	22.5	5.66	3975	2.1	302	54.5	16.46	3.15	5.08		0.541	0.261	0.219
99	22.2	5.65	3929	2.0	302	55.5	16.76	3.15	5.26		0.537	0.250	0.210
100	21.7	5.65	3840	2.0	303	55.7	16.88	3.15	5.13		0.548	0.237	0.200
101	21.6	5.65	3823	1.9	303	55.7	16.88	3.18	5.17		0.547	0.235	0.198
102	22.3	5.65	3946	2.0	303	56.2	17.03	3.15	5.24		0.546	0.248	0.209

(In the P_{mag} column, an arrow spans from point 88 through point 96 indicating a constant value of ≈3.18.)

TABLE B-II

TEST RESULTS (contd)

Point No.	T gram	ṁ mg/sec	I_{sp} sec	P_t 10^{-4} torr	I_A amp	V_A volt	P_A kW	P_{mag} kW	P_{c+b} kW	P_{sm} kW	η_{TH}	η_F	η_o
Run 732 (contd)													
139	24.1	5.65	4265	2.3	302	57.5	17.37	3.15	5.42		0.537	0.284	0.240
140	24.6		4353	2.2	302	57.6	17.40	3.18	5.44		0.537	0.295	0.250
141	24.4		4318	2.2	302	57.3	17.30	3.18	5.40		0.537	0.292	0.247
142	24.3		4300	2.3	302	58.0	17.52	3.18	5.42		0.542	0.286	0.242
143	24.0		4247	2.2	302	57.2	17.27	3.18	5.38		0.539	0.283	0.239
144	24.1		4265	2.2	302	56.5	17.06	3.15	5.38		0.531	0.289	0.244
145	24.2		4283	2.3	301	58.0	17.46	3.15	5.44		0.538	0.285	0.241
146	24.0	5.65	4247	2.2	304	58.0	17.63	3.23	5.47		0.542	0.277	0.235
147	23.3	5.66	4116	2.3	302	56.0	17.52	3.15	5.47		0.538	0.263	0.223
148	22.4	5.65	3964	2.4	302	58.0	17.52	3.15	5.47		0.540	0.243	0.206
149	22.2	5.66	3922	2.3	302	57.5	17.37	3.15	5.43		0.538	0.241	0.204
150	21.9	5.65	3876	2.2	300	58.5	17.55	3.13	5.47		0.540	0.232	0.197
151	21.8		3858	2.2	300	58.5	17.55	3.11	5.43		0.544	0.230	0.195
152	21.3		3769	2.4	301	58.0	17.46	3.15	5.36		0.544	0.221	0.187
153	21.7		3840	2.2	300	59.0	17.70	3.15	5.39		0.550	0.226	0.192
154	21.7	5.65	3840	2.3	300	58.0	17.40	3.13	5.56		0.532	0.230	0.195
155	21.7	5.66	3833	2.3	301	58.0	17.46	3.13	5.45		0.540	0.229	0.194
156	21.4	5.66	3780	2.3	300	58.5	17.55	3.13	5.45		0.540	0.221	0.188

TABLE B-II

TEST RESULTS (contd)

Point No.	T gram	ṁ mg/sec	I_{sp} sec	P_t 10^{-4} torr	I_A amp	V_A volt	P_A kW	P_{mag} kW	P_{c+b} kW	P_{an} kW	η_{TH}	η_F	η_o
Run 732 (contd)													
211	21.5	5.66	3798	1.9	301	59.0	17.76	3.13	5.75		0.545	0.221	0.188
212	21.5	5.66	3798	1.9	301	59.5	17.91		5.82		0.543	0.219	0.186
213	21.0	5.66	3710	1.9	301	59.5	17.91		5.77		0.546	0.209	0.178
214	21.2	5.66	3745	1.9	301	59.5	17.91		5.82		0.544	0.213	0.181
215	21.7	5.67	3827	1.9	301	60.0	18.06		5.80		0.549	0.221	0.188
216	21.2		3738	1.8	302	59.0	17.82		5.82		0.541	0.213	0.182
217	21.2		3738	1.9	302	59.0	17.82		5.77		0.553	0.213	0.182
218	21.2		3738	1.9	300	60.0	18.00	3.13	5.89		0.540	0.211	0.180
219	21.2		3738	1.9	300	59.5	17.85	3.10	5.75		0.551	0.213	0.182
220	21.2	5.67	3738	1.9	298	60.0	17.88	3.10	5.86		0.548	0.213	0.181
221	21.6	5.67	3816	1.9	300	59.5	17.85	3.10	5.80		0.550	0.222	0.189
222	21.0	5.66	3710	1.9	300	59.0	17.70	3.11	5.77		0.548	0.211	0.180
223	20.8	5.66	3674	1.8	300	60.0	18.00	3.13	5.69		0.544	0.204	0.174
224	22.1	5.67	3897	1.8	300	59.5	17.85	3.13	5.80		0.553	0.232	0.197
225	21.0	5.67	3703	2.4	302	61.5	18.57	3.16	5.60		0.560	0.201	0.172
226	23.0	5.68	4049	2.0	301	60.0	18.06	3.15	5.95		0.559	0.248	0.211
227	25.1	5.69	4411	2.2	303	59.5	18.03	3.16	5.91		0.556	0.295	0.251
228	23.8	5.68	4190	2.0	303	59.3	17.97	3.16	5.95		0.550	0.266	0.227
229	20.9	5.67	3686	2.8	300	64.5	19.35	3.16	5.77		0.545	0.191	0.164

Aerospace Corporation
P. O. Box 95085
Los Angeles, California   90045
Attn: Library/Technical Documents Group   1

Jet Propulsion Laboratory
4800 Oak Grove Drive
Pasadena, California 91103
Attn: G. Russel   1

General Dynamics/Convair
P. O. Box 1128
San Diego, California 92112
Attn: A. V. Larson   1

National Aeronautics and Space Administration
Ames Research Center
Moffett Field, California   94035
Attn: H. Stine   1

Princeton University
Forrestal Research Center
Princeton, New Jersey   08540
Attn: Professor R. G. Jahn   1

National Aeronautics and Space Administration
Langley Field Station
Hampton, Virginia   23365
Attn: M. Ellis   1
        R. Hess   1

Avco-Everett Research Laboratory
A Division of Avco Corporation
2385 Revere Beach Parkway
Everett, Massachusetts   02149
Attn: R. M. Patrick   1

United States Air Force
Office of Scientific Research
Washington, D. C.   20025
Attn: Mr. Slawsky   1

Case Institute of Technology
10900 Euclid Avenue
Cleveland, Ohio 44106
Attn: Professor O. K. Mawardi   1
        Dr. Eli Reshotko   1

Space Science, Inc.
301 Bear Hill Road
Waltham, Massachusetts   02154
Attn: J. M. Proud   1

Ford Motor Company
Aeronutronics
Newport Beach, California   92660
Attn: R. M. Spongberg   1

Avco Corporation
Research and Advanced Development Division
201 Lowell Street
Wilmington, Massachusetts   01887
Attn: R. R. John   1
       S. Bennett   1

Magnetohydrodynamics, Inc.
P. O. Box 1815
Newport Beach, California   92660
Attn: V. Blackman   1

General Electric Company
Missile and Space Division
Space Sciences Laboratory
P. O. Box 8555
Philadelphia, Pennsylvania   19101
Attn: P. Gloersen   1

Thermal Mechanical Research Laboratory
OAR USAF
Wright-Patterson Air Force Base, Ohio   45433
Attn: Eric Soehngen   1

Giannini Scientific Corporation
3839 South Main Street
Santa Ana, California 92702
Attn: Adriano Ducati   1

Los Alamos Scientific Laboratory
P. O. Box 1663
Los Alamos, New Mexico   87544
Attn: Dr. Stratton   1

Catholic University of America
Department of Space Sciences and Applied Physics
Washington, D. C.   20017
Attn: Professor C. C. Chang   1

University of Minnesota
Department of Mechanical Eng. - Heat Transfer Lab
Minneapolis, Minnesota 55435
Attn: Dr. E. Pfender   1

McDonnell Aircraft Corporation
P. O. Box 516
St. Louis, Missouri 63166
Attn: Dr. W. van Camp   1

Westinghouse Astronuclear Laboratories
Electric Propulsion Laboratories
Pittsburgh, Pennsylvania 15234
Attn: H. W. Szymanowski, Manager   1

Space Dynamics Corporation
Plasmajet Systems Division
2215 Florence Avenue
Cincinnati, Ohio 45206
Attn: Dr. M. Chai   1

National Aeronautics and Space Administration
Scientific and Technical Information Facility
P. O. Box 33
College Park, Maryland 20740
Attn: NASA Representative RQT-2448   6